

Analytical and Computational Studies of Quasi-1D Spin Models

by

Yushao Chen

A thesis
presented to the University of Waterloo
in fulfillment of the
thesis requirement for the degree of
Doctor of Philosophy
in
Physics

Waterloo, Ontario, Canada, 2024

© Yushao Chen 2024

Examining Committee Membership

The following served on the Examining Committee for this thesis. The decision of the Examining Committee is by majority vote.

External Examiner: Hae-Young Kee
Professor
Dept. of Philosophy of Physics, University of Toronto

Supervisor(s): Yin-Chen He
Adjunct Faculty
Dept. of Physics and Astronomy, University of Waterloo
Roger Melko
Professor
Dept. of Physics and Astronomy, University of Waterloo

Internal Member: Anton Burkov
Professor
Dept. of Physics and Astronomy, University of Waterloo
Timothy Hsieh
Adjunct Faculty
Dept. of Physics and Astronomy, University of Waterloo

Internal-External Member: Marcel Nooijen
Professor, Dept. of Chemistry, University of Waterloo

Author's Declaration

This thesis consists of material all of which I authored or co-authored: see Statement of Contributions included in the thesis. This is a true copy of the thesis, including any required final revisions, as accepted by my examiners.

I understand that my thesis may be made electronically available to the public.

Statement of Contributions

This thesis is based on three research manuscripts. Yushao Chen is the first author of [16].

Chapter 4 draws primarily from the material published in Ref. [16]. This research was conducted under the guidance of Yin-Chen He.

Chapter 5 features work that is yet to be published, conducted in collaboration with Xuzhe Ying and supervised by Liujun Zou.

Chapter 6 includes findings from another unpublished study, undertaken in partnership with Jinmin Yi and under the supervision of Ziwen Liu.

Each chapter reflects a significant collaborative effort and mentorship that greatly enhanced the depth and scope of the research presented.

Abstract

This thesis explores quasi one-dimensional (quasi-1D) quantum spin systems, specifically focusing on Kitaev ladders, Heisenberg ladders, and Motzkin chains. The research employs a combination of analytical and numerical tools to systematically study the phase diagrams of these low-dimensional spin lattices, developing a standardized pipeline for analyzing future models of interest within the field of quantum physics.

At the core of this investigation is the deep interconnection between low-dimensional quantum systems and their corresponding tensor network structures. Utilizing Matrix Product States (MPS) and the Density Matrix Renormalization Group (DMRG) methodologies, the thesis provides detailed insights into the phase behaviors of these quasi-1D systems. This includes examining novel phenomena such as quantum spin liquids, various magnetic orderings, and symmetry-protected topological orders. These findings not only enhance our understanding of quantum physics but also highlight the effectiveness and adaptability of tensor network approaches in tackling complex theoretical problems.

Acknowledgements

I am deeply grateful to my supervisor, Yin-Chen He, for his invaluable guidance, patience, and support throughout my studies and research. His mentorship was crucial in helping me navigate the challenges and meet the timelines of my academic journey.

I extend my thanks to Aaron Szasz for the collaboration during the challenging years of the pandemic. Our teamwork was both smooth and productive, and I look forward to potentially collaborating on future projects.

I owe immense gratitude to Aida Ahmadzadegan-Shapiro and Roger G. Melko for the opportunities you have provided me. Your support has allowed me to venture beyond the realm of pure theoretical physics and into broader scientific explorations!

To all my friends, both within and outside the Perimeter Institute, thank you for sharing these five transformative years with me. While it is impractical to name everyone individually here, since that will easily go longer than my actual work in this thesis, each of you has had a significant impact on my journey. A special acknowledgment goes to the Bistro staff—your efforts have played a pivotal role in fostering our community’s spirit and excellence.

Lastly, to my parents, thank you for understanding and waiting for so long. I sincerely hope we can see each other as soon as possible.

Dedication

To Life. To Joy. To Love.

Table of Contents

Examining Committee	ii
Author's Declaration	iii
Statement of Contributions	iv
Abstract	v
Acknowledgements	vi
Dedication	vii
List of Figures	xii
List of Tables	xvii
1 Introduction	1
1.1 Background	1
1.2 Research Problem and Objectives	2
1.3 Thesis Structure Overview	3
2 Preliminary	5
2.1 Theoretical Physics Background	5

2.1.1	Foundational Hilbert Space for Spin Systems	5
2.1.2	The Role of the Hamiltonian	6
2.1.3	Key Quantities in Quantum Many-Body Systems	7
2.1.4	Phases and Phase Transitions	10
2.1.5	The Thermodynamic Limit and Finite Temperature	11
2.2	Tensor Networks: A Practical Introduction	12
2.2.1	Basic Definition	12
2.2.2	Natural Representation of Low-Dimensional Many-Body Ground/Low-lying States	16
2.2.3	Compression Essence of Tensor Networks	16
2.2.4	Numerical Foundations of Tensor Networks	18
2.2.5	Selective Focus on Tensor Network Techniques	19
2.2.6	Summary	22
3	Methodology	25
3.1	Research Pipeline	25
3.2	Research Resources	27
3.2.1	Software Ecosystem	27
3.2.2	High-Performance Computing Infrastructure	28
4	Spin-S Kitaev Ladders	29
4.1	Definitions and Framework	30
4.2	Higher Spin- S Kitaev Ladders	31
4.2.1	Symmetries of Spin- S Kitaev Ladders	31
4.2.2	Spin-1/2 Ladder and Jordan-Wigner Transformation	34
4.2.3	Spin- S Ladders and Perturbation Theory	38
4.2.4	Spin- S Phase Diagrams	43
4.3	Summary	53

5	Heisenberg Ladder	55
5.1	Definitions and Framework	57
5.2	Phase Diagram	57
5.2.1	Ground State Configuration and Magnetic Properties	58
5.2.2	Gapless Phases and Central Charge Analysis	59
5.3	Dynamics and Luttinger Liquid	61
5.3.1	Correlation Functions and Luttinger Parameter	61
5.3.2	From Static Correlations to Dynamic Responses	62
5.4	Summary	65
6	Motzkin Chains	67
6.1	Definitions and Framework	70
6.1.1	Local Interaction Terms	70
6.1.2	Boundary Conditions	71
6.1.3	Symmetry	71
6.1.4	Physical Meaning	71
6.1.5	Ground State	73
6.2	Combinatorics, Exact MPS, and Orthogonal DMRG	75
6.2.1	Calculating Motzkin Numbers	75
6.3	Motzkin and Quantum Error Correction	82
6.3.1	Calculating Subsystem Variance for the Motzkin Chain	82
6.4	Summary	85
7	Conclusion and Future Work	86
7.1	Key Findings and Comparisons	87
7.1.1	Spin-S Kitaev Ladders	87
7.1.2	Heisenberg Mixed Ladders	87
7.1.3	Motzkin Chains	87

7.2	Extending Tensor Networks: Prospects in Quantum Mechanics and Machine Learning	88
7.2.1	Data Driven Standard Automatic Library	88
	References	89
	APPENDICES	98
A	PDF Plots From Matlab	99
B	SOPs and SPT distinction	105

List of Figures

2.1	Formation of the foundational Hilbert space \mathcal{H} for spin systems through the tensor product of N local spaces \mathcal{H}_d , where each \mathcal{H}_d is spanned by the basis $\{0, 1, \dots, d - 1\}$	6
2.2	Tensor Networks and Matrix Product States (MPS): (a) Generic Tensor Network illustrates a network of five tensors connected by edges that represent tensor contractions, critical for encoding complex quantum states and operations compactly. (b) Mapping to MPS via singular value decomposition (SVD) transforms a high-dimensional quantum state into a one-dimensional chain of tensors (T0 to T5), simplifying the state representation while maintaining essential quantum correlations. This MPS framework is particularly useful for efficient simulations of one-dimensional quantum systems, overcoming challenges posed by the exponential growth of the state space.	13
2.3	Reshaping a tensor \mathbf{T} from a vector (1-leg tensor) to a matrix (2-leg tensor) and further to a 3-leg tensor	14
2.4	Demonstration of Singular Value Decomposition (SVD) as a tunable method for data compression. This example uses a photograph of the author, progressively compressed at bond dimensions of 64, 32, and 16. The images illustrate the varying degrees of compression and their impact on image quality, providing a clear visualization of the trade-off between data reduction and fidelity.	17
2.5	The singular values on a central bond of an MPS from the excited, highly-entangled states of an exotic quantum spin model. The values after the 16th largest are already much close to zero.	18
2.6	Overview of the fDMRG Process	20
2.7	Schematic representation of the TEBD procedure, where time evolution operators are applied to pairs of sites (even and odd) in alternating steps.	23

3.1	Quantum Many-Body Systems Research Pipeline	26
4.1	(a) Definition of Kitaev model on a honeycomb lattice and a two-leg ladder: solid, double, and dashed lines indicate spin interactions as shown in the key, with respective strengths K_z , K_x , and K_y . There is a local symmetry for each plaquette given by a product of local operators $X = e^{i\pi S^x}$, etc. along the interior of each plaquette. (b) Phase diagram of half-integer spin Kitaev ladders; red lines indicate the critical points. (c) Phase diagram of integer spin Kitaev ladders. Dashed lines indicate the first-order phase transition lines of spin-1 ladders. For higher spins, the unnecessary phase transition locations may change.	32
4.2	Jordan-Wigner transformation for spin-1/2 Kitaev Ladder. The upper panel represents the original spin model with the definition of the JWT, and the lower panel shows the Hamiltonian in the Majorana representation. Note that in this representation, the specific transformation we chose makes the local symmetries D_n live only on the bonds between K_y pairs.	35
4.3	Dimer illustration in both anisotropic limits. Here we define $ \uparrow\rangle$ and $ \downarrow\rangle$ to be the eigenstates of S^z s.t. $S^z \uparrow\rangle = S \uparrow\rangle$, $S^z \downarrow\rangle = -S \downarrow\rangle$, and $ \pm\rangle$ the corresponding eigenstates of S^x	39
4.4	Results for spin-1/2 Kitaev ladder. The phase diagrams are found using a 4-site iMPS with $\chi = 64$. (a) Order parameter $\langle e^{i\pi S^x} e^{i\pi S^y} \rangle$ measured on the sites of a Z -bond as shown in the inset, indicating SSB order. The axes show the parameter $K = (K_x, K_y, K_z)$ in spherical coordinates, i.e. $K_z = \sin \theta$, $K_x = \cos \theta \cos \phi$, $K_y = \cos \theta \sin \phi$. (b) Pollmann-Turner order parameter of SPT order [64]. (c) Correlation length on the line $K_x + K_y = 2$, $K_z = 1$ to locate the critical point (d) Ground state energies and the 1st and 2nd derivatives, indicating second-order phase transitions.	44
4.5	(a) Distinction between two SPT orders along the line $K_x + K_y = 2$, $K_z = 1$. The x -axis labels the value of K^x and $K^y = 2 - K^x$. In the inset we depict the distinction between the two SOPs for the two SPT phases. (b) Using finite-entanglement scaling to estimate the central charge $c = 0.5$ of the transition point at $K = (1.5, 0.5, 1.0)$. (c) Using finite-entanglement scaling to estimate the central charge $c = 1.0$ of the transition point at $K = (1.0, 1.0, 0)$	46

4.6	Phase Diagram of Spin-1 Kitaev Ladder. The phase diagrams are found using a 4-site iMPS with $\chi = 64$. (a) SSB phase indicated by the order parameter $\langle S^x S^y \rangle$. (b) The value of $\langle e^{i\pi S^x} e^{i\pi S^y} \rangle$ in the phase diagram. (c) Using finite-entanglement scaling to estimate the central charge of the phase transition point near $K = (1.4, 1.4, 1.0)$ between the SSB and trivial phases. (d) Overlaps between GS and two different dimer product states change suddenly at the first order phase transition around $\phi = 0.6$ with $\tan \phi = 0.69$ as predicted while the value of θ is close to $\pi/2$	49
4.7	Phase diagram of spin-3/2 ladders. The phase diagrams are given by a 4-site iMPS with $\chi = 128$. (a) Order parameter $\langle e^{i\pi S^x} e^{i\pi S^y} \rangle$. (b) Pollmann-Turner order parameter for SPT order [64]. (c) Central charge estimation at a critical point $\theta = \frac{2}{9}\pi, \phi = 0.55$, giving $c \approx 0.5$. (d) Correlation length ξ and second derivative of energy $d^2 E/d^2 \phi$ along $\theta = \frac{2}{9}\pi$	50
4.8	Phase Diagram of Spin-2 Kitaev Ladder. The phase diagrams are given by a 4-site iMPS with $\chi = 128$. (a) The phase diagram given by the order parameter $\langle S^x S^y \rangle$. (b) The value of $\langle e^{i\pi S^x} e^{i\pi S^y} \rangle$ in the phase diagram. (c) Central charge estimation at a transition point. (d) Overlaps between GS and two different dimer product states change suddenly at the first order phase transition points around $\phi = 0.53$ and $\phi = 0.70$ while the value of θ is close to $\pi/2$	51
5.1	Phase Diagram of Heisenberg Ladders	58
5.2	Entanglement entropy scaling for various J_{inter} values at $J_{\text{AFM}} = 1$. The slopes of these lines are used to extract the central charge c . For $J = 0.1$, we find $c \approx 1.18$, while for $J \geq 0.5$, the central charge much closer to $c \approx 1.0$	60
5.3	Correlation functions for a Heisenberg ladder. Blue dots are the sampled data points measured over the simulated MPS via DMRG; orange curves are fitted functions. Left: $\langle S^z(x, 0) S^z(0, 0) \rangle$. Right: $\langle S^+(x, 0) S^-(0, 0) \rangle$. The fitting results indicate a Luttinger parameter $K \approx 0.46$	62
5.4	Dynamical structure factor $S_{\text{FM}}^{\pm}(k, \omega)$. The right panel is a zoomed-in version of the left panel, enhancing details. The left panel is presented on a log10 scale, while the right panel uses a linear scale.	63
5.5	Dynamical structure factor $S_{\text{AFM}}^{\pm}(k, \omega)$ displayed on a log10 scale, highlighting the complex high-energy excitations distinct to the AFM leg.	64
5.6	Dynamical structure factor $S_{\text{FM}}^{zz}(k, \omega)$ in log10 scale, emphasizing the low-energy excitations and their dispersion characteristics.	65

5.7	Dynamical structure factor $S_{\text{AFM}}^{zz}(k, \omega)$, presented in log10 scale. The zoomed-in view reveals detailed features of the excitation spectrum.	66
6.1	A Motzkin path in a Motzkin chain of length $2n = 4$	72
6.2	Increase of the entanglement entropy along a Motzkin chain, along with the increase of system size. Meanwhile, though not able to describe with conformal theory, Motzkin groundstate possess similar finite-size scaling behavior with a 'central charge' being 3.	74
6.3	Schmidt values (logarithmic plot) on each bond of a Motzkin ground state MPS of length $2n = 60$. The plot demonstrates the characteristic entanglement structure of the Motzkin state, with higher Schmidt values near the center of the chain and lower values towards the ends.	78
6.4	Power Law of the Subsystem Variance of Motzkin Chain with Scaling System Sizes	83
A.1	Brief illustration of the detection of SPT order. (a) iMPS and its transfer matrix T . The corresponding leading eigenvector is the identity matrix, denoted by "1.". (b) iMPS transformed by a symmetry Σ^a and the corresponding generalized transfer matrix T^a , which is given in terms of the original transfer matrix by a unitary transformation U^a as shown. (c) The leading eigenvector of T^a is U^a . For two different elements a and b in the symmetry group $G = \mathbb{Z}_2 \times \mathbb{Z}_2$, we can calculate $U^a U^b U^{a\dagger} U^{b\dagger}$ to determine whether the iMPS belongs to an SPT phase.	100
A.2	Modification of symmetry action on iMPS for model with two-site symmetries. (a) A usual translation-invariant iMPS under the transformation of its on-site group $G = \{\Sigma\}$. (b) Action of symmetries on the ground state of the cluster model $H = \sum \sigma^x \sigma^z \sigma^x$, invariant under the translation by 2 sites.	101
A.3	(a)(b)An intuitive choice of unit cell inspired by perturbation theory. (c)(d) With this choice of unit cell, Σ_l^Z and Σ_u^Z act, respectively, on the first two sites and the last two sites.	103
A.4	(a) An improperly selected translationally invariant block for the same iMPS and (b) the corresponding local operators for the symmetry Σ_l^Z	104

B.1 Illustration of the string order parameters and their equivalent definition after multiplication with the local symmetries. Two SOPs in different limits map to effective SOPs of cluster model in different ways, which highlights the phase distinction. Note that the capitalized X and Z in the lower part indicate the operators in the effective models. 107

List of Tables

B.1	Pre-images in the original model of the X_{even} and X_{odd} symmetries of the effective cluster model from perturbation theory in the X - and Y -limits for half-integer spin. “rep1” and “rep2” columns give two different elements of the original $\mathbb{Z}_2 \times \mathbb{Z}_2 \times \mathbb{Z}_2$ symmetry group, each of which map to X_{even} or X_{odd} in the specified anisotropic limit.	106
-----	---	-----

Chapter 1

Introduction

1.1 Background

Quantum spin systems have played a pivotal role in advancing condensed matter physics. The study of these systems involves various Hamiltonians, such as the Ising model, where spins interact in a way that confines them to two possible states (up or down) and the Heisenberg model, which respects $\mathbf{SU}(2)$ symmetry, allowing the same spins as in Ising model to rotate freely in any direction in spin space. These models, with their distinct interaction rules, are fundamental in understanding the complex behavior of magnetic systems and have been crucial in the theory of phase transitions [5, 93, 102].

In strongly correlated systems, given the lack of single-particle pictures, one of the significant challenges is the exponential increase in computational complexity with the system size, often referred to as the 'curse of dimensionality.' This has necessitated the development of various numerical and theoretical tools. The Density Matrix Renormalization Group (DMRG), introduced by S.R. White [89, 90, 72], was a groundbreaking algorithm for studying one-dimensional and quasi-one-dimensional systems. DMRG works by optimizing the density matrices instead of directly truncating the wavefunction, which naturally captures the entanglement structure of 1D systems.

In the 21st century, the formalism of Matrix Product State (MPS) has been recognized as a powerful state representation not just within DMRG, but also as a framework for other tensor network methods [72, 85, 60]. MPS is a way to represent quantum states in a one-dimensional lattice with high efficiency, particularly in systems with limited entanglement, and it provides a more intuitive and compact representation of wavefunctions. The

evolution of tensor network methods, of which MPS is a cornerstone, has expanded the toolbox for tackling strongly correlated systems, leading to enhanced precision, reduced computational resources, and deeper insights into quantum many-body systems [85, 18, 86].

Moreover, advances in tensor networks have fostered significant cross-disciplinary applications, particularly in fields closely allied with physics. In quantum computing, tensor networks have been instrumental in efficiently simulating quantum circuits, crucial for developing quantum algorithms [66, 59, 67]. This has profound implications for understanding quantum entanglement and complexity. In the realm of scientific computing, tensor networks are pivotal for computational physics applications in other fields beyond quantum physics, facilitating complex calculations involving multi-particle interaction potentials [60, 33, 59], essential in studying phenomena like electronic structures and quantum phase transitions. Additionally, in high-performance computing, tensor networks have contributed to optimizing tensor operations, particularly for deep learning and artificial intelligence algorithms, which are increasingly relevant in computational physics and data analysis [61, 17, 3]. This wide range of applications highlights the versatility of tensor networks for addressing complex problems across various physics-related domains.

In my capacity as a researcher in the field of quantum matter, I aim to concentrate on uncovering ground states and low-lying excited states of emergent many-body systems. This thesis will highlight some of the most recent and significant systems in this field. I will demonstrate the application of tensor network algorithms to these systems and analyze the intriguing results obtained through these techniques [18, 43, 36]. This approach not only showcases the practical utility of tensor networks in cutting-edge quantum research but also contributes to our understanding of complex quantum phenomena [82, 70, 28]

1.2 Research Problem and Objectives

The core of this thesis is an in-depth exploration of several distinct quantum many-body systems. My approach throughout this work is to present it as an example-driven, theoretical-numerical hybrid guide, designed to serve as a comprehensive reference for myself in the future as well as any other colleagues in the field. The utilization of tensor network algorithms serves as a cornerstone in this investigation, complemented by auxiliary methodologies such as exact diagonalization and perturbation theory, which play significant roles especially in the first example Kitaev ladders. In each case study, these algorithms serve as tools that vividly represent the physical meaning inherent in the corresponding systems, all in the same essential mathematical form but varying according to the physical quantities or phenomena of interests in different cases. This dual focus

ensures that the tensor network algorithms retain their mathematical essence, which is fundamentally rooted in linear algebra, while also providing a tangible link to the physical phenomena they are used to model.

My primary aim is to achieve an organic integration of quantum many-body physics with straightforward numerical methods. This integration is intended to bridge the gap between complex theoretical concepts and their practical numerical applications, thereby enriching the understanding and utility of quantum many-body systems. Through this work, I aspire to contribute to the field by providing a model for effectively combining theoretical physics with computational techniques. This would not only advance the study of quantum systems but also offer a valuable framework for future research endeavors in similar domains.

1.3 Thesis Structure Overview

In this section, I outline the structure of this thesis, which is organized as follows:

Chapter 2 provides the theoretical foundation necessary to understand the systems studied in this work. It begins with an introduction to quantum spin systems, phase transitions, and the thermodynamic limit. It then offers a detailed explanation of tensor networks, focusing on their role in efficiently representing low-dimensional quantum many-body systems. The chapter also discusses the compression techniques and numerical foundations that make tensor networks such a powerful tool in this field.

Chapter 3 describes the methodology employed in this thesis. It outlines the research pipeline, from the design of numerical experiments to the analysis of results. The chapter also provides an overview of the software packages used, such as tensor network libraries, as well as the computational resources that were essential for carrying out large-scale simulations. This chapter serves as a practical guide to the technical aspects of the research.

Chapter 4 focuses on the analysis of *Spin-S Kitaev ladders*, detailing both the model definitions and the methods used to explore their phase diagrams. This chapter includes a study of symmetries, perturbation theory, and ground-state configurations for these systems. The phase diagrams for higher-spin systems are presented, along with detailed explanations of the transitions and critical points encountered.

Chapter 5 shifts the attention to *Heisenberg ladders*, covering both the ground-state properties and dynamic behavior. The chapter explores gapless phases using central charge analysis, as well as the correlation functions that reveal the underlying Luttinger Liquid

characteristics. Additionally, this chapter discusses the static and dynamic responses of these systems to various perturbations.

Chapter 6 addresses the study of *Motzkin chains*, a unique class of quantum systems with combinatorial and quantum error correction properties. The chapter covers the definition of the model, its local interaction terms, and the physical meaning of the ground state. Special emphasis is placed on the exact matrix product state (MPS) representations and the connection to quantum error correction codes. The analysis of Motzkin numbers and the relationship between the chains and orthogonal DMRG methods are also explored in detail.

Chapter 7 concludes the thesis by summarizing the key findings across the three different systems: Spin-S Kitaev ladders, Heisenberg ladders, and Motzkin chains. This chapter also explores future research directions, with a special focus on extending tensor network methods to other quantum mechanical problems and potential applications in machine learning. The limitations and challenges faced during this research are discussed, providing insights for future work in this rapidly evolving area of quantum many-body physics.

Chapter 2

Preliminary

2.1 Theoretical Physics Background

The study of low-dimensional quantum systems has been a profound avenue for understanding the intricate behaviors of quantum materials and phenomena. These systems, typically one- or two-dimensional, provide a simplified yet rich context for exploring quantum mechanics, exhibiting a diverse array of physical properties and phases that both challenge and enrich our theoretical comprehension.

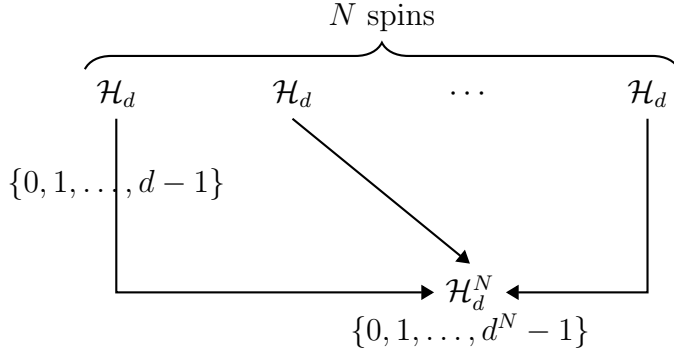
2.1.1 Foundational Hilbert Space for Spin Systems

We initiate our discussion by defining the foundational Hilbert space for spin systems, which are pivotal in the study of quantum many-body systems. For a spin system where each spin has a local dimension d (e.g., $d = 2$ for qubits, $d = 3$ for qutrits and $d = 4$ for ququarts), we can describe the composite space formed by N such spins as follows:

$$\mathcal{H} = \mathcal{H}_d^N \equiv \otimes^N \mathcal{H}_d \quad (2.1)$$

Here, \mathcal{H} represents the combined Hilbert space, with \mathcal{H}_d denoting the Hilbert space of a single spin. The notation \otimes^N signifies the tensor product, which combines the Hilbert spaces of the individual spins N .

The dimension of the resultant space is $D = d^N$, which is the main reason for the notorious dimensional crisis in the numerical studies of any many-body strongly correlated systems. For a single spin, there are only 2 possible states, namely $|0\rangle$ or $|1\rangle$; for two spins, the



Tensor product of N spin Hilbert spaces forming the composite space \mathcal{H} .

Figure 2.1: Formation of the foundational Hilbert space \mathcal{H} for spin systems through the tensor product of N local spaces \mathcal{H}_d , where each \mathcal{H}_d is spanned by the basis $\{0, 1, \dots, d-1\}$.

states are $|00\rangle, |01\rangle, |10\rangle, |11\rangle$; three spins then $|000\rangle, |001\rangle, |010\rangle, |011\rangle, |100\rangle, |101\rangle, |110\rangle$ and $|111\rangle$. This specific illustration clearly shows that the basis set of the Hilbert space consists of all length- N binary numbers, not to mention that a general state should be a linear combination with complex coefficients.

2.1.2 The Role of the Hamiltonian

Recall the foundational equation of quantum mechanics, the Schrödinger equation:

$$i\hbar \frac{\partial}{\partial t} |\psi(t)\rangle = \hat{H} |\psi(t)\rangle, \quad (2.2)$$

where the Hamiltonian \hat{H} , a central element in any quantum theory, defines the interaction rules among different sites and dictates the time evolution of the state $|\psi\rangle$ as $e^{-it\hat{H}}$. At finite temperature, the probability distribution of the eigenstates is proportional to $e^{-\beta\hat{H}}$, where $\beta = 1/(k_B T)$.

The Hamiltonian \hat{H} is a linear operator that can, in principle, be represented by a matrix of dimension $D \times D$, where $D = d^N$ is the size of the Hilbert space for a system with N sites and local dimension d . Without additional constraints, this matrix would have $D^2 = d^{2N}$ independent parameters. However, various physical constraints, such as locality, symmetry, and the Hermiticity of the Hamiltonian, drastically reduce the effective number of independent parameters, confining the system to a much smaller parameter space that corresponds to realistic physical systems.

The focus of many-body physics has traditionally been on ground states or low-lying states, i.e., the eigenstates of the Hamiltonian with the lowest eigenvalues, and on deriving subsequent physical quantities through the measurement of various operators.

Locality and Geometry

In spin systems, the locality of Hamiltonians is determined by the lattice structure and geometry. By generalizing lattices as graphs, it becomes evident that the defining characteristic is the neighborhood configuration. For instance, a nearest-neighbor 1D chain restricts each site to two neighbors, whereas a 2D square lattice includes four neighboring sites per site.

Hermiticity

Hermiticity, a property enforced axiomatically, ensures that the energy and the probability distribution of evolving states remain real and conserved. This property is indispensable for maintaining the physical realism and stability of the system dynamics.

2.1.3 Key Quantities in Quantum Many-Body Systems

In the study of quantum many-body systems, understanding the behavior and characteristics hinges not just on the Hamiltonian, but on a series of interconnected key quantities and concepts. These range from fundamental measures like energy to more complex phenomena such as entanglement and symmetry breaking. Below, we present a progression of these key quantities, emphasizing their mathematical definitions and significance in quantum systems. Here we only sketch the overall logics; for further detailed discussions and derivations, please see related textbooks [74, 104, 98, 4, 51, 30, 68].

Energy and Energy Gaps

The most immediate and fundamental quantity derived from the Hamiltonian \hat{H} is the energy, which is obtained from the eigenvalue equation:

$$\hat{H}|\psi_n\rangle = E_n|\psi_n\rangle,$$

where $|\psi_n\rangle$ are the eigenstates and E_n are the corresponding eigenvalues (energies) of the system. The differences between these energy levels, known as the 'energy gaps', are defined as:

$$\Delta E = E_{n+1} - E_n.$$

Note that, in the context of condensed-matter physics, if no extra explanation, typically energy gaps are specifically for the gaps between ground state(s) and the first excited state(s). Energy gaps play a critical role in determining the system's stability and its phase transitions. For instance, in systems with a non-zero energy gap, the system is typically in a gapped phase, often associated with insulating behavior in condensed matter systems. Conversely, a gapless system, where $\Delta E = 0$, often signals a critical phase, such as in certain quantum phase transitions. Energy gaps also dictate how the system responds to external perturbations, influencing the thermal and dynamic properties of the system.

Density Matrices and Entanglement Entropy

To describe the quantum state of a subsystem within a many-body system, we use the density matrix ρ , which for a pure state is given by:

$$\rho = |\psi\rangle\langle\psi|.$$

For mixed states or subsystems, the density matrix provides a statistical description of the quantum state, $\rho = \sum_i p_i |\psi_i\rangle\langle\psi_i|$ where $\sum_i p_i = 1$. If we partition a system into two subsystems A and B , the reduced density matrix for subsystem A is obtained by tracing out the degrees of freedom of B :

$$\rho_A = \text{Tr}_B(\rho).$$

From this reduced density matrix, we can compute the von Neumann entanglement entropy which measures the degree of quantum entanglement between the two subsystems:

$$S_A = -\text{Tr}(\rho_A \log \rho_A).$$

This quantity is pivotal in understanding quantum correlations, particularly near quantum critical points where entanglement entropy often exhibits scaling behavior. More detailed relationship between entanglement entropy and other quantities e.g. central charges will be revealed afterwards in our concrete research chapters.

Correlation Functions and Mutual Information

Correlation functions quantify how observables, such as spins or charges, are correlated across different parts of the system. For a quantum spin system, the two-point spin-spin correlation function is typically defined as:

$$C(r) = \langle \hat{S}_i^z \hat{S}_{i+r}^z \rangle - \langle \hat{S}_i^z \rangle \langle \hat{S}_{i+r}^z \rangle,$$

where \hat{S}_i^z is the spin operator along the z -axis at site i , and r is the distance between spins. Correlation functions help reveal critical behavior in the system by showing how correlations decay with distance. At a critical point, correlations often decay algebraically:

$$C(r) \sim r^{-\eta},$$

where η is a critical exponent. In non-critical, gapped phases, correlations typically decay exponentially:

$$C(r) \sim e^{-r/\xi},$$

where ξ is the correlation length.

Mutual information extends the concept of correlation by quantifying the total amount of information shared between two subsystems A and B . It is defined as:

$$I(A : B) = S_A + S_B - S_{A \cup B},$$

where S_A , S_B , and $S_{A \cup B}$ are the entanglement entropies of the respective subsystems and their union. Mutual information provides a more global measure of correlations within the system, including both classical and quantum contributions.

Symmetry and Symmetry Breaking

Symmetry considerations play a fundamental role in quantum many-body systems, providing insights into how systems behave under specific transformations. Mathematically, a symmetry of a Hamiltonian \hat{H} is a unitary or anti-unitary operator \hat{U} such that:

$$\hat{U} \hat{H} \hat{U}^\dagger = \hat{H}.$$

This equation means that the Hamiltonian remains invariant under the transformation defined by \hat{U} . Symmetries can be classified into continuous symmetries, such as rotational or gauge symmetries, and discrete symmetries, such as parity or time-reversal symmetry.

In many systems, symmetries may be spontaneously broken in the ground state. Spontaneous symmetry breaking (SSB) occurs when the ground state $|\psi_0\rangle$ of a Hamiltonian does not exhibit the same symmetry as the Hamiltonian itself, i.e.,

$$\hat{U}|\psi_0\rangle \neq |\psi_0\rangle,$$

even though $\hat{U}\hat{H}\hat{U}^\dagger = \hat{H}$ still holds. This broken symmetry leads to the appearance of order parameters which are non-zero in the symmetry-broken phase and can be used to classify different phases of matter. A typical example is the magnetization $M = \langle \hat{S}^z \rangle$ in a ferromagnetic system, which serves as an order parameter and becomes non-zero when rotational symmetry is broken.

In low-dimensional systems, the role of symmetry is particularly profound, influencing stability, determining phase boundaries, and dictating the nature of quantum and thermal fluctuations. For example, in 1D systems, the Mermin-Wagner theorem states that continuous symmetries cannot be spontaneously broken at finite temperature, highlighting the significance of dimensionality in symmetry-breaking phenomena. Symmetry considerations also help in understanding quantum phase transitions where phases are distinguished by different symmetry properties, often characterized by the closing of energy gaps and the emergence of long-range order.

2.1.4 Phases and Phase Transitions

Low-dimensional quantum systems exhibit various phases characterized by their order and symmetries, including gapped and gapless phases, SSB, symmetry-protected topological (SPT) phases, and topologically ordered phases. Gapped phases have a finite energy difference between the ground state and the first excited state, often associated with long-range order and SSB in the thermodynamic limit. In contrast, gapless phases feature a continuous spectrum of low-energy excitations, indicative of critical systems or unconventional ordered states like those in quantum spin liquids.

Phase transitions in these systems, such as quantum phase transitions occurring at zero temperature driven by quantum fluctuations, provide insights into universality and scaling behaviors. The study of SPT phases, which are distinguished by their edge states and protected by global symmetries, and topological order, characterized by non-local entanglement and exotic excitations (e.g., anyons), further enriches our understanding of quantum matter. An important characteristic of phase transitions is whether they are first or second order. First-order phase transitions are typically associated with a discontinuity in the order parameter as a function of tunable parameter in Hamiltonians.

Such discontinuity involves sudden change of orders or a 'cusp' in energy. On the other hand, second-order phase transitions are sometimes called continuous phase transition, implying the fact that those changes in orders or energy happen in a milder way, but in fact bring much more interesting novel phenomena such as universal scaling behaviors along with their critical exponents; this is also one of the main drives for modern condensed-matter research.

2.1.5 The Thermodynamic Limit and Finite Temperature

While the focus of this thesis is primarily on zero-temperature quantum systems, it is essential to acknowledge the importance of the thermodynamic limit and finite temperature effects, as they significantly influence the behavior of many-body quantum systems.

The thermodynamic limit, where the system size approaches infinity ($N \rightarrow \infty$), is fundamental in defining phases and phase transitions in both classical and quantum systems. In finite-size systems, certain phase transitions, such as the spontaneous breaking of symmetry, may not be well-defined, as thermal or quantum fluctuations can overwhelm long-range order. In the thermodynamic limit, however, the system's bulk properties dominate, and phase transitions become sharp, characterized by non-analytic behavior in thermodynamic quantities such as free energy or entropy.

Mathematically, this limit is often expressed as:

$$\lim_{N \rightarrow \infty} -\frac{1}{\beta N} \log Z_N = f,$$

where Z_N is the partition function for a system of size N , f is the free energy per particle, and $\beta = 1/(k_B T)$ is the inverse temperature. As $N \rightarrow \infty$, the bulk thermodynamic properties are captured, and fluctuations around the mean behavior tend to vanish. This limit is crucial for ensuring the extensivity of thermodynamic quantities.

At finite temperature, thermal fluctuations become significant, introducing a competition between thermal and quantum effects. The thermal partition function is given by:

$$Z(\beta) = \text{Tr} \left[e^{-\beta \hat{H}} \right],$$

which weights the system's eigenstates according to the Boltzmann factor $e^{-\beta E_n}$, where E_n are the eigenvalues of the Hamiltonian \hat{H} . As temperature increases, thermal excitations populate higher energy states, which can alter the system's phase and response to external perturbations.

At low temperatures, quantum fluctuations dominate, particularly in low-dimensional systems, where quantum critical behavior is often observed near phase transition points. As temperature increases, these quantum effects are gradually suppressed by thermal fluctuations, leading to a rich interplay between quantum and thermal phenomena. This interplay can be characterized by the thermal de Broglie wavelength, which provides a length scale for comparing quantum and thermal effects.

This competition can give rise to finite-temperature phase transitions, which are driven by thermal fluctuations and are generally described by classical statistical mechanics. However, in systems with strong quantum effects, finite-temperature phase diagrams may exhibit exotic phases such as quantum spin liquids or fractionalized phases, where both thermal and quantum effects play a role.

In summary, while the thermodynamic limit allows for the clear definition of phases and phase transitions, finite-temperature effects introduce thermal fluctuations, which compete with quantum fluctuations to produce complex phase diagrams. These effects are crucial for understanding real-world systems, as actual experiments are often performed at non-zero temperatures, where both quantum and thermal effects must be considered.¹

2.2 Tensor Networks: A Practical Introduction

This section diverges from conventional pedagogical approaches to Tensor Networks (TN), emphasizing the practical numerical implications rather than solely theoretical aspects. Traditional discussions often neglect crucial aspects such as convergence, canonical forms, and error estimation, vital for TN applications in computational physics and quantum information science. Our aim is to demystify these numerical tools, providing an intuitive and practical understanding.

2.2.1 Basic Definition

At its core, a tensor network does not inherently pertain to quantum physics. Conceptually, a tensor network involves a set of tensors, which are multidimensional arrays (similar to the class `ndarray` in `numpy`). These tensors are vertices in a graph, with connections

¹From the perspective of statistical mechanics, these concepts correspond to taking the parameter N for particle number to the limit of infinity for extensive quantities in Hamiltonians, while intensive quantities (like temperature) remain finite. The parameter T for temperature in partition functions is moved away from the limit of zero.

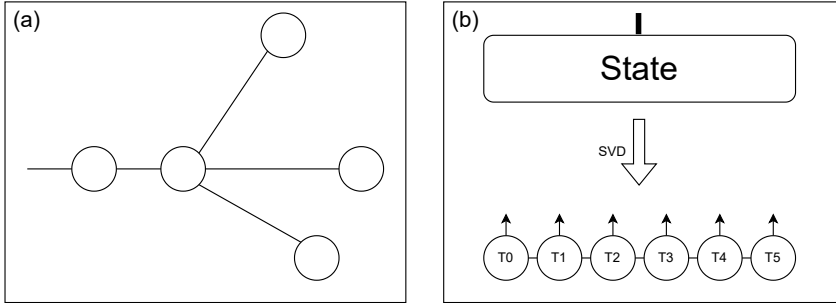


Figure 2.2: Tensor Networks and Matrix Product States (MPS): (a) Generic Tensor Network illustrates a network of five tensors connected by edges that represent tensor contractions, critical for encoding complex quantum states and operations compactly. (b) Mapping to MPS via singular value decomposition (SVD) transforms a high-dimensional quantum state into a one-dimensional chain of tensors (T0 to T5), simplifying the state representation while maintaining essential quantum correlations. This MPS framework is particularly useful for efficient simulations of one-dimensional quantum systems, overcoming challenges posed by the exponential growth of the state space.

between them defined as edges. See Figure 2.2 (a) for an illustration. This setup forms a computational graph that can be contracted as long as each pair of connected tensors has correspondingly compatible dimensions. In cases where a tensor lacks sufficient dimensions for contraction, dummy spaces can be added to facilitate forced contraction. Such a structure, based on fundamental principles of linear algebra, is what defines a tensor network.

Reshaping

A key operation in tensor networks is reshaping, which allows us to view the same data in different dimensional structures without changing the underlying information. Figure 2.3 illustrates this concept:

As shown in Figure 2.3, a tensor \mathbf{T} can be represented in multiple ways:

- As a 1-leg tensor (vector): $\mathbf{T} = [1, 2, 3, 4, 5, 6, 7, 8]$ with a single index i .
- As a 2-leg tensor (matrix): $\mathbf{T} = [[1, 2, 3, 4], [5, 6, 7, 8]]$ with indices j_1 and j_2 .
- As a 3-leg tensor: $\mathbf{T} = [[[1, 2], [3, 4]], [[5, 6], [7, 8]]]$ with indices k_1 , k_2 , and k_3 .

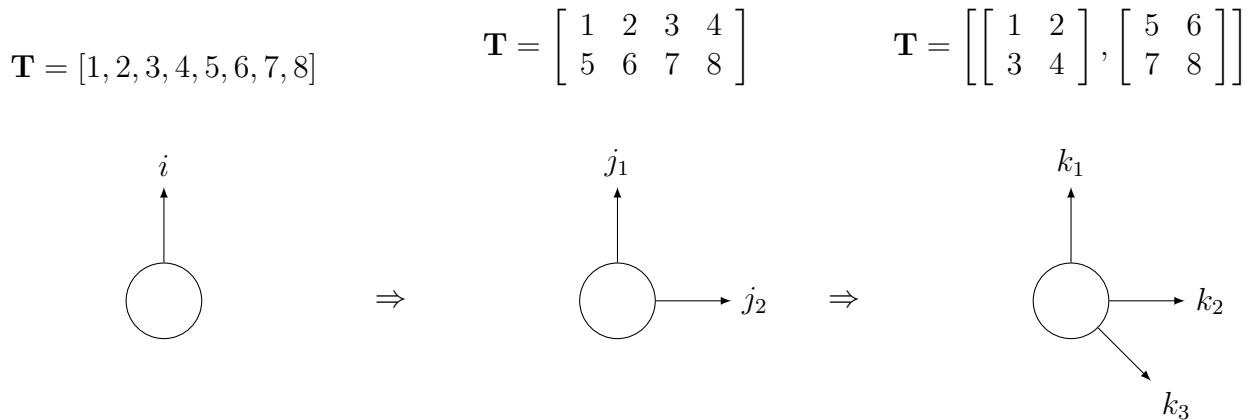


Figure 2.3: Reshaping a tensor \mathbf{T} from a vector (1-leg tensor) to a matrix (2-leg tensor) and further to a 3-leg tensor

In the context of tensor networks, reshaping operations play a crucial role in facilitating the contraction of tensors with compatible dimensions². When tensors lack sufficient dimensions for contraction, we can reshape them or introduce dummy dimensions to make the operation possible. A prime example of this occurs in Matrix Product States (MPS), where tensors associated with individual sites are contracted with neighboring tensors to obtain the full wavefunction.

Consider an MPS where each site is represented by a tensor $T_i^{\sigma_i}$ with three indices: a physical index σ_i and two bond indices. To contract tensors on neighboring sites, say $T_i^{\sigma_i}$ and $T_{i+1}^{\sigma_{i+1}}$, the bond dimensions must be compatible for summation over the shared index. However, before contraction, it is often necessary to reshape the tensors into matrices by combining certain indices. For instance, we can reshape $T_i^{\sigma_i}$ into a matrix by combining the physical index σ_i and one bond index, thus allowing contraction with the adjacent tensor $T_{i+1}^{\sigma_{i+1}}$.

This reshaping process is particularly vital when dealing with tensors that have multiple indices, as it simplifies the tensor structure and enables efficient contraction. In practical terms, we might start with a tensor of shape (d, D, D) , where d is the physical dimension and D is the bond dimension. We can reshape this tensor into a matrix of shape $(d \times D, D)$, facilitating matrix multiplication with neighboring tensors. Once the contraction

²This reshaping process is fundamental in tensor network operations, enabling efficient contractions and manipulations of high-dimensional data. The ability to view and operate on the same data in different dimensional structures is a cornerstone of tensor network computations.

is complete, the result can be reshaped back into a tensor to continue the tensor network algorithm.

These reshaping operations are not merely theoretical constructs but are widely implemented in numerical algorithms such as the Density Matrix Renormalization Group (DMRG) and Tensor Network States (TNS). In these methods, reshaping allows for efficient manipulations of tensors while preserving the necessary structure for contraction and other operations.

The flexible structure afforded by reshaping operations, rooted in the principles of linear algebra and multidimensional array manipulations, forms the foundation of tensor networks. This flexibility makes tensor networks a powerful tool for handling complex data structures and computations across various fields, including but not limited to quantum physics, machine learning, and data compression.

Contraction of Tensors

In tensor algebra, contraction involves summing over the indices of tensor components that appear in multiple tensors, following the rules of Einstein summation convention. For example, contracting a two-leg tensor A with indices i, j and a three-leg tensor B with indices j, k, l involves computing $\sum_j A_{ij} B_{jkl}$. This operation reduces the number of free indices by summing over the repeated indices, leading to a new tensor that combines information from both A and B .

Computational Considerations The true significance of tensor contraction, however, lies beyond the mathematical definition. In practical applications, especially in computational physics and numerical simulations, the order in which tensor contractions are performed can drastically affect the computational complexity of the task. This is because:

- **Efficiency:** Different contraction sequences can lead to varying amounts of intermediate data being generated. Some sequences minimize the size of intermediate tensors, leading to significant reductions in computational time and resource usage.
- **Optimization:** Identifying the optimal order of contraction—often via algorithms like those used in tensor network optimizations—can be crucial for managing the exponential growth of tensor dimensions in many-body physics, quantum computing simulations, and other fields.

Therefore, understanding and optimizing tensor contraction sequences is not just a matter of theoretical interest but a critical factor in the efficiency of algorithms that handle large-scale tensor calculations. This makes the study of tensor contraction essential for advancing computational techniques in various scientific domains. Fortunately in this thesis we do not claim to make any contribution to the current tensor contraction algorithms³.

2.2.2 Natural Representation of Low-Dimensional Many-Body Ground/Low-lying States

The quantum states, especially those in the spin systems, are nothing but complex vector arrays of exponentially high dimensions. However, given the predefined tensor-product structure (the geometry of the physical lattices/graphs of the researchers' interests), it is natural to consider tensor networks as the representations of the corresponding statevectors. Moreover, a class of algorithms from last century [90], density matrix renormalization group (DMRG), was already shown to be able to improve drastically and sometimes optimize the accuracy of such MPS representations of quantum states [72].

This approach is validated by numerous demonstrations in the field. MPS are recognized as the state-of-the-art method for simulating low-lying states in one-dimensional or quasi-one-dimensional quantum many-body systems [17]. This prominence is largely due to the adherence of such states to the so-called "area law" of entanglement. This law posits that the entanglement entropy of a subsystem scales with the boundary (or "area") of the subsystem rather than its volume. According to this law, the bipartite entanglement does not increase exponentially, which typically sustains the feasibility of tensor networks for such applications. Meanwhile, many of the interesting many-body quantum systems have hamiltonians that can be expressed as Matrix Product Operator, MPO, yet another tensor network with very similar structures as MPS.

2.2.3 Compression Essence of Tensor Networks

Tensor Networks (TN) leverage the classical linear algebra technique of Singular Value Decomposition (SVD) for data compression. This methodology, when adapted to quantum physics, facilitates the efficient representation of quantum systems, such as two-qubit systems. By controlling the compression through the manipulation of singular values, TN

³instead, we either already used pre-defined contraction package written by experts or reinvent wheels for those new networks which happen to not yet be included in standard packages.



Figure 2.4: Demonstration of Singular Value Decomposition (SVD) as a tunable method for data compression. This example uses a photograph of the author, progressively compressed at bond dimensions of 64, 32, and 16. The images illustrate the varying degrees of compression and their impact on image quality, providing a clear visualization of the trade-off between data reduction and fidelity.

allows for a precise yet compact expression of bipartite quantum states, exemplifying the trade-off between compression and fidelity in the representation of quantum states.

To revisit the fundamentals of SVD: for any matrix M , say dimension $m \times n$, it decomposes as:

$$M = USV^\dagger \quad (2.3)$$

where U is a unitary matrix in space of dimension m and V is another one but in space of dimension n ; S is a m by n matrix but only nonzero on the diagonal line. This decomposition is guaranteed as MM^\dagger and $M^\dagger M$ are Hermitian, thus allowing for eigen-decomposition. The resultant forms are⁴:

$$MM^\dagger = US^2U^\dagger, \quad M^\dagger M = VS^2V^\dagger. \quad (2.4)$$

A noteworthy point is the preservation of information within M , including the sign or phase of eigenvalues. In quantum applications of particular relevance here, the matrices involved are typically reduced density matrices, which are semi-positive, thereby circumventing potential issues related to eigenvalue sign or phase.

By discarding smaller singular values in the matrix S , significant data compression can be achieved while maintaining essential information. This approach remains a widely utilized technique for efficient data storage and processing. Figure 2.4 provides a practical demonstration of this method, illustrating how SVD can be used to compress an image at various levels of granularity, balancing data reduction with fidelity to the original image.

⁴Simultaneous validation of the two equations can be seen from $MM^\dagger = US^2U^\dagger \implies M^\dagger MM^\dagger = M^\dagger US^2U^\dagger \Leftrightarrow M^\dagger MM^\dagger U = M^\dagger US^2 \Leftrightarrow (M^\dagger M)(M^\dagger U) = (M^\dagger U)S^2$ i.e. the eigendecomposition of $M^\dagger M$.

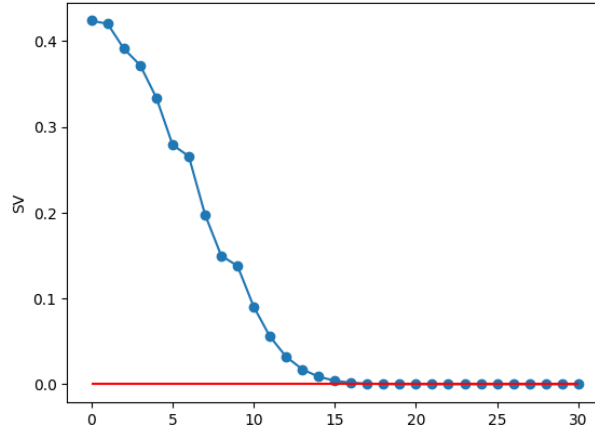


Figure 2.5: The singular values on a central bond of an MPS from the excited, highly-entangled states of an exotic quantum spin model. The values after the 16th largest are already much close to zero.

In quantum physics, state vectors and density matrices are typically more structured and predictable than real-world data, such as images. As such, the data compression requirements in condensed matter physics are usually more modest, leading to manageable dataset sizes. This characteristic aligns with the middle-scale infrastructure generally used for generating and analyzing quantum data. However, the critical challenges often lie not just in managing data sizes but ensuring the data reliably corresponds to the underlying Hamiltonian. Meanwhile, numerous physical measurements over the state data will be involved, and sometimes it is necessary to evolve the data under certain conditions and constraints, preserving physical accuracy and relevance.

2.2.4 Numerical Foundations of Tensor Networks

The effective application of TN is based on a deep understanding of its numerical foundations that are highly related to the tasks of interests in quantum many-body systems:

- **Canonical Forms:** Canonical forms, such as those for Matrix Product States (MPS), streamline computations and enhance algorithmic efficiency by providing a standardized representation.
- **Convergence:** Identifying conditions for algorithmic convergence and understanding factors affecting convergence rates are essential for reliable TN applications.

- **Error Estimation:** Developing techniques to accurately quantify and mitigate errors in TN algorithms ensures the precision of quantum simulations.

These elements are indispensable for bridging theoretical concepts with practical computational strategies.

2.2.5 Selective Focus on Tensor Network Techniques

Among the family of TN techniques, we focus on those with significant practical utility which were also used by our research:

DMRG

Density Matrix Renormalization Group (DMRG) stands out for its effectiveness in solving one-dimensional and quasi-one-dimensional quantum systems.

In Figure 2.6, we outline the core procedural loop of the DMRG algorithm tailored for finite spin chains. The diagram simplifies the process while avoiding overly technical details, focusing on four crucial phases:

- Initialization:** Establishing the initial matrix product state (MPS) configuration for the computation. As a typical optimization problem, the initialization process can not be ignored and in fact a good choice of initial state greatly improve the overall performance both in speed and quality.
- Selection:** Targeting specific tensors within the MPS for optimization, with other segments acting as the environment or effective Hamiltonian. A common strategy in this step is to select two consecutive sites to improve, and after the program revisit, move to the next two consecutive ones.
- Optimization:** Refinement of selected tensors to improve the approximation of the system's ground state. Elegant and efficient contraction algorithms are required here and this step will consume the majority of computing resources; also, well-organized canonicalizations are typically required to optimize the performance of this step.
- Restoration:** Adjusting the MPS back to its canonical form and preparing for the next iteration. This stage also decides whether to continue with additional optimization cycles or to terminate the algorithm.

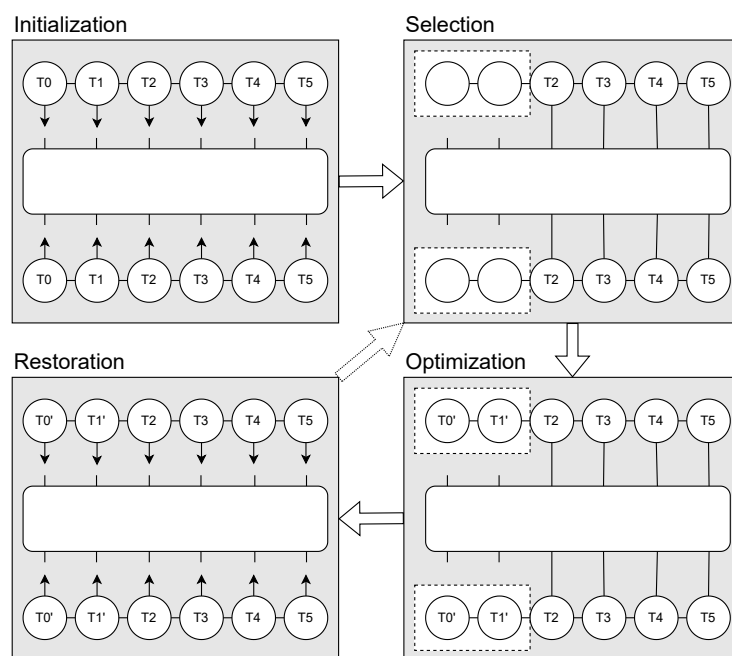


Figure 2.6: Overview of the fDMRG Process

Such algorithms seem quite complicated, but thanks to previous researchers effort currently people do not have to bother reinvent everything all by their own.

TEBD

Time-Evolving Block Decimation (TEBD) is a widely used algorithm for simulating the time evolution of one-dimensional quantum systems represented by tensor networks [80]. It is particularly effective for systems whose Hamiltonians are local, meaning they can be expressed as a sum of terms that each act on only a small number of neighboring sites.

In many quantum systems, the Hamiltonian \hat{H} can be decomposed into two parts, typically referred to as the "even" and "odd" parts, each of which acts on separate neighboring sites:

$$\hat{H} = \hat{H}_{\text{even}} + \hat{H}_{\text{odd}}, \quad (2.5)$$

where \hat{H}_{even} contains terms acting on pairs of sites connected by even bonds, and \hat{H}_{odd} contains terms acting on pairs of sites connected by odd bonds. This structure allows for the use of Trotter-Suzuki decomposition, which approximates the time evolution operator $e^{-it\hat{H}}$ by splitting it into separate exponentials that are easier to compute.

First-Order Trotter Decomposition Using the Baker-Campbell-Hausdorff formula, the time evolution operator can be approximated by the first-order Trotter decomposition:

$$\hat{U}(t) \equiv e^{-it\hat{H}} \approx e^{-it\hat{H}_{\text{even}}} e^{-it\hat{H}_{\text{odd}}} = \hat{U}^{\text{TEBD1}}(t), \quad (2.6)$$

where $\hat{U}^{\text{TEBD1}}(t)$ evolves the system by first applying the time evolution of \hat{H}_{even} , followed by \hat{H}_{odd} . While this approximation is efficient and easy to implement, it introduces an error of order $O(t^2)$, meaning that it becomes less accurate for larger time steps.

Second-Order Trotter Decomposition To reduce this error, the second-order Trotter-Suzuki decomposition is often employed, which introduces a symmetrized form of the time-evolution operator:

$$\hat{U}^{\text{TEBD2}}(t) = e^{-i(t/2)\hat{H}_{\text{even}}} e^{-it\hat{H}_{\text{odd}}} e^{-i(t/2)\hat{H}_{\text{even}}}, \quad (2.7)$$

where the even part is applied for half a time step before and after applying the odd part. This reduces the error to order $O(t^3)$, making the approximation significantly more accurate for small time steps without introducing substantial additional computational cost.

TEBD Procedure and Its Importance The TEBD algorithm works by applying these time-evolution operators to a Matrix Product State (MPS). Since MPS is an efficient representation of low-entanglement states in one-dimensional quantum systems, TEBD is capable of simulating the real-time dynamics of such systems efficiently. After each application of the time-evolution operators, the resulting MPS tensors are updated, and a truncation step is typically employed to ensure that the bond dimension remains manageable, limiting the growth of entanglement.

A typical TEBD algorithm proceeds as follows:

1. **Initial State Preparation:** The initial quantum state is represented as an MPS.
2. **Application of Time Evolution:** For each time step, the time-evolution operator (using either the first- or second-order Trotter decomposition) is applied to the MPS, updating the tensors.
3. **Truncation:** After the application of each operator, the bond dimension of the MPS is truncated using singular value decomposition (SVD), ensuring that the computational cost remains under control.
4. **Iteration:** This process is repeated for each subsequent time step, generating the time-evolved state.

TEBD is particularly important because it allows for the simulation of real-time dynamics in one-dimensional quantum systems, a task that is computationally prohibitive for generic quantum systems due to the exponential growth of the Hilbert space. By leveraging the low entanglement of many quantum systems under local interactions, TEBD efficiently simulates the time evolution of states with only a polynomial increase in computational resources.

Figure 2.7 illustrates the TEBD procedure, where the Hamiltonian is split into even and odd parts, and time evolution is applied to alternating pairs of sites. This methodology highlights the importance of TEBD in advancing the practical applications of tensor networks, particularly in simulating dynamics in quantum systems efficiently and accurately.

2.2.6 Summary

The shift towards a more intuitive and numerically informed discussion of Tensor Networks represents an essential step in demystifying these powerful tools. By emphasizing practical

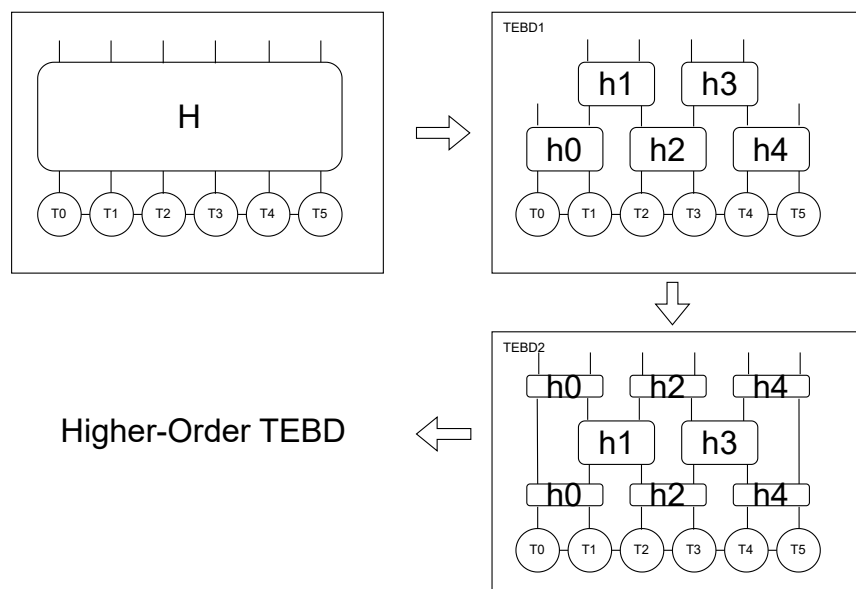


Figure 2.7: Schematic representation of the TEBD procedure, where time evolution operators are applied to pairs of sites (even and odd) in alternating steps.

considerations such as convergence error estimation, and focusing on key TN techniques, we aim to equip readers with the knowledge needed to apply Tensor Networks effectively in their research endeavors.

Chapter 3

Methodology

This chapter outlines the theoretical and practical approaches adopted in this research to redefine the methodology of computational physics. The aim is to establish a more structured, engineering-like framework that transcends the traditional, often chaotic approaches prevalent in the field. This methodology emphasizes reproducibility, systematic investigation, and the application of numerical techniques to address complex physical phenomena.

3.1 Research Pipeline

Our research approach to studying quantum many-body systems is structured and comprehensive, combining fundamental quantum theory aspects with sophisticated computational techniques. The process initiates with three key inputs: the State Space, which delineates the possible configurations of local states; the Graph/Lattice Structure, which describes the spatial arrangement and connectivity of local spins; and the Hamiltonian, which defines the system's energy and interactions, and also serves as the cost function when finding the groundstates.

From these foundational elements, we derive essential information such as local state mappings, spatial relationships within the system, and the dynamics of interactions. This information is subsequently processed using a suite of advanced analytical tools, which include:

- Matrix Product Operators (MPO) for efficient representation of operators,

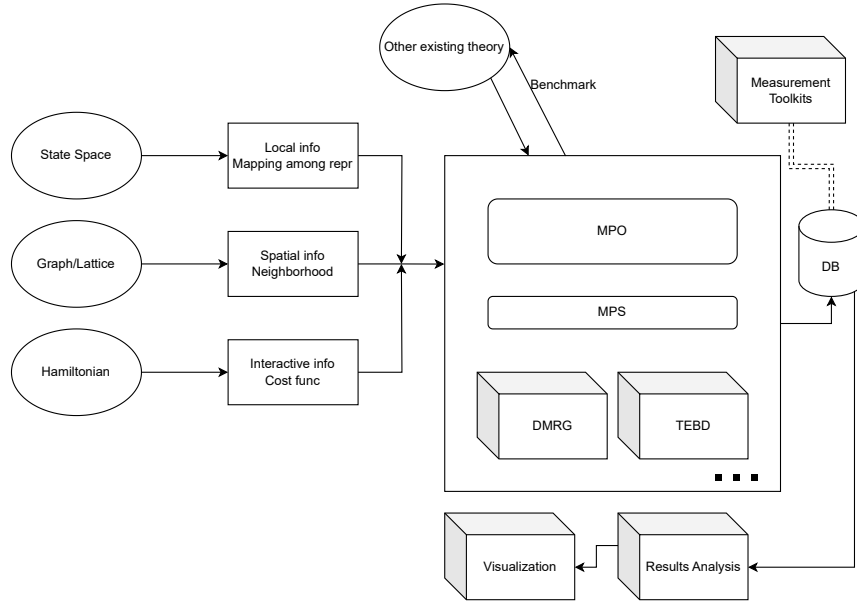


Figure 3.1: Quantum Many-Body Systems Research Pipeline

- Matrix Product States (MPS) for a compact description of states,
- Density Matrix Renormalization Group (DMRG) for precise ground state calculations,
- Time-Evolving Block Decimation (TEBD) for dynamic analysis.

Our methodology emphasizes rigorous validation through benchmarking against established theories to ensure the reliability of our results. All findings are methodically cataloged in a database, which supports ongoing analysis and enriches our cumulative understanding.

This integrated approach equips us to tackle complex quantum systems across various scales and configurations, providing a robust framework for advancing our understanding of quantum many-body phenomena.

3.2 Research Resources

Our research into quantum many-body systems demands a sophisticated array of computational tools and high-performance computing platforms. The complexity of these systems requires not just powerful hardware, but also specialized software capable of handling the intricate calculations involved in quantum simulations.

3.2.1 Software Ecosystem

At the heart of our computational approach lies a carefully curated suite of software packages, each playing a crucial role in our research pipeline:

- **TeNPy**: This Python library is our primary tool for implementing Density Matrix Renormalization Group (DMRG) methods. TeNPy's strength lies in its efficient handling of tensor network algorithms, allowing us to study ground states of complex quantum systems with high precision. We've found it particularly effective for investigating one-dimensional systems with long-range interactions.
- **ITensors.jl**: Written in Julia, this library excels in constructing and manipulating large tensor networks. Its performance in Time-Evolving Block Decimation (TEBD) calculations has been instrumental in our studies of quantum dynamics. The flexibility of ITensors.jl has allowed us to explore novel tensor network structures tailored to specific quantum geometries.
- **NumPy**: While not specific to quantum calculations, NumPy forms the backbone of our data handling and basic numerical operations. Its efficient array operations are crucial for preprocessing our quantum data and post-processing simulation results.
- **Matplotlib**: Visualization is key to understanding the complex results of our simulations. Matplotlib enables us to create both static and interactive representations of quantum state evolution, entanglement growth, and other critical phenomena we observe in our studies.

The synergy between these tools allows us to move seamlessly from raw quantum data to sophisticated simulations and finally to insightful visualizations, forming a comprehensive workflow that enhances our understanding of quantum many-body phenomena.

3.2.2 High-Performance Computing Infrastructure

The computational demands of quantum many-body simulations are substantial, often requiring days or weeks of processing time. To meet these challenges, we leverage several high-performance computing (HPC) resources:

- **ComputeCanada:** This national platform has been invaluable for our long-running simulations. Its vast array of computing nodes allows us to parallelize our calculations, significantly reducing the time required for large-scale quantum simulations. We’ve successfully used ComputeCanada to perform extensive parameter sweeps in our studies of quantum phase transitions.
- **Symmetry (Perimeter Institute):** As a cluster dedicated to theoretical physics, Symmetry offers optimized hardware configurations that align perfectly with our quantum simulation needs. Its high-speed interconnects have proven crucial for our tensor network contractions, enabling us to study systems of unprecedented size and complexity.
- **GitHub:** While not a computational resource per se, GitHub plays a critical role in our research infrastructure. We use it not just for version control, but as a central hub for our entire research workflow. It hosts our simulation scripts, data analysis tools, and even this thesis document, enabling seamless collaboration and ensuring reproducibility of our results.

By strategically distributing our workloads across these platforms, we’re able to optimize our resource usage and tackle a diverse range of quantum many-body problems. The combination of TeNPy and ITensors.jl running on these HPC resources has allowed us to push the boundaries of what’s computationally feasible in quantum many-body simulations.

This integrated approach to our computational resources forms the foundation of our research methodology, enabling us to explore quantum phenomena with unprecedented depth and precision.

Chapter 4

Spin- S Kitaev Ladders

The Kitaev model, a cornerstone in the study of quantum spin liquids, epitomizes the forefront of quantum magnetism and topological physics[40, 82, 28, 81, 5, 102, 70]. Its inception marked a significant leap in understanding entangled spin states, offering a window into the exotic realm of fractionalized excitation and long-range entanglement without the need for symmetry breaking—phenomena central to quantum computing prospects and fault-tolerant quantum information processing [31, 93, 92, 32, 56, 75, 91, 83, 62, 38, 6, 37, 20, 35, 100, 49].

The spin-1/2 Kitaev model, renowned for its exact solvability [53], has illuminated the theoretical landscape with its distinct phase characteristics, demonstrating the potential for realizing a quantum spin liquid state. This state is pivotal for the development of quantum computing technologies due to its robustness against local disturbances, making it an ideal platform for error-resistant quantum computation.

However, the pursuit of extending the Kitaev model to higher spin values ventures into uncharted territory, confronting the loss of exact solvability that underpins the spin-1/2 model's elegance. This expansion is motivated by experimental advancements, revealing a richer landscape of physical phenomena and potential material applications that resonate beyond the confines of the original model [78, 77, 96, 95]. The adaptation of the model to incorporate higher spins promises insights into new quantum states of matter, albeit at the cost of increased computational complexity and the need for innovative numerical methods [36, 42, 21, 34, 103, 19, 50].

Traditional numerical techniques such as exact diagonalization and Monte Carlo simulations, while useful, fall short of capturing the full spectrum of ground state properties in these higher-spin systems [9, 34, 44, 43].

4.1 Definitions and Framework

Kitaev models represent a specific category within the broader class of quantum spin systems known as compass models. These models are distinguished by their incorporation of direction-dependent interactions between spins, with the nature of these interactions being fundamentally tied to the geometric orientations of the bonds connecting them. This directional dependence is a key feature that allows the Kitaev model to capture exotic quantum phenomena, including topological quantum states and phases that are of significant interest in quantum computing and condensed matter physics.

In the context of the Kitaev model, each spin on the lattice has exactly **3** neighbors, and each pair of such neighbors has a unique bond represent the interaction between them. The lattice is composed of bonds that are designated into **3** distinct directions. These directions are not merely spatial orientations but are integral to defining the type of spin-spin interaction along each bond, specified as Ising-like couplings that act with different operators depending on the bond's orientation. This anisotropic interaction scheme is mathematically represented by the Hamiltonian:

$$H = \sum_{\langle ij \rangle} K_{\langle ij \rangle} S_i^{\alpha ij} S_j^{\alpha ij} \quad (4.1)$$

where H denotes the Hamiltonian of the system, the sum runs over nearest-neighbor pairs $\langle ij \rangle$, $K_{\langle ij \rangle}$ represents the coupling strength between spins at sites i and j , and S_i^α and S_j^α are Pauli matrices corresponding to the spins at sites i and j , with α indicating the interaction axis determined by the bond's orientation. This formulation underlines the Kitaev model's foundation on the principle of three-directional-dependent interactions, encapsulating the essence of compass models within a quantum spin lattice framework.

A noteworthy characteristic of Kitaev models is their inherent local symmetries, which are a fundamental aspect across all variants. To better appreciate the complex behavior and universal properties of these models, it is instructive to explore a phenomenon common to all Kitaev models before examining the nuances specific to each variant. Consider a closed loop C within the lattice structure of any Kitaev model. As one proceeds around the loop, visiting each lattice site i , an operator $e^{i\pi S_i^{\beta i}}$ is applied. Here, $S_i^{\beta i}$ denotes the spin component that has not yet been affected by the bonding interactions at site i . Specifically, $S_i^{\beta i}$ is selected from S_i^x , S_i^y , or S_i^z , depending on which spin component remains uninvolved by the bonds meeting at site i . This exercise highlights the local symmetries by demonstrating their preserved nature even as the system configuration varies along the loop.

It is not hard to manually check the commutivity between any such loop operators and the original Hamiltonian (4.1). Noting this feature, it is clear that for the original Kitaev honeycomb lattice, each hexagon plaquette represents a local symmetries.

4.2 Higher Spin- S Kitaev Ladders

Exploring the complex domain of higher-spin Kitaev ladders extends beyond the realm of traditional analytical methods due to the exponential growth in the complexity of their Hamiltonians. Direct diagonalization, while effective for simpler systems, becomes impractical for ladders of arbitrary length and higher spin values. This necessitates a multifaceted analytical and numerical approach to uncover the rich tapestry of quantum states that these systems harbor.

To navigate this complexity, our investigation employs a trio of complementary methods, each tailored to leverage unique insights into the system's behavior:

- Jordan-Wigner transformation offers a window into the fermionic characteristics of spin-1/2 ladders, setting a foundational understanding that aids in contrasting the nuances of higher-spin systems.
- Perturbation Theory becomes indispensable when tackling generic higher spin ladders, especially within anisotropic limits. This method provides a rigorous framework for approximating the system's behavior by systematically breaking down the interaction complexities.
- DMRG simulations stand at the forefront of our numerical arsenal, allowing for the detailed mapping of phase diagrams across a spectrum of higher spin Kitaev ladders. This approach not only validates theoretical predictions but also uncovers new phases and transitions specific to higher spins.

4.2.1 Symmetries of Spin- S Kitaev Ladders

In this section, we explore the symmetries of spin- S Kitaev ladders in detail, facilitating a deeper understanding of their structural and dynamical properties. The symmetries of these systems can be broadly categorized into global and local symmetries. Note that for higher spin, the spin-1/2 anticommutation relations, $\{S^\alpha, S^\beta\} = \delta^{\alpha\beta}$, do not directly generalize. Instead, we have $\{S^\alpha, e^{i\pi S^\beta}\} = 0, \forall \alpha \neq \beta$, and $[S^\alpha, e^{i\pi S^\alpha}] = 0$; in other

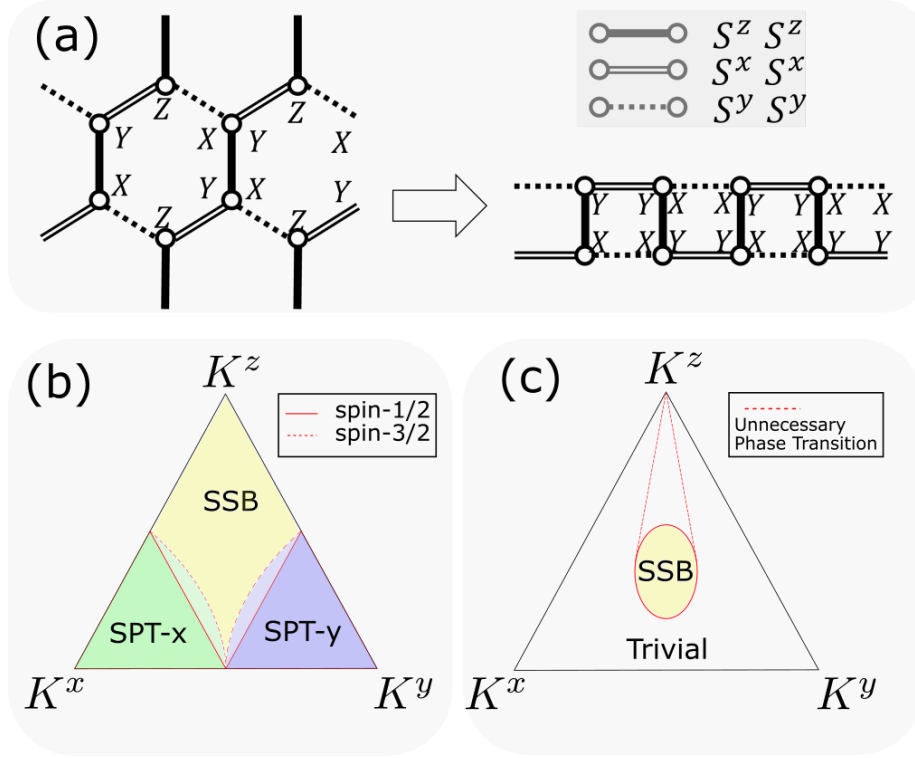


Figure 4.1: (a) Definition of Kitaev model on a honeycomb lattice and a two-leg ladder: solid, double, and dashed lines indicate spin interactions as shown in the key, with respective strengths K_z , K_x , and K_y . There is a local symmetry for each plaquette given by a product of local operators $X = e^{i\pi S^x}$, etc. along the interior of each plaquette. (b) Phase diagram of half-integer spin Kitaev ladders; red lines indicate the critical points. (c) Phase diagram of integer spin Kitaev ladders. Dashed lines indicate the first-order phase transition lines of spin-1 ladders. For higher spins, the unnecessary phase transition locations may change.

words, conjugation by, for example, $e^{i\pi S^x}$ acts as a π rotation around x , thus transforming $S^x \mapsto S^x$, $S^y \mapsto -S^y$ and $S^z \mapsto -S^z$ [7, 73, 8, 16]. It follows immediately that

$$[e^{i\pi S^\alpha} \otimes e^{i\pi S^\alpha}, S^\beta \otimes S^\beta] = 0$$

Global Symmetries

The global symmetry group for Kitaev ladders, particularly those consisting of $4N$ spins, is composed of three fundamental operations: Σ^X , Σ^Y , and Σ^Z , where each operation acts simultaneously on all spins in the system. These operations collectively generate a group described as $Z_2 \times Z_2 \times Z_2$, reflecting the binary nature (two possible states) of each symmetry operation.

The comprehensive global symmetry group, denoted as G , is explicitly given by:

$$G = \{\text{Id}, \Sigma^X, \Sigma^Y, \Sigma^Z, \Sigma_u^Z, \Sigma_l^Z, \Sigma_u^X \Sigma_l^Y, \Sigma_l^X \Sigma_u^Y\} \quad (4.2)$$

where $\Sigma_u^X \Sigma_l^Y$ represents the operation of acting with $e^{i\pi S^x}$ on all sites of the upper leg and $e^{i\pi S^y}$ on the lower leg, and vice versa for $\Sigma_l^X \Sigma_u^Y$. These symmetries highlight the intricate balance and interaction between different spin components across the two legs of the ladder.

Local Symmetries

Local symmetries in Kitaev ladders are characterized by loop operators, denoted as D_n , defined on the smallest square plaquettes within the lattice structure. For a periodic ladder consisting of $4N$ spins, there exist $2N$ independent local symmetries. Each of these symmetries, D_n , can assume eigenvalues of ± 1 .

The presence of these local symmetries plays a crucial role in reducing the complexity of the system's Hilbert space. Specifically, fixing the value of each D_n effectively halves the dimension of the Hilbert space, thereby reducing it by a factor of 2^{2N} . This significant reduction aids in the analytical and computational study of these ladders, providing a clearer understanding of their quantum mechanical behaviors.

Implications of Symmetries

Understanding both the global and local symmetries of Kitaev ladders is essential for investigating their quantum phases and dynamics. These symmetries not only dictate

the possible states and excitations within these systems but also influence their responses to external perturbations and interactions. As such, a thorough comprehension of these symmetries enhances our ability to manipulate and utilize these ladders in various quantum information and computational applications.

4.2.2 Spin-1/2 Ladder and Jordan-Wigner Transformation

Unlike its honeycomb counterpart, which can be exactly solved using the parton solution, the spin-1/2 ladder system allows for a more straightforward and compact method suited to one-dimensional (1D) spin systems: the Jordan-Wigner transformation. This method is also commonly applied across various other systems.

Initially, we map the quasi-one-dimensional ladder into a linear chain, employing what we term "snake ordering":

$$H(K) = \sum_{n=1}^{2N} K_z \sigma_{2n-1}^z \sigma_{2n}^z + K_x \sigma_{2n}^x \sigma_{2n+1}^x + K_y \sigma_{2n-1}^y \sigma_{2n+2}^y \quad (4.3)$$

Here, we denote the operators by σ to emphasize that this method is specifically tailored for spin-1/2 particles and may not be suitable for higher spin systems.

Note that, in the mapped spin chain configuration, each unit cell comprises two spins. Therefore, methods that typically treat each site independently require modifications to accommodate two spins within the same unit cell. This adjustment ensures that the analytical and computational techniques used are correctly aligned with the physical structure of the spin chain.

Jordan-Wigner Transformation

The Jordan-Wigner Transformation (JWT) is a well-established technique for analytically solving certain one-dimensional spin-1/2 chains. It involves nonlocally mapping the Pauli matrices to fermionic operators as detailed below:

$$\begin{aligned} \eta_{2n}^a &= Q_{2n-1} \sigma_{2n}^z \\ \eta_{2n}^b &= Q_{2n-1} \sigma_{2n}^x \\ \eta_{2n+1}^a &= Q_{2n} \sigma_{2n+1}^x \\ \eta_{2n+1}^b &= Q_{2n} \sigma_{2n+1}^z \end{aligned} \quad (4.4)$$

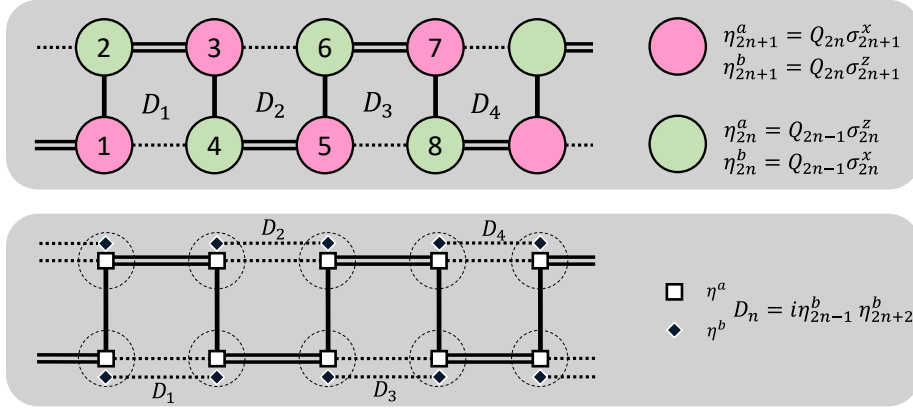


Figure 4.2: Jordan-Wigner transformation for spin-1/2 Kitaev Ladder. The upper panel represents the original spin model with the definition of the JWT, and the lower panel shows the Hamiltonian in the Majorana representation. Note that in this representation, the specific transformation we chose makes the local symmetries D_n live only on the bonds between K_y pairs.

where the string operator $Q_n := \prod_{k=1}^n \sigma_k^y$, with $Q_0 = 1$, ensures proper fermionic anticommutation relations:

$$\{\eta_i^\alpha, \eta_j^\beta\} = 2\delta^{\alpha,\beta} \delta_{i,j} \quad (4.5)$$

The inclusion of these string-operator 'tails' is crucial not only for maintaining Majorana relations but also for facilitating the expression of two-body interactions:

$$\begin{aligned} \sigma_{2n}^x \sigma_{2n+1}^x &= i\eta_{2n}^a \eta_{2n+1}^a \\ \sigma_{2n-1}^z \sigma_{2n}^z &= -i\eta_{2n-1}^a \eta_{2n}^a \\ \sigma_{2n-1}^y \sigma_{2n+2}^y &= (i\eta_{2n-1}^a \eta_{2n+2}^a) (i\eta_{2n-1}^b \eta_{2n+2}^b) \end{aligned} \quad (4.6)$$

Following this transformation, the original bulk Hamiltonian of Kitaev ladders transforms into:

$$H(K) = -K_z \sum_{n=1}^{2N} i\eta_{2n-1}^a \eta_{2n}^a + K_x \sum_{n=1}^{2N-1} i\eta_{2n}^a \eta_{2n+1}^a + K_y \sum_{n=1}^{2N-1} (i\eta_{2n-1}^a \eta_{2n+2}^a) (i\eta_{2n-1}^b \eta_{2n+2}^b) \quad (4.7)$$

This mapping reveals the practical benefits of the initial pairing between (a, b) and (z, x) , where the Y -terms manifest as combinations of a and b terms. These b terms serve as local symmetries within the original Hamiltonian:

$$D_n = (i\eta_{2n-1}^b \eta_{2n+2}^b) = \sigma_{2n-1}^x \sigma_{2n}^y \sigma_{2n+1}^y \sigma_{2n+2}^x \quad (4.8)$$

Each operator D_n consists of two Majorana fermions, indicating a subspace dimension of 2. They may also be interpreted as \mathbb{Z}_2 -fluxes over the fermionic chain.

JWT typically introduces many 'cluster' terms in the Majorana representation for generic spin chains. However, in our case, the two-body interactions within the original model are fortunately still represented as two-body interactions in the transformed Hamiltonian. The only exceptions are the $\sigma^y\sigma^y$ terms, but these also take a convenient form: they are two-body interactions multiplied by local symmetries.

Since these local symmetries commute with the Hamiltonian and with each other, the Hilbert space can be decomposed into a direct sum of subspaces. Each subspace is a simultaneous eigenspace of all the D_n . Within each such subspace, characterized by the set of eigenvalues $(D_1, D_2, \dots, D_{2N})$, where $D_n \in \{\pm 1\}$, each D_n can be treated as a constant. Therefore, the Hamiltonian within each block is effectively quadratic and can be efficiently solved.

Infinite Spin-1/2 Kitaev Ladders, Exact

Assuming that the states of interest are confined within a subspace where the flux configuration is translationally invariant, i.e., $D_n = D = \pm 1$, the fermionic Hamiltonian can be efficiently and analytically solved as a single-body problem through Fourier transformation. The Hamiltonian expressed in momentum space is:

$$H = i \sum_k \alpha_k \beta_k^\dagger (K_z + K_x e^{ik} + (DK_y) e^{-ik}) \quad (4.9)$$

where $\eta_{2n-1}^a = \sum_k e^{ink} \alpha_k$ and $\eta_{2n}^a = \sum_k e^{ink} \beta_k$, with k taking values in

$$k \in \left\{ \frac{\pi(2m+1)}{2N} \mid m = -N, -N+1, \dots, N-1 \right\} \quad (4.10)$$

The resulting spectrum is given by:

$$\epsilon(k; \mathbf{K}, D) = \sqrt{(K_z + P_+ \cos k)^2 + P_-^2 \sin^2 k}$$

where $P_\pm = K_x \pm DK_y$. Integrating over the momentum space yields the energy per site:

$$E(\mathbf{K}, D) = - \int_0^{2\pi} dk \epsilon(k; \mathbf{K}, D)$$

This energy function is utilized in Fig. 3 (d), where critical points are discerned from the singularity in $\frac{d^2 E}{d\lambda^2}$, with λ being the linear parameter that controls the changes along a specific curve in the parameter space for \mathbf{K} .

Finite Spin-1/2 Kitaev Ladders, Open Boundary Condition

For finite-size ladders, the analysis differs depending on whether Open Boundary Conditions (OBC) or Periodic Boundary Conditions (PBC) are applied, though the method of solution remains grounded in efficiently solving a quadratic (single-body) Hamiltonian given a fixed choice of flux configurations $\{D_n\}$.

General Procedure Let $L = 2N$ denote the number of two-site unit cells, and consequently, $2L = 4N$ represents the total number of spins. With the flux configuration set as $D = (D_n)$, for $n = 1, \dots, L$, the Hamiltonian can be reformulated as:

$$H = i\frac{1}{2}\eta^\dagger M \eta \quad (4.11)$$

where $\eta^\dagger := (\eta_1^a, \dots, \eta_{4N}^a)$ and M is a skew-symmetric matrix that depends on K_x, K_y, K_z , and D . The Schur decomposition of M provides $M = O^T N O$, where $N = \bigoplus_{n=1}^L \epsilon_n \begin{bmatrix} 0 & 1 \\ -1 & 0 \end{bmatrix}$, with $\epsilon_n \leq 0$ representing the spectrum, and O being the orthogonal transformation matrix. The Hamiltonian thus simplifies to:

$$H = i\frac{1}{2}\zeta^\dagger N \zeta = \sum_{n=1}^L i\epsilon_n \zeta_{2n-1} \zeta_{2n} \quad (4.12)$$

Open Boundary Conditions (OBC) Under OBC, the ends of the spin chain are not connected, which introduces edge effects that can significantly influence the physical properties of the system. These boundary conditions typically result in a non-cyclic structure of the matrix M , affecting the orthogonality and the eigenvalue spectrum of O . The edge states may manifest zero modes or localized states that decay exponentially from the boundaries inward, affecting the overall spectrum and hence, the ground state energy.

Periodic Boundary Conditions (PBC) In contrast, PBC assume that the chain forms a closed loop, thereby connecting the ends of the chain. This closure enforces a cyclic symmetry in M , which often simplifies the mathematical treatment and leads to a more uniform spectral distribution. The periodicity allows for the application of Fourier transform techniques, enhancing the analytical tractability of the problem. However, it can introduce additional complexities such as the emergence of topological modes depending on the parity of L and the values of D_n .

Transformation to Spin-1/2 System Both boundary conditions leverage the JWT to transform the system into a new spin-1/2 system (denoted by ρ) consisting of only L non-interacting dimers:

$$H = \sum_{n=1}^L \epsilon_n \rho_{2n-1}^z \rho_{2n}^z \quad (4.13)$$

Here, the original number of spins has effectively halved from $2L$ to L due to the fixed D_n . This transformation is beneficial for analyzing the system's dynamics under different boundary conditions, as it reduces the complexity of the Hamiltonian to a more tractable form.

Ground State Energy Calculation Finally, the exact ground state energy of the finite spin chains is calculated by summing over the simplified spectrum:

$$E = - \sum_{n=1}^L \epsilon_n \quad (4.14)$$

Furthermore, examining the appearance of zero modes $\epsilon_n = 0$ as $L \rightarrow \infty$ helps reveal the degeneracy of the original systems in the thermodynamic limit, offering insights into the quantum characteristics dictated by the boundary conditions.

4.2.3 Spin- S Ladders and Perturbation Theory

Brief Review of Perturbation Theory

In perturbation theory, the Hamiltonian is divided into an unperturbed part, H_0 , and a perturbing Hamiltonian, H' :

$$H = H_0 + H'$$

Here, H_0 is typically simple, with well-defined eigen-subspaces that are straightforward to identify. This partitioning simplifies the full Hilbert space, \mathcal{H} , into the ground subspace, \mathcal{H}_{GS} , and the excited subspace, \mathcal{H}_{ES} , with no off-diagonal components of H_0 linking the two.

The ground subspace \mathcal{H}_{GS} is often highly degenerate. In the case of N -spin- $\frac{1}{2}$ Kitaev ladders, for example, it is $2^{N/2}$ -dimensional in the anisotropic limits. The aim is to understand how H' influences the degeneracy within \mathcal{H}_{GS} to derive the effective Hamiltonian projected onto \mathcal{H}_{GS} .

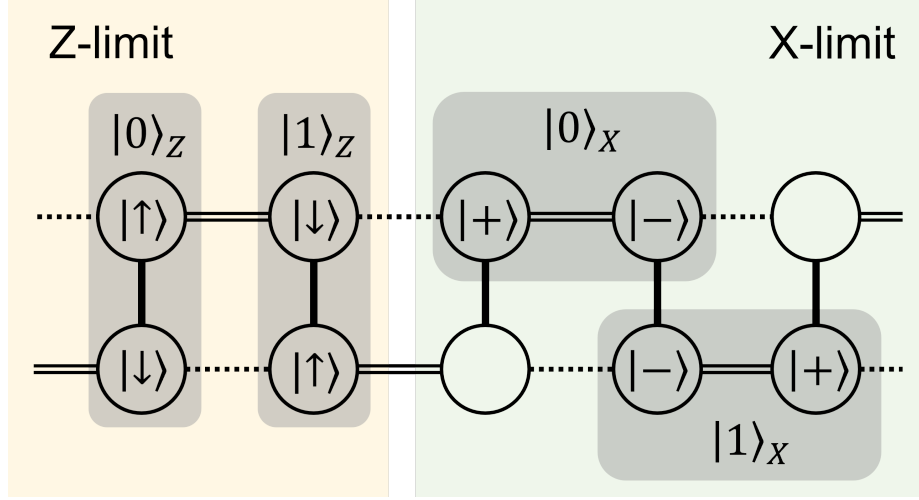


Figure 4.3: Dimer illustration in both anisotropic limits. Here we define $|\uparrow\rangle$ and $|\downarrow\rangle$ to be the eigenstates of S^z s.t. $S^z |\uparrow\rangle = S |\uparrow\rangle, S^z |\downarrow\rangle = -S |\downarrow\rangle$, and $|\pm\rangle$ the corresponding eigenstates of S^x .

Degeneracy is addressed through 'virtual' processes where repeated applications of H' transition states between \mathcal{H}_{GS} and \mathcal{H}_{ES} . These processes enable H' to introduce non-trivial matrix elements within \mathcal{H}_{GS} , effectively lifting the degeneracy. The resulting effective Hamiltonian is given by:

$$H_{\text{eff}} = E_0 + \sum_{n=1}^{\infty} \mathcal{P}_{\text{GS}} (H' \tilde{\mathcal{P}}_{\text{ES}})^{n-1} H' \mathcal{P}_{\text{GS}}$$

where $\mathcal{P}_{\text{GS}} = \sum_{\psi \in \mathcal{H}_{\text{GS}}} |\psi\rangle\langle\psi|$ and $\tilde{\mathcal{P}}_{\text{ES}} = \sum_{\psi \in \mathcal{H}_{\text{ES}}} \frac{1}{E_0 - E_{\psi}} |\psi\rangle\langle\psi|$.

Application to Kitaev Ladders

The spin- $\frac{1}{2}$ Kitaev honeycomb model is renowned for its exact solvability, a trait that extends to spin- $\frac{1}{2}$ ladders as well. However, models with higher spins on both honeycomb and ladder configurations cannot be exactly solved. In these cases, perturbation theory provides a valuable tool for deriving simpler effective models, particularly in anisotropic limits such as $K_x \gg K_y, K_z > 0$ or $K_z \gg K_x, K_y > 0$. The symmetry implies that the case of large K_y is analogous to large K_x .

The Hamiltonian H is divided into $H = H_0 + H'$, where H' is small. In the significant limits of K_z (the Z -limit) or K_x (the X -limit), the dominant interaction term forms H_0 , and the lesser terms contribute to H' :

$$\begin{aligned} H_{0,\mathbf{Z}} &= K_z h^z, & H'_{\mathbf{Z}} &= K_x h^x + K_y h^y, \\ H_{0,\mathbf{X}} &= K_x h^x, & H'_{\mathbf{X}} &= K_z h^z + K_y h^y, \end{aligned}$$

where $h^\gamma = \sum_{\langle i,j \rangle_\gamma} S_i^\gamma S_j^\gamma$.

In these limits, H_0 defines an effective spin- $\frac{1}{2}$ chain with each dimer representing a strong bond. The dimers each have two degenerate local ground states, creating an effective spin- $\frac{1}{2}$ degree of freedom: $|0\rangle_k = |S^k = +S\rangle|S^k = -S\rangle$ and $|1\rangle_k = |S^k = -S\rangle|S^k = +S\rangle$ for $k = x, z$. The effective Hamiltonian is influenced by the powers of H' acting within \mathcal{H}_{GS} .

Effective models in both X - and Z -limits differ between half-integer and integer spins. We define Pauli operators for the effective model as τ , with $\tau^z|0\rangle = |0\rangle, \tau^z|1\rangle = -|1\rangle$. These operators reduce the complexity of the original model from $(2S + 1)^2$ to 2, preserving relationships with the symmetries of the original model. These relationships and global/local symmetries are simplified in the effective model, summarized in Table II.

In the half-integer-spin case under the Z -limit, τ^y anti-commutes with most global symmetries, serving as an order parameter for spontaneous symmetry breaking (SSB). In contrast, in the integer-spin scenario, where $\langle S^x S^y \rangle$ anti-commutes with global symmetries, it is more suitable as an order parameter.

Effective Model for Half-Integer Spins

X -limit: When K_x dominates, the ground subspace comprises dimers on the original X -bonds as indicated in the right part of Fig. 2. The effective Hamiltonian is given by:

$$H_{\text{eff}}(K) = \alpha_{S,x}(K) \sum_{i=1}^{2N} \tau_i^z \tau_{i+1}^x \tau_{i+2}^z,$$

where α is a coefficient dependent on S and K . This Hamiltonian characterizes the cluster model, a typical model of symmetry protected topological (SPT) order, guarded by a $\mathbb{Z}_2 \times \mathbb{Z}_2$ symmetry. The protecting symmetries, $X_{\text{even}} = \prod_i \tau_{2i}^x$ and $X_{\text{odd}} = \prod_i \tau_{2i+1}^x$, mirror the $\mathbb{Z}_2 \times \mathbb{Z}_2$ subgroup symmetries of the original model's $\mathbb{Z}_2 \times \mathbb{Z}_2 \times \mathbb{Z}_2$ symmetry group.

Additional $\mathbb{Z}_2 \times \mathbb{Z}_2$ subgroups that protect the SPT order include $\Sigma_u^Z \times \Sigma_l^Z$, where Σ_u^Z and Σ_l^Z act as X_{even} and X_{odd} , respectively. Σ^Y operates as the global X symmetry, influencing

how symmetries are mapped in the X - and Y -limits. Particularly, $\Sigma_u^X \Sigma_l^Y$ and $\Sigma_l^X \Sigma_u^Y$ also form part of the protecting symmetries, showing the detailed interplay of symmetries in the effective model.

In the Z -limit, when K_z is predominant, the effective Hamiltonian is:

$$H_{\text{eff}}(K) = \alpha_{S,z}(K) \sum_{i=1}^{2N} \tau_i^y \tau_{i+1}^y.$$

This Ising-type Hamiltonian, with τ^y as the order parameter, corresponds to the operator $e^{i\pi S^x} \otimes e^{i\pi S^y}$, breaking the symmetries $\Sigma^X, \Sigma^Y, \Sigma_u^Z$, and Σ_l^Z in the original model. It provides a profound insight into the symmetry transformations and the resultant SPT orders in Kitaev ladders under extreme anisotropic conditions.

Effective Model for Integer Spins

X -limit: The ground subspace configuration remains consistent across different spin magnitudes, consisting of dimers on the original X -bonds. However, the effective Hamiltonian for integer spins differs from the half-integer case:

$$H_{\text{eff}}(K) = \alpha_{S,x}(K) \sum_{i=1}^{2N} \tau_i^x,$$

resulting in a trivial ground state linked to a product state of dimers.

Z -limit: In this scenario, the effective Hamiltonian is more complex:

$$H_{\text{eff}}(K) = \sum_{i=1}^{2N} \alpha_{S,z}(K) \tau_i^x + \beta_{S,z}(K) \tau_i^x \tau_{i+1}^x. \quad (4.15)$$

This model incorporates two distinct terms with separate coefficients, potentially allowing for first-order phase transitions between different product states.

SSB Phase: For integer spins, both limits traditionally do not favor spontaneous symmetry breaking. However, numerical simulations indicate the presence of an SSB phase in integer S away from the extreme anisotropic limits, a finding that will be further discussed in subsequent sections.¹

¹The detailed computation procedure of these coefficients in all the effective models will be published in my GitHub along with another future work that has not yet been involved in this thesis.

Local Symmetries in the Effective Models

The effective models derived for the Kitaev ladders, as seen from the first two rows of Table II, are notably influenced by the summation of local symmetries. This observation is not only theoretically intriguing but also practically beneficial. Specifically, by solving a simple commuting Hamiltonian in the effective model, one can deduce the ground state flux configuration in the original model. This approach is particularly advantageous in higher-spin scenarios where Lieb's theorem may not directly apply.

The uniqueness of the ground state derived through perturbation theory, by selecting a specific flux configuration, implies a corresponding uniqueness in the ground subspace of H_0 , \mathcal{H}_{GS} . For each flux configuration, \mathcal{H}_{GS} intersects with the corresponding subspace of \mathcal{H} as a one-dimensional space, containing a single state. This holds true in the X -limit for both integer and half-integer spins. Conversely, in the Z -limit, only even-numbered $D = +1$ flux configurations are considered, leading to a two-dimensional intersection in the half-integer spin case. This results in two potential ground states, indicative of \mathbb{Z}_2 spontaneous symmetry breaking (SSB). For integer spins, however, the additional τ^x term in the effective model uniquely determines the ground state within this two-dimensional space.

Comparison with Honeycombs

Perturbation theory has been applied extensively to the Kitaev honeycomb model for both spin- $\frac{1}{2}$ and higher spins. This analysis provides a useful benchmark for comparing with the Kitaev ladder models. In the honeycomb model, due to inherent symmetries, the scenarios with large K_x , K_y , and K_z are equivalent, simplifying the analysis.

For half-integer spins on the honeycomb, perturbation theory reduces the model to the toric code. This model is emblematic of topological quantum computing and exhibits non-trivial topological phases. The toric code effectively captures the essence of topological protection similar to what is observed in the cluster model of the ladder, which serves as a one-dimensional analogue to the toric code.

In contrast, for integer spins, the honeycomb model simplifies to disconnected spins in a magnetic field. This configuration leads to a trivial ground state without any interaction between the spins, mirroring the trivial paramagnetic state found in the integer-spin ladder models under the X -limit.

However, the Z -limit of the ladder model does not correspond directly with any of these honeycomb model behaviors. This divergence highlights unique characteristics inherent to

the ladder configuration.

4.2.4 Spin- S Phase Diagrams

Spin-1/2 Kitaev Ladders

For the case of spin- 1/2, we employ both analytical and numerical approaches to conclusively determine the phase diagram. Our results are consistent with previous works[14, 2, 52, 97, 22]. However, we also go beyond them, providing a more detailed classification of phases.

Analytical and Numerical Methods The spin-1/2 Kitaev ladder can be solved analytically via Jordan-Wigner transformation, which takes a 1D spin-1/2 system to a (Majorana) fermionic system by a specific non-local transformation. A further Fourier analysis gives the energy spectrum and predicts the energy gap to close at $||K_x| - |K_y|| = |K_z|$. The gap closing corresponds to a second order phase transition as confirmed by computing derivatives of the energy.

Phase Classification and Transitions Although the analytical solution for spin-1/2 ladders gives efficient access to the ground state energy, numerical simulations with DMRG provide more efficient access to entanglement entropy, expectation values of operators such as the order parameter $\langle e^{i\pi S^x} e^{i\pi S^y} \rangle$ illustrated in Fig. 4.4(a), and the detection of SPT order. Additionally, numerical simulations help us compare the spin-1/2 Kitaev ladder with its higher-spin counterparts.

Phase classification The gap-closings found analytically suggest that there are just three phases for $K_x, K_y, K_z > 0$, each including one of the perturbative limits of large K^z , large K^x , and large K^y . Using DMRG simulations directly in the thermodynamic limit, we confirm the presence of exactly three distinct phases, and we determine the nature of the phases and the transitions between them. In particular, we look for an SSB phase corresponding to the half-integer Z -limit perturbation theory by numerically evaluating the order parameter $\langle \tau^y \rangle = \langle e^{i\pi S^x} e^{i\pi S^y} \rangle$ and for SPT order protected by $\Sigma_l^Z \times \Sigma_u^Z$ using both the method of Pollmann and Turner [64] (see also Appendix A) and string order parameters (SOPs).

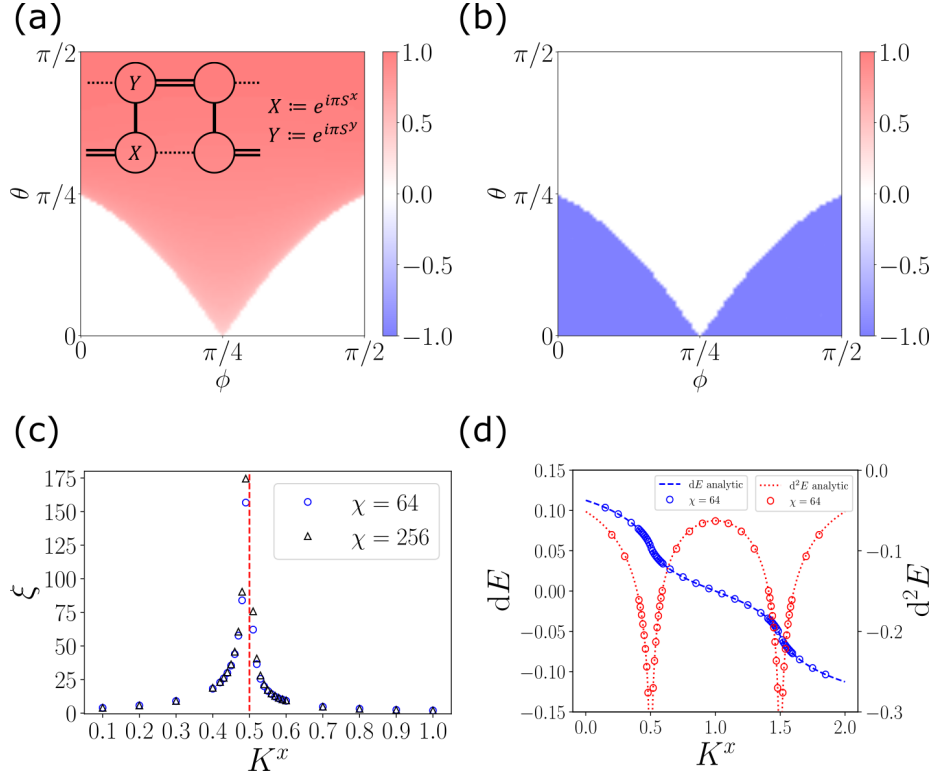


Figure 4.4: Results for spin-1/2 Kitaev ladder. The phase diagrams are found using a 4-site iMPS with $\chi = 64$. (a) Order parameter $\langle e^{i\pi S^x} e^{i\pi S^y} \rangle$ measured on the sites of a Z-bond as shown in the inset, indicating SSB order. The axes show the parameter $K = (K_x, K_y, K_z)$ in spherical coordinates, i.e. $K_z = \sin \theta$, $K_x = \cos \theta \cos \phi$, $K_y = \cos \theta \sin \phi$. (b) Pollmann-Turner order parameter of SPT order [64]. (c) Correlation length on the line $K_x + K_y = 2$, $K_z = 1$ to locate the critical point (d) Ground state energies and the 1st and 2nd derivatives, indicating second-order phase transitions.

Measurements of the order parameter $\langle e^{i\pi S^x} e^{i\pi S^y} \rangle$ show the existence of a large SSB phase. This phase starts from the large- Z limit as we have predicted in the perturbation theory, with the expectation value of the order parameter very close to 1 just like in the Ising model. The computed value of the SSB order parameter throughout parameter space is presented in Fig. 4.4(a).

The two SPT phases are found around the large- K_x and large- K_y limits, confirmed by directly extracting the projective representation of symmetries from the MPS. The MPS state is an SPT if the projective measurement is -1 , and is a trivial symmetric state if it is $+1$. The symmetries of interest are broken if it is 0. The results of the projective representation measurement are presented in Fig. 4.4(b).

This conventional technique to detect SPT order, however, fails to distinguish between the two SPT phases in the half-integer spin Kitaev ladder, as it maps the two-leg ladders into 1D chains, compressing some information and losing the distinction between SPT- x and SPT- y . We now show that they are, in fact, distinct phases.

Considering just the effective cluster model derived in the X - and Y -limits using perturbation theory, $H \propto \tau^z \tau^x \tau^z$, the protecting symmetry group is $\mathbb{Z}_2 \times \mathbb{Z}_2$ and the corresponding SPT classification is \mathbb{Z}_2 ; in other words, there is one SPT phase and one trivial phase. [84] Then how can there be two different SPT phases, in addition to a trivial phase?

The answer lies in the mapping from the original spin ladder to the effective cluster model, as discussed in the section for half-integer X -lim. Although the effective model is the same in each case, the protecting $\mathbb{Z}_2 \times \mathbb{Z}_2$ symmetry groups are not. Or, more precisely, some pre-images of $\mathbb{Z}_2 \times \mathbb{Z}_2$ in the X -limit are different from some pre-images in the Y -limit, and we can show using SOPs that these different symmetry groups do indeed protect the respective SPT phases.

In particular, one candidate $\mathbb{Z}_2 \times \mathbb{Z}_2$ symmetry group that could protect the SPT- x phase is $\Sigma_u^X \Sigma_l^Y \times \Sigma_u^Z$, with a corresponding SOP $O_x = e^{i\pi S_1^x} \left(\prod_{n=1}^N e^{i\pi S_{4n-2}^z} e^{i\pi S_{4n-1}^z} \right) e^{i\pi S_{4N}^x}$, illustrated in the inset of Fig. 4.5. As shown in the figure, this SOP identifies SPT- x as an SPT phase and SPT- y as trivial. On the other hand, a corresponding candidate $\mathbb{Z}_2 \times \mathbb{Z}_2$ group that could protect SPT- y is $\Sigma_u^X \Sigma_l^Y \times \Sigma_l^Z$, with a corresponding SOP $O_y = e^{i\pi S_2^y} \left(\prod_{n=1}^N e^{i\pi S_{4n-3}^z} e^{i\pi S_{4n}^z} \right) e^{i\pi S_{4N-1}^y}$. As we again show in Fig. 4.5, this SOP identifies the SPT- y phase as an SPT and the SPT- x phase as trivial. We provide further insights into the construction process of such SOPs, in particular into ambiguity in defining them due to the local symmetries of the Hamiltonian.

As an additional perspective, note that the local Hilbert space here is spin-1/2, which is in the projective representation of any global symmetry; notably, on a single site the two

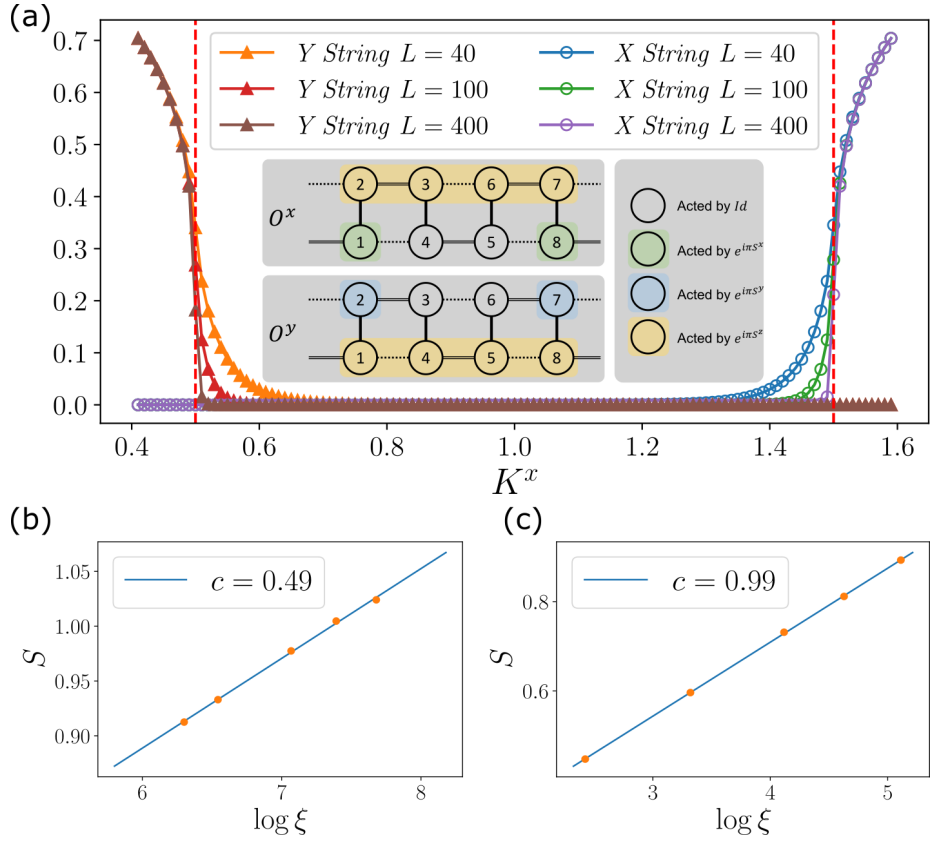


Figure 4.5: (a) Distinction between two SPT orders along the line $K_x + K_y = 2, K_z = 1$. The x -axis labels the value of K^x and $K^y = 2 - K^x$. In the inset we depict the distinction between the two SOPs for the two SPT phases. (b) Using finite-entanglement scaling to estimate the central charge $c = 0.5$ of the transition point at $K = (1.5, 0.5, 1.0)$. (c) Using finite-entanglement scaling to estimate the central charge $c = 1.0$ of the transition point at $K = (1.0, 1.0, 0)$.

generators of the protecting symmetry group $\Sigma_u^X \Sigma_l^Y \times \Sigma_u^Z$ anti-commute. To relate to the physics of a known SPT phase, two spin-1/2 must be combined into a linear representation, also guaranteeing that the symmetry group generators commute. Specifically, spins on the x -bond (y -bond) can be combined into X -dimers (Y -dimers), transforming SPT- x (SPT- y) into a topological phase while SPT- y (SPT- x) becomes topologically trivial.

In the phase diagram, there is a single point $K_z = 0, K_x = K_y$ where the two phases meet, and two simultaneous phase transitions occur: X dimers transition from trivial to SPT, and Y dimers transition from SPT to trivial. This could be interpreted as two co-existing $c = 0.5$ gapless phase transitions, together resulting in the observed $c = 1$ gapless phase transition [see Fig. 4.5].

Phase transitions The exact solvability of the spin-1/2 Kitaev ladder allows us to determine the nature of the phase transitions by studying the ground state energy and its derivatives as a function of \mathbf{K} . We show the analytically computed first and second derivatives across the SSB-SPT transition in Fig. 4.4 (d); we also show in the same figure the energy derivatives computed from DMRG, which agree precisely with the exact results, thus confirming the accuracy of our numerical simulations.

The SSB-SPT transition is evidently second-order, as we see both from the discontinuity of second-order energy derivatives and from the diverging correlation length (Fig. 4.4(c)). The nature of the transition can be determined more precisely by fitting the central charge according to the finite-scaling formula $S = \frac{c}{6} \log \xi + a$ [63]. As shown in Fig. 4.5 (b) we find $c = 0.5$.

As discussed before, the transition between SPT- x and SPT- y is also continuous, but $c = 1$ since it should be regarded as a superposition of two $c = 0.5$ transition.

Spin-1 Kitaev Ladders

For spin-1 Kitaev ladders, we find a very different phase diagram. As shown in Fig. 4.6, there are only SSB and trivial paramagnetic phases. These numerical results are consistent with the prediction of perturbation theory, namely that there are only trivial phases in the anisotropic limits.

Phase classification Recall from Eq. (4.15) we have concluded that the effective Hamiltonian in the large- Z limit is given by the combination of τ_i^x and $\tau_i^x \tau_{i+1}^x$ along with coefficients α and β , respectively; by explicit calculation of all contributions up to 4th order

terms, we find that the coefficients for spin-1 are $\alpha = -(K_x^4 - \frac{18}{7}K_x^2K_y^2 + K_y^4)/K_z^3$ and $\beta = -5K_x^2K_y^2/K_z^3$. This predicts a first-order transition between different product states, $|+\rangle_x^{\otimes N} \leftrightarrow |-\rangle_x^{\otimes N}$, where $|+\rangle_x$ and $|-\rangle_x$ are the ± 1 eigenstates of τ^x , respectively. The transition occurs when $\alpha(K)$ changes sign, at $\tan \phi = K_x/K_y = \sqrt{\frac{1}{7}(9 \pm 4\sqrt{2})} = 1.44$ and 0.69 . Converting τ^x back to the original model, we get the operator $e^{i\pi S_0^x} e^{i\pi S_1^x}$ or equivalently $-e^{i\pi S_0^x} e^{i\pi S_1^y}$; we show the expectation value of the latter operator in Fig. 4.6(b), and the first order transition is immediately apparent in the Z -limit, at $\theta \approx \frac{\pi}{2}$.² Alternatively, we can observe the transition by computing the overlap, $f_{\pm} = |\langle \psi | d_{z,\pm} \rangle|$, of the MPS ground state from DMRG with two dimer states

$$|d_{z,\pm}\rangle = \otimes_{\langle ij \rangle_z} \frac{1}{2} \left(|+\rangle_i |-\rangle_j \pm |-\rangle_i |+\rangle_j \right), \quad (4.16)$$

which are precisely the product states $|+\rangle_x^{\otimes N}$ and $|-\rangle_x^{\otimes N}$ in the effective model from perturbation theory. The overlaps are shown in Fig. 4.6(d).

Unlike in the case of spin-1/2, for spin-1 we also find a phase that is not present in the effective models from perturbation theory. As shown in Fig. 4.6(a), the order parameter $\langle S_0^x S_1^y \rangle$ reveals an SSB phase around the isotropic point. We note that, while this is the same operator used to detect SSB in the spin-1/2 case, there it also corresponded to τ^y in the perturbative model in the Z -limit, whereas here it becomes the zero operator in any anisotropic limit.

Phase transitions The unnecessary phase transition between trivial phases is first-order, as verified by directly measuring the expectation value of τ^x as in Fig. 4.6.

Spin-3/2 Kitaev Ladders

Phase classification As predicted in the perturbation theory for arbitrary half-integer spin- S Kitaev ladder, the phase diagram for spin-3/2 is quite similar to that of spin-1/2: we again have SSB, SPT- x , and SPT- y phases.

To detect the SSB order, we again use the order parameter $\langle \tau^y \rangle$. For spin-1/2 this order operator happens to be the simple $S^x S^y$ but for spin-3/2 it is $e^{i\pi S^x} e^{i\pi S^y}$. Order parameter measurements are summarized in Fig. 4.7 (a).

²Note that, although $\langle \tau^x \rangle = \langle -e^{i\pi S_0^x} e^{i\pi S_1^y} \rangle$ shows the unnecessary phase transition, it commutes with all global symmetries and is thus not an order parameter.

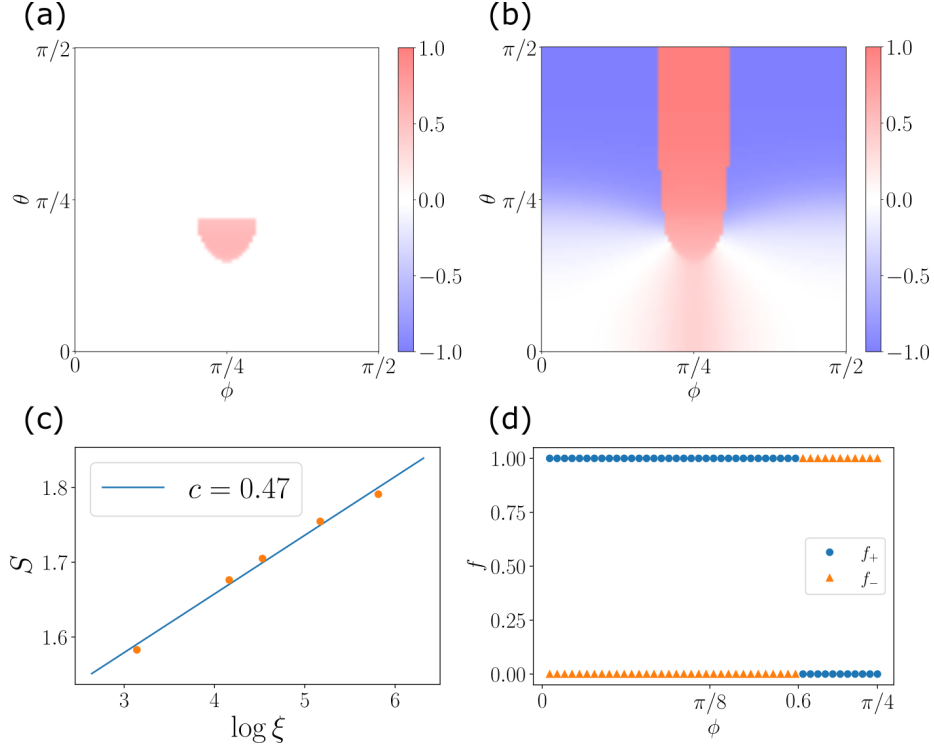


Figure 4.6: Phase Diagram of Spin-1 Kitaev Ladder. The phase diagrams are found using a 4-site iMPS with $\chi = 64$. (a) SSB phase indicated by the order parameter $\langle S^x S^y \rangle$. (b) The value of $\langle e^{i\pi S^x} e^{i\pi S^y} \rangle$ in the phase diagram. (c) Using finite-entanglement scaling to estimate the central charge of the phase transition point near $K = (1.4, 1.4, 1.0)$ between the SSB and trivial phases. (d) Overlaps between GS and two different dimer product states change suddenly at the first order phase transition around $\phi = 0.6$ with $\tan \phi = 0.69$ as predicted while the value of θ is close to $\pi/2$.

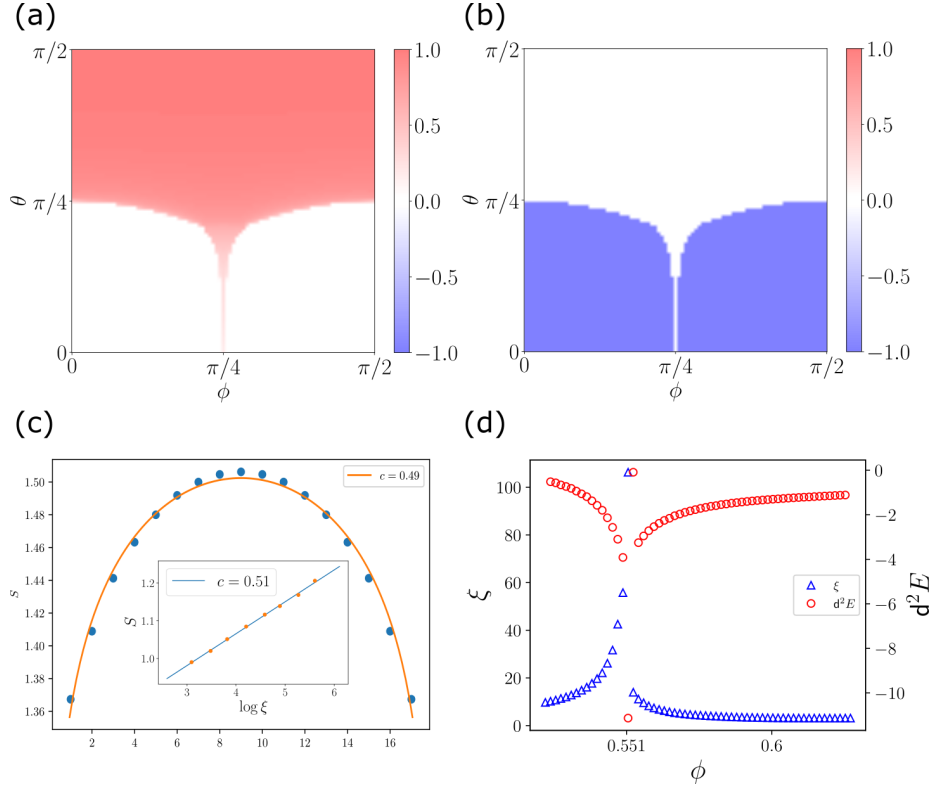


Figure 4.7: Phase diagram of spin-3/2 ladders. The phase diagrams are given by a 4-site iMPS with $\chi = 128$. (a) Order parameter $\langle e^{i\pi S^x} e^{i\pi S^y} \rangle$. (b) Pollmann-Turner order parameter for SPT order [64]. (c) Central charge estimation at a critical point $\theta = \frac{2}{9}\pi$, $\phi = 0.55$, giving $c \approx 0.5$. (d) Correlation length ξ and second derivative of energy $d^2 E/d^2 \phi$ along $\theta = \frac{2}{9}\pi$.

The SPT phases look the same in the perturbative limits for all half-integer spin- S cases. Thus projective representations are detected by exactly the same technique on the same set of symmetries as in the spin-1/2 case. SPT order measurement results are summarized in Fig. 4.7 (b).

Phase transitions In comparison with the spin-1/2 phase diagram, now the critical lines between SSB and SPT sit much closer to each other and the SSB phase is smaller when approaching the point $K^z = 0$, $K^x = K^y$. From Fig. 4.7 (d) we can see that the correlation length peaks near the critical point, and that there is a discontinuity of the second-order energy derivative as for spin-1/2. Together, these show that the transition is again second

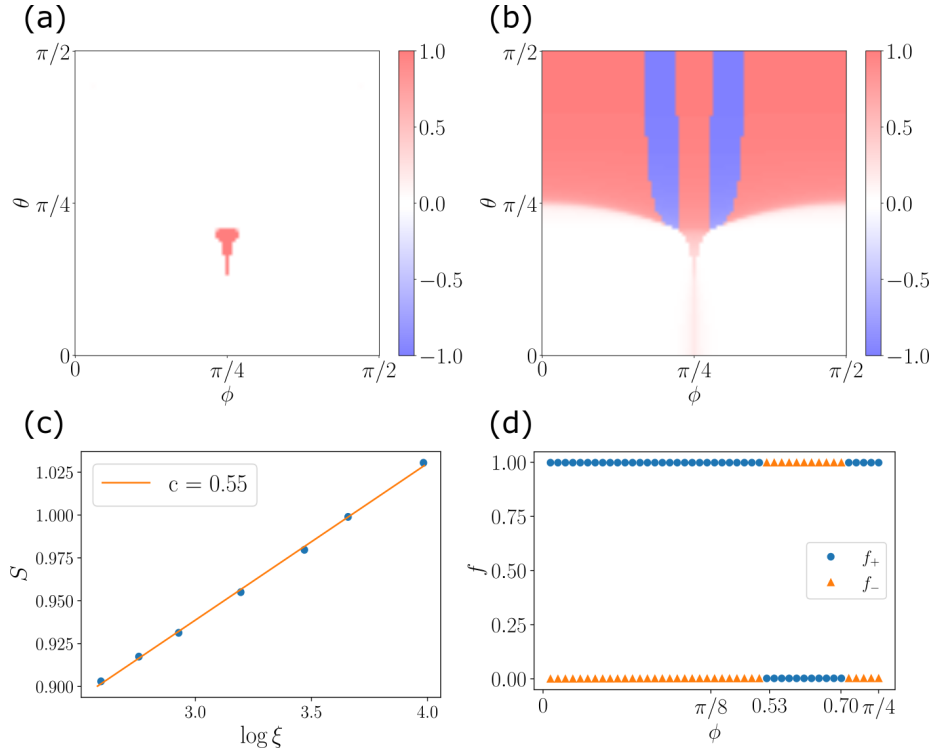


Figure 4.8: Phase Diagram of Spin-2 Kitaev Ladder. The phase diagrams are given by a 4-site iMPS with $\chi = 128$. (a) The phase diagram given by the order parameter $\langle S^x S^y \rangle$. (b) The value of $\langle e^{i\pi S^x} e^{i\pi S^y} \rangle$ in the phase diagram. (c) Central charge estimation at a transition point. (d) Overlaps between GS and two different dimer product states change suddenly at the first order phase transition points around $\phi = 0.53$ and $\phi = 0.70$ while the value of θ is close to $\pi/2$

order. As shown in Fig. 4.7 (c) both iDMRG and fDMRG give the same fitting of central charge $c = 0.5$.

Spin-2 Kitaev Ladders

Similarly to the case of spin-1, there are different trivial phases smoothly connected to product states of dimers, again with first-order unnecessary phase transitions. Also, the same SSB phase as in the spin-1 case exists in the central region, although the phase is much smaller for spin-2. The computed SSB order parameter and observable indicating the unnecessary phase transitions are shown in Figs. 4.8(a) and (b), respectively. The

unnecessary phase transitions are also observable from the overlap with different dimer product states, shown in Fig. 4.8(d).

Additionally, the transition between the trivial phases and the SSB phase again has central charge $c = 0.5$, as in the case of spin-1. The finite-entanglement scaling to determine c is shown in Fig. 4.8(c).

We note the interesting fact that Fig. 4.7(a) and Fig. 4.8(b) are quite visually similar, even though in the former the dividing line between red and white regions shows a distinct phase transition between SSB and SPT order and in the latter it shows a smooth (albeit step) change in an expectation value within a single phase. The apparent correspondence may be due to the expected convergence of integer and half-integer behavior in the classical large- S limit.

4.3 Summary

In this work, we have analyzed the general behaviors of higher-spin Kitaev ladders and concluded that for half-integer spins they have phases with SSB and SPT order with an Ising-like transition between them, and that for integer spins there are SSB and trivial phases in the phase diagram. The phases in the half-integer case can be understood through perturbation theory, as can the trivial phase in the integer case. Numerical results from analytical solutions and DMRG simulations on finite and infinite ladders confirm the results of perturbation theory, find the SSB phase for integer spins, and identify further detailed properties of the phase diagrams. With this combination of different theoretical and numerical methods, we provide a thorough and conclusive analysis on general features of spin- S Kitaev ladders.

For several values of S , we investigate the transitions between different phases by finite-entanglement scaling, and we identify both first-order and second-order phase transitions: the transitions between trivial phases are first-order and the transitions between SSB and SPT/trivial are second-order. Most of the second-order phase transition points are Ising-like with central charge $c = 0.5$. The exception is the transition between distinct SPT phases, distinguished by SOPs, which has $c = 1$.

Finally, we turn to the question of what our results imply for the full 2D Kitaev honeycomb model with higher spin. We work by analogy: we relate the spin-1/2 ladder and spin-1/2 honeycomb, and we hypothesize an analogous relationship between higher-spin ladders and higher-spin honeycombs, allowing us to predict the behavior of the latter from the former.

We first note that perturbation theory in the anisotropic limits of the spin-1/2 Kitaev honeycomb gives the toric code model, as shown by Kitaev in the original paper [40], and recently demonstrated on the spin- S honeycomb was given recently [53]. In fact, the toric code is the 2D analogue of the cluster model we found in the half-integer-spin ladders in the X -limit, thus suggesting that the behavior in the X -limit of our model carries over to 2D while the Z -limit behavior does not. We find that on the ladder, the spin-3/2 case exhibits the same cluster model SPT phases as in spin-1/2, and in fact they are stabilized by the higher spin, covering a larger portion of the phase diagram. We thus surmise that on the full honeycomb, phases with gapped \mathbb{Z}_2 topological order will be present in the anisotropic limits for higher half-integer spin just as for spin-1/2, and indeed they will reach farther towards the isotropic point. On the other hand, since the SSB phase appears in the spin-1/2 ladder but does not appear at all in the spin-1/2 honeycomb model, there is no good reason to think it would appear in higher-spin honeycomb models either. We

cannot make a clear prediction for the isotropic point itself, as there is no clear analogue for the ladder.

For integer spin, if we again assume that the X -limit of the ladder is analogous to the anisotropic limits of the honeycomb, we can predict trivial phases in all anisotropic limits, smoothly connected to product states of dimers along the corresponding strongest bonds. Unlike for half-integer spin, we find an SSB phase distinct from any anisotropic limit in a small region around the isotropic point on both spin-1 and spin-2 ladders. We also confirmed that the SSB at the isotropic point survives in the large- S limit by computing up to spin-4 and observing convergence of the SSB order parameter with increasing spin. It is not clear whether or not this SSB phase would carry over to the integer-spin honeycomb models.

Chapter 5

Heisenberg Ladder

Motivation

The Quantum Heisenberg model, pioneered by Werner Heisenberg in 1928, stands as a fundamental paradigm in the theoretical investigation of magnetic systems within the quantum mechanical framework. This model transcends the simplistic binary spin states of its predecessor, the Ising model, by introducing quantum operators that act on spins in a multi-dimensional Hilbert space. This sophisticated approach offers a more nuanced and realistic representation of magnetic interactions at the quantum level.

A key strength of the Heisenberg model lies in its remarkable versatility. By incorporating variable coupling strengths across different spatial dimensions (X, Y, Z), it can capture a wide array of magnetic behaviors and phenomena. This flexibility allows researchers to explore systems ranging from isotropic interactions, where coupling strengths are uniform, to highly anisotropic scenarios, where certain spatial directions dominate the magnetic behavior.

The model's adaptability extends to its applicability across various physical systems and phenomena:

- **Ferromagnetism and Antiferromagnetism:** The model provides insights into the fundamental mechanisms underlying these basic forms of magnetic ordering.
- **Quantum Phase Transitions:** It serves as a testbed for studying transitions between different quantum states at zero temperature, driven by quantum fluctuations rather than thermal effects.

- **Topological Phases:** The model has been instrumental in exploring exotic states of matter characterized by global properties rather than local order parameters.
- **Spin Liquids:** It offers a framework for investigating these enigmatic states where magnetic moments refuse to order even at the lowest temperatures.

A particularly noteworthy aspect of the Quantum Heisenberg model is its exact solvability in certain configurations. The one-dimensional spin-1/2 system, solvable via the Bethe ansatz, stands as a prime example. This rare instance of exact solvability in a non-trivial quantum many-body system provides profound insights into quantum criticality and the behavior of magnetic systems at critical points. It serves as a valuable benchmark for numerical techniques and approximation methods applied to more complex, non-integrable systems.

The model's significance extends beyond pure theoretical interest. It has practical applications in various fields:

- **Condensed Matter Physics:** For understanding and predicting the behavior of real magnetic materials.
- **Quantum Computing:** In the design and analysis of quantum bits (qubits) and quantum gates.
- **Spintronics:** For developing novel electronic devices that exploit electron spin.
- **Quantum Simulation:** As a target model for quantum simulators, both analog and digital.

Furthermore, the Heisenberg model serves as a fertile ground for developing and testing advanced computational techniques in quantum many-body physics. Methods such as Density Matrix Renormalization Group (DMRG), Quantum Monte Carlo, and various tensor network approaches have been honed through their application to this model.

In conclusion, the Quantum Heisenberg model not only enriches our fundamental understanding of quantum magnetism but also serves as a cornerstone in modern physics for exploring the intricate dynamics of spins and their entanglement properties in magnetic systems. Its contributions are pivotal in bridging theoretical research with practical applications, spanning from fundamental quantum mechanics to cutting-edge technologies in quantum information science. As we continue to push the boundaries of our understanding of quantum systems, the Heisenberg model remains an indispensable tool, consistently offering new insights and challenges to the scientific community.

5.1 Definitions and Framework

In our model, we explore a specific configuration of a quantum ladder where each leg is akin to a Heisenberg chain. The Hamiltonian for this system encapsulates various interactions among the spins located on adjacent sites, including both intra-leg (along the same leg) and inter-leg (between the legs) interactions. The Hamiltonian is defined as follows:

$$H = \sum_{\langle ij \rangle \in \text{intra-AFM}} J_{\text{AFM}} \vec{S}_i \cdot \vec{S}_j - \sum_{\langle ij \rangle \in \text{intra-FM}} J_{\text{FM}} \vec{S}_i \cdot \vec{S}_j + \sum_{\langle ij \rangle \in \text{inter}} J_{\text{inter}} \vec{S}_i \cdot \vec{S}_j \quad (5.1)$$

In this expression:

- The first term sums over all antiferromagnetic (AFM) intra-leg interactions, where J_{AFM} is the coupling constant for antiferromagnetic coupling between spins on the same leg.
- The second term accounts for all ferromagnetic (FM) intra-leg interactions, with J_{FM} as the ferromagnetic coupling constant.
- The third term represents the ferromagnetic inter-leg interactions, also using the J_{FM} coupling constant, but this time between spins on different legs.

This Hamiltonian structure allows us to dissect and analyze the magnetic properties and phase behaviors exhibited by the ladder system under different coupling scenarios and configurations.

5.2 Phase Diagram

To commence our detailed analysis, we leverage the Matrix Product Operator (MPO) framework as depicted in Equation (5.1), which is central to our approach for modeling quantum spin systems. Utilizing the robust Density Matrix Renormalization Group (DMRG) technique, we meticulously explore the multidimensional parameter space that characterizes the Heisenberg spin ladder models. This methodology is aligned with established practices in the study of Kitaev systems, ensuring that our results are both consistent and comparable with prior research.

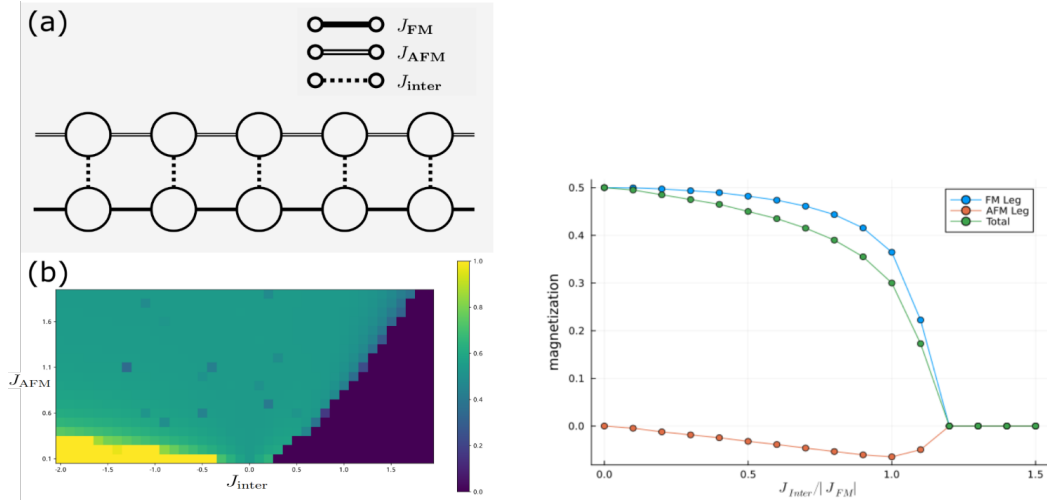


Figure 5.1: **Phase Diagram of Heisenberg Ladders:** Panel (a) presents a schematic representation of the Heisenberg ladder with various interaction parameters: J_{FM} for ferromagnetic, J_{AFM} for antiferromagnetic, and J_{inter} for inter-chain interactions. Panel (b) displays the resulting phase diagram obtained from our DMRG computations. The diagram includes a color map illustrating the stability regions of different magnetic phases as a function of interaction ratios; the parameter J on the x -axis represents the strength J_{inter} and J_2 for J_{AFM} . The accompanying graph quantitatively depicts the magnetization curves across these phases, highlighting transitions such as from ferromagnetic to spin liquid states.

5.2.1 Ground State Configuration and Magnetic Properties

Upon accurately determining the ground state configurations via DMRG, our next objective is to comprehensively assess the magnetic properties across various phases of the spin system. These assessments adhere to standard protocols used in prior research, facilitating the benchmarking and validation of our results against historical data. This systematic analysis helps in understanding the intricate magnetic behaviors exhibited by Heisenberg ladders under different interaction strengths and geometrical configurations.

In Figure 5.1 (b), the analysis of the two-leg Heisenberg ladder system reveals a rich family of magnetic behaviors across different regions of the phase diagram. For convenience, fixing $J_{\text{FM}} = 1$, these behaviors are influenced by J_{inter} and J_{AFM} . Three distinct phases have been identified:

1. **Ferromagnetic (FM) Order** (yellow region, low J_{inter} and J_{AFM}):

- This phase is characterized by strong ferromagnetic alignment, especially pronounced in one leg of the ladder.
 - Both FM leg and AFM leg exhibit polarized magnetization.
2. **Disordered Phase** (dark purple region, high J_{inter}):
- Both FM and AFM legs show a complete drop in magnetization, indicating a quantum disordered state.
 - This phase is likely a singlet state, driven by strong frustration and competing dimer interactions at high inter-chain coupling.
3. **Luttinger Liquid Phase** (green region, intermediate J_{inter} and J_{AFM}):
- This phase serves as a transitional state between the FM order and the non-magnetic phase.
 - It displays characteristics typical of Luttinger liquids in quasi-one-dimensional systems, such as algebraically decaying correlations, which will be mentioned afterwards.
 - There is a gradual reduction in magnetization in the FM leg, hinting at the presence of gapless excitations and potential spin-charge separation.

Transitions between these phases occur as the inter-chain coupling increases, with a notable transition to the non-magnetic phase around $J_{\text{inter}} \approx 1.0$, evidenced by a sharp decline in magnetization. These observations underline the complex interplay between ferromagnetic and antiferromagnetic interactions within the ladder system, and how varying the strength of inter-chain coupling dramatically alters the system’s magnetic properties.

5.2.2 Gapless Phases and Central Charge Analysis

The Luttinger liquid phases in this model are of particular interest due to their unique quantum critical behavior. To characterize these gapless phases, we utilize our MPS results to investigate universal properties, with a focus on the central charge—a key indicator of the underlying conformal field theory.

Figure 5.2 illustrates the scaling of entanglement entropy (EE) against $\log \xi$, with ξ representing the correlation length or a comparable scale factor. Our analysis yields two critical insights:

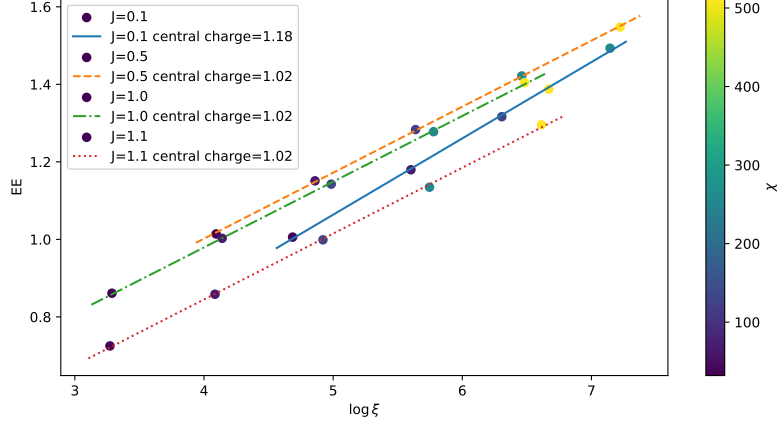


Figure 5.2: Entanglement entropy scaling for various J_{inter} values at $J_{\text{AFM}} = 1$. The slopes of these lines are used to extract the central charge c . For $J = 0.1$, we find $c \approx 1.18$, while for $J \geq 0.5$, the central charge much closer to $c \approx 1.0$.

1. **Luttinger Liquid Phase for $J \geq 0.5$:** The observed central charge approximates to $c \approx 1.02$, closely aligning with the theoretical value of $c = 1$ expected for a single-component Luttinger liquid phase. This alignment strongly supports the presence of gapless excitations and power-law decay of correlations typical of Luttinger liquids. The slight deviation from $c = 1$ is likely due to the finite-size effects inherent in MPS simulations and the limited sample size used in our calculations.
2. **Anomaly at $J = 0.1$:** At this lower coupling strength, the central charge increases to $c \approx 1.18$, indicating a potentially more complex phase or a deviation from the expected asymptotic behavior. This suggests a possible mixed phase or a regime that has not yet stabilized, highlighting the need for further investigation into this parameter region.

5.3 Dynamics and Luttinger Liquid

As a well-studied theory and well-observed phenomenon in Heisenberg chains, Luttinger liquids also have some key features to measure with fully-accessible wavefunctions.

5.3.1 Correlation Functions and Luttinger Parameter

In the study of Luttinger liquids, the decay of spin-spin correlation functions is a fundamental aspect used to characterize the phase and properties of the system. These functions typically follow a power-law behavior, indicative of the critical nature of Luttinger liquids. The mathematical expression for these correlation functions is as follows:

$$\begin{aligned}\langle S^z(x, 0)S^z(0, 0) \rangle &= C_1 \frac{1}{x^2} + C_2 (-1)^x \left(\frac{1}{x}\right)^{2K}, \\ \langle S^+(x, 0)S^-(0, 0) \rangle &= C_3 \left(\frac{1}{x}\right)^{2K+\frac{1}{2K}} + C_4 (-1)^x \left(\frac{1}{x}\right)^{\frac{1}{2K}}.\end{aligned}\tag{5.2}$$

Here, C_1 , C_2 , C_3 , and C_4 are constants that depend on the specifics of the spin chain, while K represents the Luttinger liquid parameter that describes the interaction strength and anisotropy effects within the system. This parameter K fundamentally influences the algebraic decay rates of the correlations, thus serving as a critical measure of the quantum critical behavior of the system.

To validate these theoretical predictions, we performed density matrix renormalization group (DMRG) simulations on a Heisenberg ladder with parameters $(J_{\text{AFM}}, J_{\text{FM}}, J_{\text{inter}}) = (1.0, 1.0, 1.0)$ and a bond dimension of $\chi = 600$. The results from these simulations are illustrated below:

The numerical analysis highlights the influence of the Luttinger parameter on the magnetic behavior of the system and provides significant insights into the underlying quantum phase transitions. Further investigations into different parameter regimes and higher bond dimensions could yield additional insights into the complex dynamics and critical phenomena inherent to low-dimensional quantum systems. Moreover, from the fit plotting, there is a good match between numerics and the theoretical formula used in Eq. (5.2).

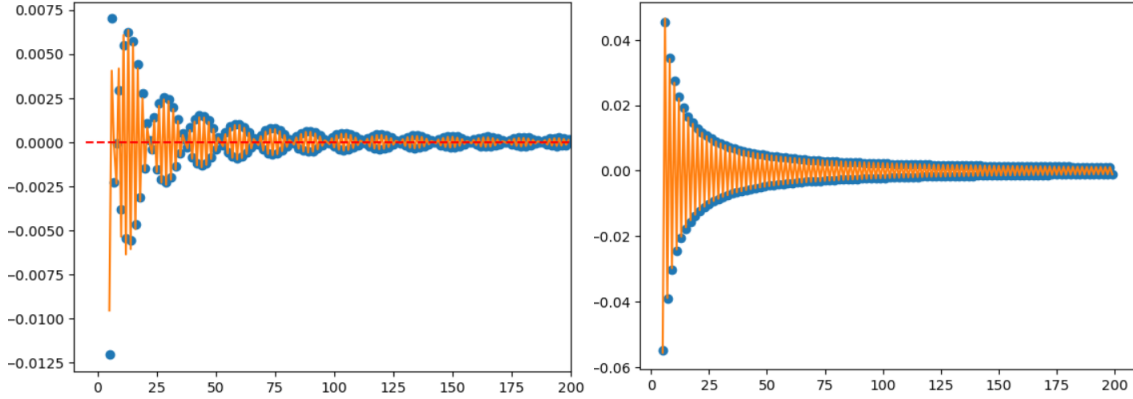


Figure 5.3: Correlation functions for a Heisenberg ladder. Blue dots are the sampled data points measured over the simulated MPS via DMRG; orange curves are fitted functions. Left: $\langle S^z(x, 0)S^z(0, 0) \rangle$. Right: $\langle S^+(x, 0)S^-(0, 0) \rangle$. The fitting results indicate a Luttinger parameter $K \approx 0.46$.

5.3.2 From Static Correlations to Dynamic Responses

The analysis of static correlation functions provides significant insight into the equilibrium properties of Luttinger liquids within the mixed spin ladder system. However, to gain a comprehensive understanding of the system’s response dynamics under various excitations, we employ Time-Evolving Block Decimation (TEBD) methods to study the dynamical structure factor, $S(k, \omega)$.

Dynamical Structure Factor

The dynamical structure factor is a fundamental measure in quantum many-body physics, offering crucial insights into the excitation spectrum of a system. It is particularly effective in revealing the nature of both collective excitations and individual quasiparticle dynamics. In the context of our mixed antiferromagnetic-ferromagnetic (AFM-FM) spin ladder, $S(k, \omega)$ allows us to probe the intricate dynamics that arise from the unique coupling configurations. The dynamical form structure $S(k, \omega)$ is obtained from the correlation function:

$$\chi^{\mathcal{O}}(x, t) = i\langle GS|\mathcal{O}^\dagger(x, t)\mathcal{O}(0, 0)|GS\rangle \rightarrow S^{\mathcal{O}}(k, \omega) = \text{Im}\chi^{\mathcal{O}}(k, \omega) \quad (5.3)$$

Numerically, unlike the TEBD introduced in 2.2.5, we first apply operator \mathcal{O} to the groundstate wavefunction and then perform time evolution with the algorithm of fourth

order time-evolving block decimation (TEBD4) to maximum time T_{\max} . Lastly, we compute the inner product of groundstate, operator $\mathcal{O}^\dagger(x, t)$ and the time-evolved excited state to obtain $\chi(x, t)$. The dynamical form structure can be computed following Fourier transformation¹:

$$S^{\mathcal{O}}(k, \omega) = \int_{-\infty}^{\infty} dt e^{i\omega t} \chi^{\mathcal{O}}(k, t) \quad (5.4)$$

$S_{\text{FM}}^\pm(k, \omega)$: Spin-Spin Correlation on the FM Leg

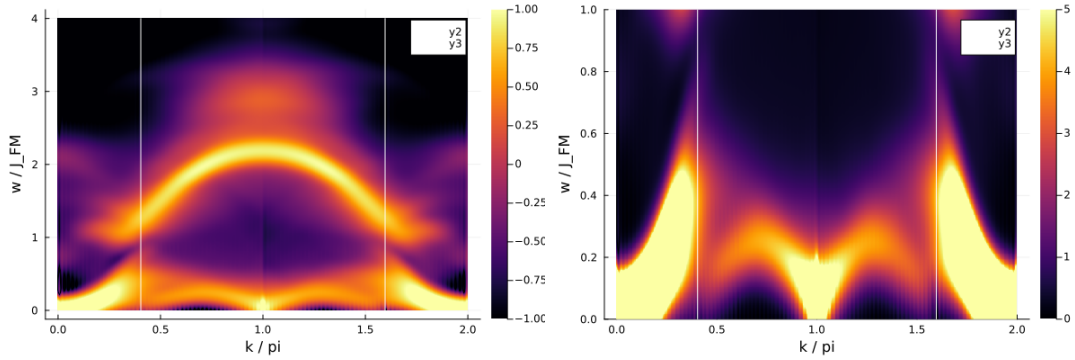


Figure 5.4: Dynamical structure factor $S_{\text{FM}}^\pm(k, \omega)$. The right panel is a zoomed-in version of the left panel, enhancing details. The left panel is presented on a log10 scale, while the right panel uses a linear scale.

Figure 5.4 depicts the dynamical structure factor for spin-spin correlations on the FM leg, characterized by the imaginary part of $\langle S^+ S^- \rangle$. Key observations from the analysis include:

- The $S_{\text{FM}}^\pm(k, \omega)$ shows periodicity in momentum with a period of 2π , confirming that translation symmetry within one unit cell is preserved.
- Zero-energy excitations are evident at specific momentum points:
 1. $k = 0$: Features a magnon with quadratic dispersion, indicative of traditional spin-wave theory.
 2. $k = \pi$: Exhibits a distinct mode characteristic of Luttinger liquid behavior, suggesting underlying complex interactions.

¹The error is on the order of one percent.

3. $k = \pi \pm 2k_F$: Marks another Luttinger liquid mode, significant for its implications on the spin structure. Here, $2k_F = 2\pi M_z \bmod 2\pi$, where M_z denotes the magnetization per unit cell.
- The dispersion relations do not extend across the entire Brillouin zone, highlighting localized interactions.

$S_{\text{AFM}}^{\pm}(k, \omega)$: **Correlation on the AFM Leg**

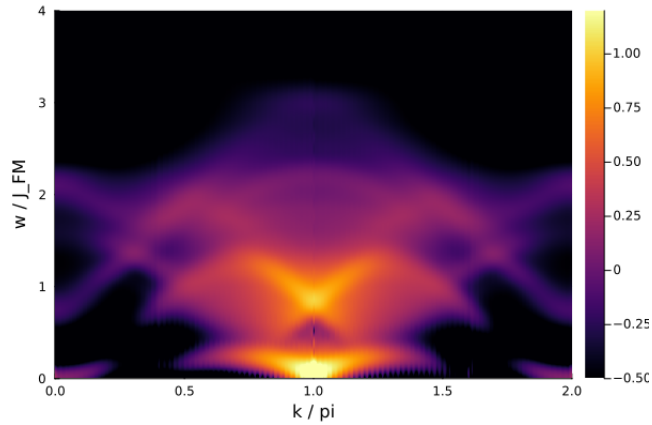


Figure 5.5: Dynamical structure factor $S_{\text{AFM}}^{\pm}(k, \omega)$ displayed on a log10 scale, highlighting the complex high-energy excitations distinct to the AFM leg.

Despite the richer high-energy excitations, the low-energy characteristics of $S_{\text{AFM}}^{\pm}(k, \omega)$ closely resemble those observed on the FM leg, as shown in Figure 5.5.

$S_{\text{FM}}^{zz}(k, \omega)$: **z -Component Correlation on the FM Leg**

Figure 5.6 explores the dynamical structure factor for z -component correlations, where the zero-energy modes at $k = 0$ and $k = 2k_F$ suggest the presence of a Luttinger liquid. The quadratic mode observed at $k = \pi$, alongside a linear mode between $k = 0$ and $k = 2k_F$, points to complex, not yet fully understood dynamics.

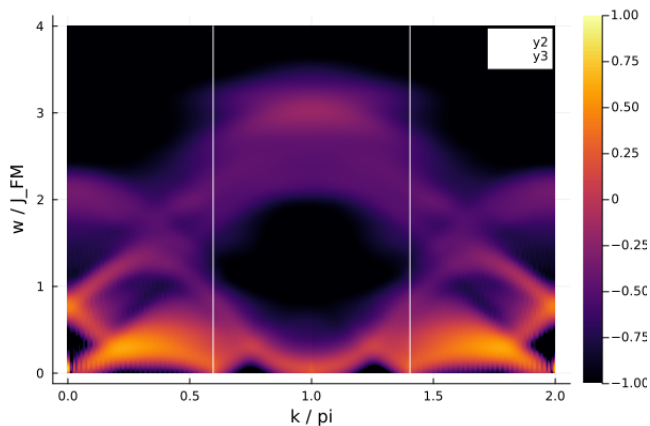


Figure 5.6: Dynamical structure factor $S_{\text{FM}}^{zz}(k, \omega)$ in log10 scale, emphasizing the low-energy excitations and their dispersion characteristics.

$S_{\text{AFM}}^{zz}(k, \omega)$: z -Component Correlation on the AFM Leg

Figure 5.7 complements the findings from the FM leg by highlighting a different aspect of the Luttinger liquid continuum, with pronounced signals above the quadratic dispersion at $k = \pi$.

The computed dynamical structure factors elucidate the coexistence of magnons and Luttinger liquid characteristics within the mixed spin ladder system, revealing a complex interplay of excitations that extends beyond traditional magnon behavior. Particularly, the continuum bound by a quadratic dispersion at $k = \pi$ introduces an unconventional feature in the $S_z S_z$ correlation landscape, underscoring the need for further theoretical and experimental investigation to fully understand these phenomena.

5.4 Summary

This chapter delves into the multifaceted properties of the Heisenberg ladder, an extended model of the classic Heisenberg model which is known for its comprehensive portrayal of quantum magnetic interactions. Our investigation employed advanced numerical methods, particularly the Density Matrix Renormalization Group (DMRG) technique, to explore the intricate phase diagram and dynamical properties of the ladder system.

We introduced the Heisenberg ladder by specifying its Hamiltonian, which incorporates both intra-leg and inter-leg spin interactions. This model extends the conventional one-

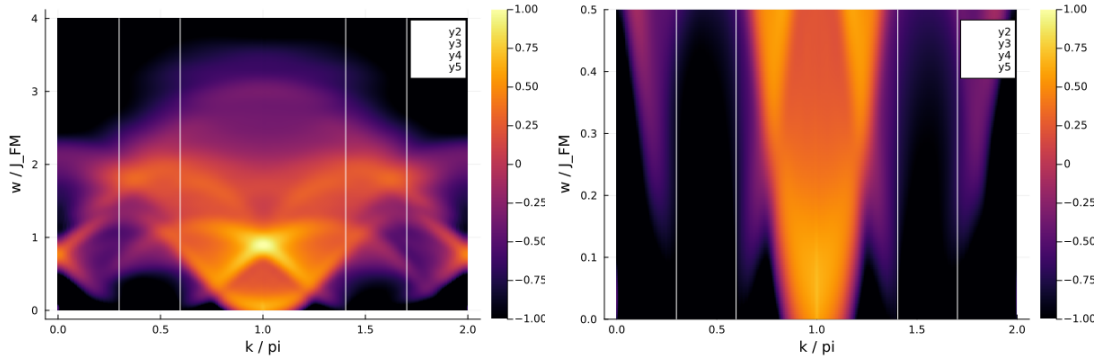


Figure 5.7: Dynamical structure factor $S_{\text{AFM}}^{zz}(k, \omega)$, presented in log10 scale. The zoomed-in view reveals detailed features of the excitation spectrum.

dimensional Heisenberg chain into a more complex two-leg ladder configuration, enabling the study of richer magnetic behaviors and interaction dynamics.

Our extensive computational analysis, supported by DMRG simulations, has revealed a rich phase diagram with distinct magnetic phases characterized by the interaction parameters J_{FM} , J_{AFM} , and J_{inter} . Key phases identified include Ferromagnetic Order, Luttinger Liquid Phase, and a Disordered Phase. Each phase exhibits unique magnetic properties and transitions that are sensitive to the interplay between ferromagnetic and antiferromagnetic interactions.

The Luttinger Liquid phase, observed at intermediate interaction strengths, is particularly noteworthy for its critical properties and gapless excitations. We quantitatively analyzed the entanglement entropy and central charge to confirm the Luttinger behavior. The dynamical structure factor studies provided deeper insights into the excitation spectrum, revealing how spin dynamics are modulated by quantum interactions within the ladder.

The findings from this chapter not only enhance our understanding of quantum magnetic systems but also contribute to the broader field of condensed matter physics by providing detailed insights into the effects of dimensional and interaction complexity on magnetic properties. These results are pivotal for both theoretical explorations and the design of experimental setups aimed at studying quantum magnetic phenomena in low-dimensional systems.

Overall, this study underscores the versatility of the Heisenberg model in modern physics and its potential in unlocking new avenues for research into quantum materials and technologies even after so many years of exploitation.

Chapter 6

Motzkin Chains

Motivation

Motzkin chains represent a sophisticated intersection of combinatorial mathematics and quantum mechanics, embodying a specialized class of spin-one chains that captivate researchers with their unique mathematical structure and intriguing physical properties. These models, rooted in the concept of Motzkin walks from combinatorial theory, offer a rich playground for exploring fundamental questions in quantum many-body physics.

Fundamental Characteristics

The construction of Motzkin chains is based on a one-to-one correspondence between steps in a Motzkin walk and quantum states within the chain. This mapping results in a Hamiltonian that is:

- **Local:** Interactions occur only between neighboring sites, mirroring the step-by-step nature of Motzkin walks.
- **Translationally Invariant in the Bulk:** Reflecting the uniform rules governing Motzkin walks away from boundaries.
- **Exactly Solvable:** Allowing for precise analytical treatments, a rarity in quantum many-body systems.

These properties, as elucidated in seminal works by Bravyi et al. [10] and Movassagh [57], position Motzkin chains at a unique vantage point in the landscape of quantum spin systems.

Quantum Properties and Significance

The ground state of Motzkin chains exhibits several remarkable features:

1. **Frustration-Free Nature:** The ground state minimizes the energy of each local term in the Hamiltonian simultaneously, a property that is both mathematically elegant and physically significant.
2. **Polynomially Closing Energy Gap:** Unlike typical gapped systems where the energy gap remains constant with system size, in Motzkin chains it diminishes polynomially, hinting at rich scaling behavior.
3. **Extensive Entanglement Entropy:** The entanglement entropy scales logarithmically with the chain length, defying the area law typically observed in one-dimensional gapped systems.

These properties collectively challenge conventional wisdom about one-dimensional quantum systems and highlight the potential complexities hidden within seemingly simple, frustration-free models.

Broader Implications and Future Directions

The significance of Motzkin chains extends far beyond their theoretical elegance:

- **Long-Range Entanglement:** They serve as a crucial platform for studying long-range entanglement in quantum systems, a key resource in quantum information processing.
- **Quantum Criticality:** The unusual scaling of the energy gap and entanglement entropy positions Motzkin chains as potential models for studying novel forms of quantum criticality.
- **Quantum Simulation:** Their exact solvability makes them ideal candidates for benchmarking quantum simulators and exploring the limits of quantum advantage.

- **Quantum Error Correction:** The unique entanglement properties of Motzkin states may inspire new approaches to quantum error-correcting codes.

Moreover, the Motzkin chain model acts as a bridge between abstract quantum theory and practical computational functionalities. Its rich entanglement features, combined with a robust mathematical foundation, offer insights into the design of quantum algorithms and the development of quantum memory devices.

As research in quantum technologies advances, Motzkin chains stand at the forefront, promising to illuminate the path towards harnessing complex quantum states for practical applications. Their study not only deepens our understanding of fundamental quantum mechanics but also paves the way for novel quantum technologies that exploit long-range entanglement and critical behavior.

6.1 Definitions and Framework

The Motzkin chain, in its mostly revised version, is defined as a spin-1 system with an even number of sites $N = 2n$. The Hamiltonian governing the dynamics and interactions within this chain is given by:

$$H = \sum_{j=1}^{2n-1} \Pi_{j,j+1} + \Pi_{\partial} \quad (6.1)$$

where $\Pi_{j,j+1}$ represents the local interaction terms between adjacent spins, and Π_{∂} encapsulates the boundary conditions at the ends of the chain.

6.1.1 Local Interaction Terms

The local term $\Pi_{j,j+1}$ in the Hamiltonian is detailed as:

$$\Pi_{j,j+1} := |D\rangle_{j,j+1}\langle D| + |U\rangle_{j,j+1}\langle U| + |\psi\rangle_{j,j+1}\langle\psi| \quad (6.2)$$

This expression consists of projectors onto three distinct types of states, each representing a different interaction or transition between the spins at positions j and $j + 1$:

- $|D\rangle$ and $|U\rangle$ typically symbolize 'down' and 'up' steps in the corresponding Motzkin walk representation.
- $|\psi\rangle$ represents a special state mixing both 'up' and 'down' characteristics.

The specific forms of these states are defined as follows:

$$\begin{aligned} |D\rangle &= \frac{1}{\sqrt{2}}(|0d\rangle - |d0\rangle) \\ |U\rangle &= \frac{1}{\sqrt{2}}(|0u\rangle - |u0\rangle) \\ |\psi\rangle &= \frac{1}{\sqrt{2}}(|00\rangle - |ud\rangle) \end{aligned} \quad (6.3)$$

Here, $|0\rangle$, $|u\rangle$, and $|d\rangle$ represent the zero, up, and down spin states, respectively. ¹

¹Usually there will be yet another parameter t as a tunable parameter that adjusts the amplitudes within these superpositions, influencing the quantum interference effects in the system. Here we omitted it due to the arrangement of future work in progress.

$$|u\rangle \equiv | + 1\rangle = \begin{pmatrix} 1 \\ 0 \\ 0 \end{pmatrix}, \quad |0\rangle = \begin{pmatrix} 0 \\ 1 \\ 0 \end{pmatrix}, \quad |d\rangle \equiv | - 1\rangle = \begin{pmatrix} 0 \\ 0 \\ 1 \end{pmatrix} \quad (6.4)$$

6.1.2 Boundary Conditions

The boundary term Π_{∂} is defined to incorporate asymmetry at the two ends of the chain, reflecting different physical conditions or constraints at these boundaries:

$$\Pi_{\partial} = |d\rangle_1 \langle d| + |u\rangle_{2n} \langle u| \quad (6.5)$$

This term applies a 'down' projector at the first site and an 'up' projector at the last site, effectively pinning the ends of the Motzkin walk to specific states, which is crucial for defining the overall ground state properties and the system's excitation spectrum.

6.1.3 Symmetry

Motzkin chain has a $U(1)$ symmetry, the same as many other spin models

$$S = \sum_{i=1}^{2n} S_i^z \quad (6.6)$$

Its commutation with Hamiltonian (6.1) can be revealed after converted to the usual spin basis.

6.1.4 Physical Meaning

The Hamiltonian of the Motzkin chain, though primarily composed of specialized projectors rather than the more commonly used spin operators, holds a clear and significant physical interpretation, especially when the parameter t is set to 1.

This model can be conceptualized as representing a restricted random walk. Imagine an agent that starts at the origin $(0, 0)$ on a Cartesian plane and is required to return to the x-axis at $(2n, 0)$ without ever crossing below it. Such constraints model the physical boundaries and behaviors dictated by the Hamiltonian:

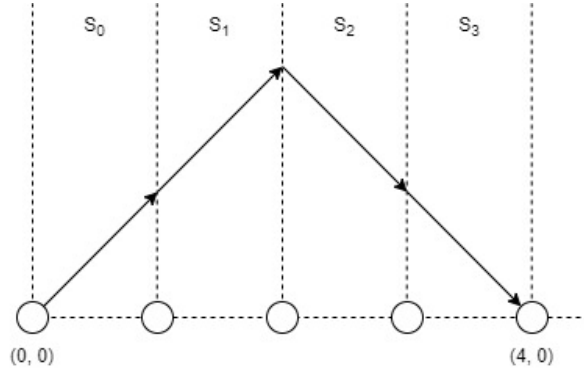


Figure 6.1: A Motzkin path in a Motzkin chain of length $2n = 4$

- At the starting point, represented by the left boundary of the Hamiltonian, any downward step is prohibited. This is reflected in the boundary term, which penalizes the downward state $|d\rangle$ at the first site, making it energetically unfavorable.
- Similarly, at the ending point, or the right boundary, upward steps are discouraged, leading to a boundary term that penalizes the upward state $|u\rangle$ at the last site.

Note that spin sites in our Hamiltonian do not correspond to the site positions in the Cartesian plane; instead, they correspond to the choices of the agent between two neighboring positions. In other words, spins live on the edges of the graph of this problem.

For the intermediate steps between these boundaries, the Hamiltonian captures the equivalence of possible sequences of movements. For example, the projector $|D\rangle$ ensures that there is no energetic preference between a sequence of a downward step followed by a stationary step and vice versa. This symmetry is similarly enforced for other combinations of moves through their respective projectors.

By establishing these projectors, the Hamiltonian effectively enforces the rules of the Motzkin walk, where the transitions between different states (steps) are strictly regulated to mimic the allowed movements of the agent on this hypothetical walk. Each projector in the bulk Hamiltonian, therefore, does not merely serve a mathematical function but illustrates a physical rule akin to the laws governing potential movements in a controlled random walk scenario.

This conceptual framework not only simplifies the understanding of the Hamiltonian's structure but also aligns with the physical analogies used in theoretical physics to model systems constrained by specific rules or boundaries. By interpreting the Motzkin chain in

this manner, we gain insight into how quantum systems can embody classical constraints, thereby bridging the connection between abstract quantum states and tangible physical processes.

6.1.5 Ground State

As a frustration-free Hamiltonian, the Motzkin chain has been shown to own a unique gapped ground-state. One may already expected that this state is immediately the superposition of all the possible path configuration of the randomwalk problem, and the fact is indeed as such.

Mapping the spin choices illustratively, the representation will be even more intuitive; here below are two simplest example of the grounds states of Motzkin chains, of length 2 and 4 respectively.

$$|\mathcal{M}_2\rangle = \frac{1}{\sqrt{2}}(|\rightarrow\rightarrow\rangle + |\nearrow\searrow\rangle). \quad (6.7)$$

$$\begin{aligned} |\mathcal{M}_4\rangle = & \frac{1}{\sqrt{9}}(|\rightarrow\rightarrow\rightarrow\rightarrow\rangle + \\ & |\nearrow\searrow\rightarrow\rightarrow\rangle + |\rightarrow\nearrow\searrow\rightarrow\rangle + |\rightarrow\rightarrow\nearrow\searrow\rangle + \\ & |\nearrow\searrow\nearrow\searrow\rangle + |\nearrow\rightarrow\searrow\rightarrow\rangle + |\rightarrow\nearrow\rightarrow\searrow\rangle + \\ & |\nearrow\rightarrow\rightarrow\searrow\rangle + \\ & |\nearrow\nearrow\searrow\searrow\rangle). \end{aligned} \quad (6.8)$$

It has been shown [10] that such states possess intricate entanglement properties. By examining a half-chain of spins designated as block A , we quantify entanglement through two principal metrics: the Schmidt rank and the entanglement entropy.

Schmidt Rank: The Schmidt rank, $\xi(A)$, which denotes the count of nonzero eigenvalues of the block's reduced density matrix ρ_A , exhibits a linear growth proportional to the system size, given by $1 + \frac{l}{2}$. This growth stems from unmatched brackets in block A , which correspond to their matching counterparts in the complementary block B . This aspect highlights profound long-range entanglement across the chain.

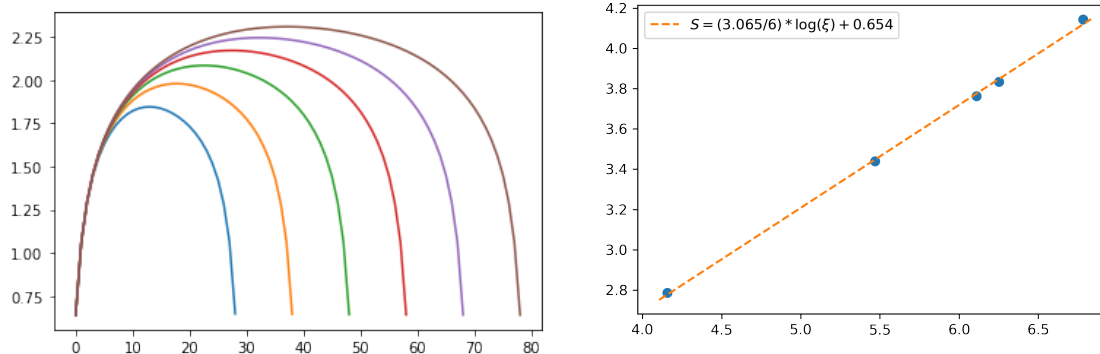


Figure 6.2: Increase of the entanglement entropy along a Motzkin chain, along with the increase of system size. Meanwhile, though not able to describe with conformal theory, Motzkin groundstate possess similar finite-size scaling behavior with a 'central charge' being 3.

Entanglement Entropy: The entanglement entropy adheres to the relation $S(A) = \frac{1}{2} \log_2 l + c_l$. Here, c_l approaches a constant as l increases, indicating a logarithmic increase in the state's complexity with the chain's length. Conceptually, this is analogous to the trajectories of a particle on a semi-infinite one-dimensional lattice, resembling a Brownian motion. The distribution of the particle's position m after $\frac{l}{2}$ steps explains the entropy's scaling. Further analysis reveals that the probability distribution p_m adjusts with size, aligning with $p_m \approx m^2 \exp\left(-\frac{3m^2}{l}\right)$ for large l .

6.2 Combinatorics, Exact MPS, and Orthogonal DMRG

Considering the inherent classical nature of the random walk model in the Motzkin chain, a precise and efficient method for computing all possible configurations becomes indispensable. In combinatorics and computer science, dynamic programming (DP) is a widely utilized approach to tackle problems that can be broken down into interrelated subproblems, allowing for a recursive solution. This method optimizes computation by reversing the recursive solutions and storing intermediate results, thus saving both time and computational resources.

For the Motzkin chain, we initially relax the constraint that the path must return to the starting position. Instead, we consider all possible paths from $(0, 0)$ to (i, j) , recording them in $DP[i, j]$. Recognizing that returning to $(2n, 0)$ is merely an extension of the precomputed DP array, we can effectively enumerate all possibilities within an open boundary condition (OBC) Motzkin chain of length $2n$ by examining the values up to $DP[n, n]$.

6.2.1 Calculating Motzkin Numbers

Motzkin numbers, the total number of different paths connecting two given positions, are a fundamental sequence in combinatorics, closely related to Catalan numbers and central to the study of Motzkin paths. In our search for GS of Motzkin chains, these numbers directly reflect the Schmidt values between each pair of spins. Below, we present a dynamic programming algorithm to calculate Motzkin numbers efficiently, followed by a discussion on their relevance to Matrix Product States (MPS) in the context of the Motzkin ground state.

Dynamic Programming Algorithm

The following pseudocode outlines an efficient dynamic programming approach to calculate the number of Motzkin paths for a given length $(2n)$, where (n) represents half the length of the Motzkin path.

This algorithm utilizes a 2D dynamic programming table to efficiently compute Motzkin numbers. The table $(DP[i][j])$ represents the number of Motzkin paths of length (i) that end at height (j) . The algorithm considers three possible steps at each position: up, down, and flat, accumulating the contributions from each valid step. The time complexity of this algorithm is $O(n^2)$, which is a significant improvement over naive recursive approaches that would have exponential time complexity.

Algorithm 1 The Dynamicl Programming Algorithm for Motzkin Paths/Numbers

```
1: function MotzkinNumber( $n$ )
2: Input:  $n$  - half the length of the Motzkin path
3: Output: Total number of Motzkin paths of length  $2n$ 
4: Initialize a 2D array  $DP$  with dimensions  $[2n + 1][n + 1]$  set to zero
5:  $DP[0][0] \leftarrow 1$  ▷ Base case: one path of length 0
6: for  $i \leftarrow 1$  to  $2n$  do
7:   for  $j \leftarrow 0$  to  $n$  do
8:     if  $j > 0$  then
9:        $DP[i][j] \leftarrow DP[i][j] + DP[i - 1][j - 1]$  ▷ Contribution from an up step
10:    end if
11:    if  $j + 1 \leq n$  and  $i - 1 \geq j + 1$  then
12:       $DP[i][j] \leftarrow DP[i][j] + DP[i - 1][j + 1]$  ▷ Contribution from a down step
13:    end if
14:     $DP[i][j] \leftarrow DP[i][j] + DP[i - 1][j]$  ▷ Contribution from a flat step
15:  end for
16: end for
17: return  $DP[2n][0]$ 
18: end function
```

Application to Matrix Product States

The Motzkin numbers and their associated paths have a profound connection to quantum many-body physics, particularly in the context of Matrix Product States (MPS). The MPS representation of the Motzkin ground state can be constructed using the insights gained from the Motzkin number calculation.

Schmidt Values in MPS Representation Using the dynamic programming algorithm presented above, we can calculate the Schmidt values in the MPS representation of the Motzkin ground state. This is achieved by computing the probability distribution of different feasible heights at each position in the Motzkin path. The Schmidt values provide crucial information about the entanglement structure of the quantum state.

Tensor Initialization The tensors in the MPS representation can be initialized based on the principles of random walks, which are closely related to Motzkin paths. The tensor elements can be defined as:

$$T_{v_i, v_{i+1}}^p = \delta(v_{i+1} - v_i - p) \quad (6.9)$$

where:

- $T_{v_i, v_{i+1}}^p$ is the tensor element
- v_i and v_{i+1} represent the heights at positions i and $i + 1$, respectively
- p denotes the step type (-1 for down, 0 for flat, 1 for up)
- δ is the Kronecker delta function

It's important to note that the feasible value range of v_i should be adjusted according to the corresponding maximum distance of the agent at position i , which has already been predicted by the DP table. This ensures that the paths remain valid Motzkin paths throughout the construction.

DMRG Solver and Ground State After constructing the initial MPS using the method described above, we can employ a Density Matrix Renormalization Group (DMRG) solver to obtain the final ground state in normalized canonical forms. Figure 6.3 illustrates this agreement by showing the Schmidt values on each bond of a Motzkin ground state MPS of length $2n = 60$. The logarithmic plot of Schmidt values reveals important features of the Motzkin ground state:

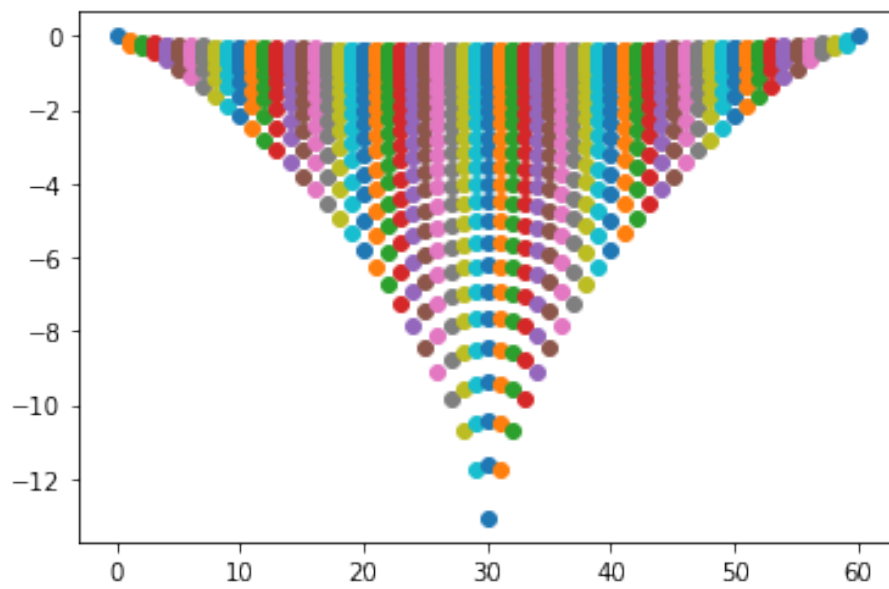


Figure 6.3: Schmidt values (logarithmic plot) on each bond of a Motzkin ground state MPS of length $2n = 60$. The plot demonstrates the characteristic entanglement structure of the Motzkin state, with higher Schmidt values near the center of the chain and lower values towards the ends.

- The Schmidt values exhibit a symmetric distribution, reflecting the symmetry of the Motzkin paths.
- The largest Schmidt values are found near the center of the chain, indicating stronger entanglement in this region.
- The Schmidt values decrease towards the ends of the chain, consistent with the boundary conditions of Motzkin paths.
- The overall distribution of Schmidt values provides insights into the area law of entanglement entropy in this system.

First Excited States

A noteworthy aspect of the Motzkin chain is its first excited states. While the ground state of the system can be exactly described, the exact forms of low-lying eigenstates remain challenging to determine. However, the Density Matrix Renormalization Group technique offers a solution, albeit with certain requirements. By adjusting the bond dimension and allocating sufficient computational resources, DMRG can be modified to effectively retrieve these low-lying states. This adaptation underscores the potential of DMRG to explore complex quantum states beyond the ground state, expanding our understanding of quantum systems modeled by Motzkin chains.

Generating the First Excited State

The process of obtaining the first excited state builds upon the ground state calculation and involves a technique called state-targeting or state-specific DMRG. Here's a detailed explanation followed by a pseudocode algorithm:

Explanation: Start with the ground state MPS obtained from the initial DMRG calculation. Implement orthogonality constraints to ensure the excited state is orthogonal to the ground state. Modify the DMRG optimization procedure to minimize the energy while maintaining orthogonality. Iterate the DMRG sweeps until convergence to obtain the first excited state.

The key challenge is maintaining orthogonality to the ground state while optimizing for the lowest energy state in the orthogonal subspace. This is typically achieved through a projection technique.

Algorithm 2 First Excited State Generation using Modified DMRG

Note: This algorithm uses the same MPS representation for both the ground state and the excited state, ensuring they are in the same basis. The orthogonality to the ground state is enforced by the projector P , which is an alternative to state-averaged decimation methods.

```
1: Input: Ground State MPS  $|\psi_0\rangle$ , Hamiltonian  $H$ , max bond dimension  $\chi$ 
2: Output: First Excited State MPS  $|\psi_1\rangle$ 
3: Initialize  $|\psi_1\rangle$  as a random MPS with bond dimension  $\chi$ 
4:  $E_0 \leftarrow \langle \psi_0 | H | \psi_0 \rangle$  ▷ Ground state energy
5: while not converged do
6:   for each site  $i$  do
7:      $|\phi\rangle \leftarrow$  local tensor at site  $i$  of  $|\psi_1\rangle$ 
8:      $H_{\text{eff}} \leftarrow$  effective local Hamiltonian around site  $i$ 
9:      $P \leftarrow I - |\psi_0\rangle\langle\psi_0|$  ▷ Projector orthogonal to GS
10:     $H_{\text{proj}} \leftarrow PH_{\text{eff}}P$  ▷ Projected Hamiltonian
11:    Solve eigenvalue problem:  $H_{\text{proj}}|\phi'\rangle = E|\phi'\rangle$ 
12:    Update local tensor of  $|\psi_1\rangle$  with  $|\phi'\rangle$ 
13:    Perform SVD and truncate to bond dimension  $\chi$ 
14:  end for
15:   $E_1 \leftarrow \langle \psi_1 | H | \psi_1 \rangle$ 
16:  if  $|E_1 - E_{\text{prev}}| < \epsilon$  then
17:    converged  $\leftarrow$  true
18:  end if
19:   $E_{\text{prev}} \leftarrow E_1$ 
20: end while
21: return  $|\psi_1\rangle$ 
```

Key Points: The algorithm starts with a random MPS for the excited state and the pre-computed ground state. The projector $P = I - |\psi_0\rangle\langle\psi_0|$ ensures orthogonality to the ground state. The effective Hamiltonian is projected into the subspace orthogonal to the ground state. The local optimization problem becomes an eigenvalue problem in the projected subspace. SVD truncation maintains the desired bond dimension χ . The process continues until the energy converges within a specified tolerance ϵ .

Implementation Considerations: Efficient implementation of the projection operation is crucial for performance. The choice of initial random state can affect convergence speed. Higher bond dimensions may be necessary for accurate representation of excited states. Multiple runs with different initial states can help ensure the true first excited state is found.

Verification: After obtaining the first excited state, it's important to verify:

Orthogonality to the ground state: $\langle\psi_0|\psi_1\rangle \approx 0$ Energy gap: $E_1 - E_0 > 0$ and consistent with theoretical predictions Entanglement properties: Compare Schmidt values with those of the ground state

This modified DMRG approach allows for the systematic exploration of low-lying excited states in the Motzkin chain, providing valuable insights into the spectral properties and excitation dynamics of this intriguing quantum system. To get more than first excited states, one needs to further modify the input $|\psi_0\rangle$ to generalize to include a subspace, and then nest the whole procedure into another layer of decision loop.

6.3 Motzkin and Quantum Error Correction

The Motzkin chain’s ground state, characterized by its high degree of entanglement, offers a fertile ground for AQEC. This high entanglement suggests potential for error correction if appropriately harnessed. The concept of subsystem variance emerges as a critical measure in this context, quantifying the robustness of the chain’s encoded states against local perturbations and errors.

Given a quantum code defined by the code space \mathfrak{C} , the subsystem variance $\varepsilon(\mathfrak{C}, d, \mathbf{G})$ is defined as [99]:

$$\varepsilon(\mathfrak{C}, d, \mathbf{G}) = \max_{\psi \in \mathfrak{C}, |S| \leq d} \|\psi_S - \Gamma_S\|, \quad (6.10)$$

where Γ denotes the maximally mixed state over the code space \mathfrak{C} , and S represents a subsystem of size at most d under the adjacency graph \mathbf{G} . This metric essentially captures the largest deviation of local reduced states from their average, offering a quantifiable measure of how local errors affect the encoded information.

This parameter is crucial for assessing the AQEC properties of any quantum code. It reflects the degree to which the code deviates from ideal quantum error-correcting conditions under local noise, thereby providing a fundamental link to the code’s error-correcting performance.

6.3.1 Calculating Subsystem Variance for the Motzkin Chain

The subsequent analysis will focus on the detailed computation of the subsystem variance for the Motzkin chain. By employing numerical simulations and analytical techniques, we will explore how the unique structure of the Motzkin chain’s ground state contributes to its potential AQEC capabilities. The results from these investigations will not only enhance our understanding of the Motzkin chain as a quantum error-correcting code but also provide insights into the broader implications for error correction in highly entangled quantum systems.

To start we can select the subspace as simple as only consisting of the GS and 1st ES. Therefore, the problem can be simplified as the optimization problem over the problem of how to find the mixture of $|\psi_0\rangle$ and $|\psi_1\rangle$ such that the distance between this density matrix and the maximally mixed state can be maximized.

Generalized Reduced Density Matrix (RDM) Calculation We compute the generalized RDM to capture the quantum correlations between the GS and ES, providing

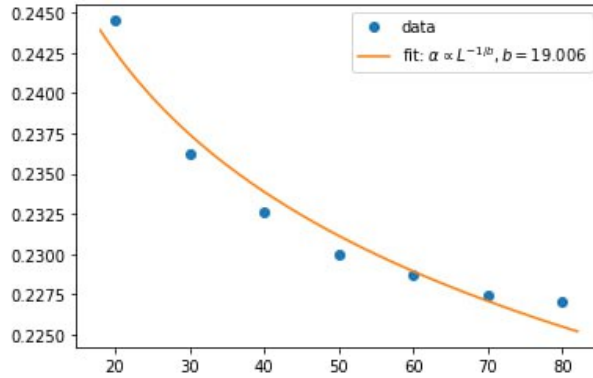


Figure 6.4: Power Law of the Subsystem Variance of Motzkin Chain with Scaling System Sizes

insights into their interaction dynamics. Most importantly, this step can drastically simplify the following-up procedures.

Mixed States Space Construction By generating mixed states as parametrized linear combinations of the GS and ES, we explore the spectrum of possible quantum states between these two extremes, enriching our understanding of the chain’s quantum landscape.

Distance Landscape With a given parametrized subspace, the whole problem turns into optimization over the distance landscape to find the peak. If the number of parameters is limited enough, one can simply sample over the whole space and bruteforcely extract the maximum points and values.

Systematic Study Across System Sizes The aforementioned analyses are replicated across various chain lengths, from $L=20$ to $L=80$, to observe how these quantum properties evolve with system size, enhancing our understanding of scaling behaviors.

Analysis of Variance Scaling In Figure 6.4, we present the observed scaling relationship between the subsystem variance and system sizes for the setup previously defined, where the variance scales approximately as a power law with an exponent of $-1/19$. This scaling, while indicative of a significant trend, does not perfectly align with theoretical predictions. The deviation from an ideal fit can be attributed to several factors:

- **Quality of Excited States:** The first excited states (ES) of the Motzkin chain, especially at larger system sizes, exhibit intricate structural complexities not present in the ground state (GS). These complexities can introduce anomalies in the observed scaling behavior due to the ES's sensitivity to boundary conditions and finite-size effects.
- **Theoretical Underpinnings:** Currently, a comprehensive systematic theory that fully explains the AQEC properties across various models remains undeveloped. Our understanding is mostly confined to asymptotic behaviors rather than precise, quantifiable predictions that are commonplace in more mature fields of study.

These observations underline the challenges in generalizing AQEC properties and stress the need for further theoretical and empirical research to refine our understanding of quantum error correction in complex quantum systems.

6.4 Summary

The exploration of Motzkin chains within this study has illuminated several critical aspects and innovative potentials of quantum spin chain models. The following insights summarize the significant findings and their implications.

- **Complexity of Local, Frustration-Free Hamiltonians:** Despite being local and frustration-free, the Hamiltonians, such as those governing Motzkin chains, exhibit remarkable complexity and exotic properties, even when gapped. This breaks away from the conventional expectation that local and frustration-free systems must inherently display trivial quantum behaviors. Instead, these systems can host a diverse spectrum of quantum states with intricate entanglement patterns, highlighting a rich area for deeper quantum mechanical explorations and theoretical advancements.
- **Effectiveness of MPS Representations:** Matrix Product States (MPS) continue to prove effective in representing states within these complex systems. MPS, a powerful tool in the study of quantum many-body systems, is particularly adept at capturing the nuances of these exotic states without compromising computational feasibility. This underscores the adaptability of MPS techniques in handling not only simple but also highly entangled and complex quantum states, reaffirming their utility in theoretical and computational quantum physics.
- **Encoding Time-Series in Static Spin Chains:** The study of Motzkin chains suggests an intriguing potential for static, local spin chains to model time-series data. This insight opens up a novel application of quantum spin chains beyond traditional physics, venturing into the realms of data analysis and computational finance. By mapping time progression onto spatial dimensions within the chain, and utilizing the quantum mechanical properties of the system, we can potentially develop new methods for forecasting and analyzing time-dependent data. This could lead to breakthroughs in how we model economic, meteorological, or any sequential data using quantum systems.

These findings not only advance our understanding of quantum spin chains like the Motzkin model but also expand the potential applications of quantum mechanics in other scientific domains. As we continue to unravel the capabilities of these models, we pave the way for innovative interdisciplinary applications that harness the principles of quantum mechanics to solve complex problems in science and technology.

Chapter 7

Conclusion and Future Work

In this thesis, we have conducted a detailed exploration of three distinct quantum many-body systems, utilizing the DMRG technique along with various analytical approaches to uncover deep insights into their complex behaviors and characteristics. These systems—Spin- S Kitaev ladders, Heisenberg mixed ladders, and Motzkin chains—exhibit not only fundamentally distinct quantum phases but also diverse areas of research interest.

Despite their differences, a common thread has emerged: the representation of quantum states using tensor networks, particularly MPS. This methodological approach has, in some sense, unified the superficial differences between these models, suggesting that tensor network methods might serve as a universal framework for engaging with quantum many-body systems in one-dimensional (1D) and quasi-one-dimensional settings, and potentially extending to two-dimensional (2D) systems in the future.

This chapter aims to succinctly recapitulate the core content presented, outline ongoing research, and highlight several promising directions for future exploration and potential applications.

7.1 Key Findings and Comparisons

7.1.1 Spin- S Kitaev Ladders

Our comprehensive investigation into Spin- S Kitaev ladders has unveiled a richly varied phase diagram, marked by distinct phases such as symmetry-breaking (SSB), symmetry-protected topological (SPT) phases, and trivial states. Notably, the integer-spin Kitaev ladders exhibit both first-order and second-order phase transitions, showcasing the dynamic interplay of quantum states. Furthermore, half-integer spin systems display a fascinating gapless region where SPT phases converge, highlighting the complex interactions within the Kitaev model. Additionally, an apparent even-odd oscillation effect in the phase characteristics becomes more pronounced as the spin dimension increases, revealing deeper quantum mechanical behaviors as the system scales from spin- $\frac{1}{2}$ up to spin-4.

7.1.2 Heisenberg Mixed Ladders

Investigations into Heisenberg mixed ladders have illuminated their non-standard magnetization profiles and dynamic properties, indicative of underlying Luttinger liquid behavior. This deviation from simple magnon-based models points to a rich array of quantum phase transitions driven by inherent fluctuations and microscopic interactions. The current numerical results lay the groundwork for a more extensive theoretical exploration, with a comprehensive theory still under development to fully describe the model's complex behaviors and its extensions.

7.1.3 Motzkin Chains

Our studies of Motzkin chains have revealed extraordinary entanglement properties that distinguish them from behaviors typically observed in other gapped one-dimensional systems. The unique entanglement features of Motzkin chains, particularly within their ground states, challenge traditional notions of quantum entanglement in local gapped systems. These findings not only advance our understanding of quantum state complexity but also underscore the potential of Motzkin chains in the context of approximate quantum error correction (AQEC). Additionally, the integration of combinatorial structures within the Motzkin chain Hamiltonian and its states offers insightful connections between classical combinatorial problems and quantum many-body systems, opening new avenues for exploring quantum-classical analogies.

7.2 Extending Tensor Networks: Prospects in Quantum Mechanics and Machine Learning

This section outlines the promising intersection of Tensor Networks (TN), Quantum Mechanics (QM), and Machine Learning (ML), underscoring the significant potential for TN methods in quantum research facilitated by their inherent linear algebra structure. This integration is poised to revolutionize the efficiency and scalability of simulations and analyses in quantum many-body systems, highlighting the role of TN in the future of quantum science and technology.

7.2.1 Data Driven Standard Automatic Library

As evidenced through ongoing research, the attributes of straightforwardness, efficiency, and accuracy inherent in tensor network techniques make them ideal for exploring quantum many-body systems in one-dimensional or quasi-one-dimensional configurations. This opens up the possibility for these systems to be modeled as part of a data-driven, extensive project shared among quantum physicists and the general public alike.

Tensor Networks offer a novel "white-box" framework for demystifying quantum states, providing great interpretability and manageability. This approach not only simplifies the understanding of complex quantum interactions but also enhances the transparency of computational models.

Moreover, the integration of a well-defined and structured dataset in quantum physics could pave the way for the seamless incorporation of modern toolkits, including AI, cloud computing, or at least some continuously organized pipeline as suggested in Chapter 3. This integration would not only allow for the application of advanced machine learning algorithms to predict, analyze, and interpret quantum phenomena with unprecedented precision and scalability, but also release extensive human resource that used to be put on manually searching and tuning parameters in Hamiltonian kaleidoscope.

References

- [1] Dmitry A Abanin, Ehud Altman, Immanuel Bloch, and Maksym Serbyn. Colloquium: Many-body localization, thermalization, and entanglement. *Reviews of Modern Physics*, 91(2):021001, 2019.
- [2] Cliò Efthimia Agrapidis, Jeroen van den Brink, and Satoshi Nishimoto. Ground state and low-energy excitations of the Kitaev-Heisenberg two-leg ladder. *Phys. Rev. B*, 99:224418, Jun 2019.
- [3] Ehud Altman, Gabriel Aeppli, et al. Quantum simulators: Architectures and opportunities. *PRX Quantum*, 2(1):017003, 2021.
- [4] D. J. Amit and V. Martin-Mayor. *Field Theory, the Renormalization Group, and Critical Phenomena*. World Scientific, 3 edition, 2005.
- [5] Leon Balents. Spin liquids in frustrated magnets. *Nature*, 464:199, Mar 2010.
- [6] A Banerjee, CA Bridges, J-Q Yan, AA Aczel, L Li, MB Stone, GE Granroth, MD Lumsden, Y Yiu, Johannes Knolle, et al. Proximate Kitaev quantum spin liquid behaviour in a honeycomb magnet. *Nature materials*, 15(7):733–740, Apr 2016.
- [7] G. Baskaran, Diptiman Sen, and R. Shankar. Spin- s Kitaev model: Classical ground states, order from disorder, and exact correlation functions. *Phys. Rev. B*, 78:115116, Sep 2008.
- [8] Owen Bradley, Jaan Oitmaa, Diptiman Sen, and Rajiv R. P. Singh. Thermodynamic behavior of modified integer-spin Kitaev models on the honeycomb lattice. *Phys. Rev. E*, 103:022109, Feb 2021.
- [9] Owen Bradley and Rajiv R. P. Singh. Instabilities of spin-1 Kitaev spin liquid phase in presence of single-ion anisotropies. *Phys. Rev. B*, 105:L060405, Feb 2022.

- [10] Sergey Bravyi, Libor Caha, Ramis Movassagh, Daniel Nagaj, and Peter W. Shor. Criticality without frustration for quantum spin-1 chains. *Phys. Rev. Lett.*, 109:207202, Nov 2012.
- [11] Hans J. Briegel and Robert Raussendorf. Persistent entanglement in arrays of interacting particles. *Phys. Rev. Lett.*, 86:910–913, Jan 2001.
- [12] Collin Broholm, RJ Cava, SA Kivelson, DG Nocera, MR Norman, and T Senthil. Quantum spin liquids. *Science*, 367(6475), 2020.
- [13] Pasquale Calabrese and John Cardy. Entanglement entropy and conformal field theory. *Journal of Physics A: Mathematical and Theoretical*, 42(50):504005, 2009.
- [14] Andrei Catuneanu, Erik S. Sørensen, and Hae-Young Kee. Nonlocal string order parameter in the $s = \frac{1}{2}$ Kitaev-Heisenberg ladder. *Phys. Rev. B*, 99:195112, May 2019.
- [15] Xie Chen, Zheng-Cheng Gu, Zheng-Xin Liu, and Xiao-Gang Wen. Symmetry protected topological orders and the group cohomology of their symmetry group. *Phys. Rev. B*, 87:155114, Apr 2013.
- [16] Yushao Chen, Yin-Chen He, and Aaron Szasz. Phase diagrams of spin- s kitaev ladders. *Phys. Rev. B*, 108:045124, Jul 2023.
- [17] Zhuo Chen, Laker Newhouse, Eddie Chen, Di Luo, and Marin Soljatic. ANTN: Bridging autoregressive neural networks and tensor networks for quantum many-body simulation. In *Thirty-seventh Conference on Neural Information Processing Systems*, 2023.
- [18] J Ignacio Cirac, David Perez-Garcia, Norbert Schuch, and Frank Verstraete. Matrix product states and projected entangled pair states: Concepts, symmetries, and theorems. *Reviews of Modern Physics*, 93(4):045003, 2021.
- [19] Pedro M. Cònsoli, Lukas Janssen, Matthias Vojta, and Eric C. Andrade. Heisenberg-kitaev model in a magnetic field: $1/s$ expansion. *Phys. Rev. B*, 102:155134, Oct 2020.
- [20] Tessa Cookmeyer and Joel E. Moore. Spin-wave analysis of the low-temperature thermal hall effect in the candidate Kitaev spin liquid α -RuCl₃. *Phys. Rev. B*, 98:060412, Aug 2018.
- [21] Xiao-Yu Dong and D. N. Sheng. Spin-1 Kitaev-Heisenberg model on a honeycomb lattice. *Phys. Rev. B*, 102:121102, Sep 2020.

- [22] Xiao-Yong Feng, Guang-Ming Zhang, and Tao Xiang. Topological characterization of quantum phase transitions in a spin-1/2 model. *Phys. Rev. Lett.*, 98:087204, Feb 2007.
- [23] Kiyu Fukui, Yasuyuki Kato, Joji Nasu, and Yukitoshi Motome. Ground-state phase diagram of spin- s Kitaev-Heisenberg models, 2022.
- [24] IM Georgescu, Sahel Ashhab, and Franco Nori. Quantum simulation. *Reviews of Modern Physics*, 86(1):153, 2014.
- [25] Jacob S. Gordon and Hae-Young Kee. Insights into the anisotropic spin- s Kitaev chain. *Phys. Rev. Research*, 4:013205, Mar 2022.
- [26] M Zahid Hasan and Charles L Kane. Colloquium: topological insulators. *Reviews of modern physics*, 82(4):3045, 2010.
- [27] Matthew B Hastings. An area law for one-dimensional quantum systems. *Journal of Statistical Mechanics: Theory and Experiment*, 2007(08):P08024, 2007.
- [28] M. Hermanns, I. Kimchi, and J. Knolle. Physics of the Kitaev model: Fractionalization, dynamic correlations, and material connections. *Annual Review of Condensed Matter Physics*, 9(1):17–33, 2018.
- [29] Ryszard Horodecki, Paweł Horodecki, Michał Horodecki, and Karol Horodecki. Quantum entanglement. *Reviews of modern physics*, 81(2):865, 2009.
- [30] Claude Itzykson and Jean-Michel Drouffe. *Statistical Field Theory*, volume 1. Cambridge University Press, 1989.
- [31] G. Jackeli and G. Khaliullin. Mott insulators in the strong spin-orbit coupling limit: From heisenberg to a quantum compass and Kitaev models. *Phys. Rev. Lett.*, 102:017205, Jan 2009.
- [32] Seong-Hoon Jang, Ryoya Sano, Yasuyuki Kato, and Yukitoshi Motome. Antiferromagnetic Kitaev interaction in f -electron based honeycomb magnets. *Phys. Rev. B*, 99:241106, Jun 2019.
- [33] Hong-Chen Jiang, Zheng-Yu Weng, and Tao Xiang. Accurate determination of tensor network state of quantum lattice models in two dimensions. *Physical Review Letters*, 101(9):090603, 2008.

- [34] Hui-Ke Jin, W. M. H. Natori, F. Pollmann, and J. Knolle. Unveiling the $s = 3/2$ Kitaev honeycomb spin liquids. *Nature Communications*, 13:3813, Jul 2022.
- [35] Y. Kasahara, T. Ohnishi, Y. Mizukami, O. Tanaka, Sixiao Ma, K. Sugii, N. Kurita, H. Tanaka, J. Nasu, Y. Motome, T. Shibauchi, and Y. Matsuda. Majorana quantization and half-integer thermal quantum hall effect in a Kitaev spin liquid. *Nature*, 559:227–231, Jul 2018.
- [36] Ilia Khait, P. Peter Stavropoulos, Hae-Young Kee, and Yong Baek Kim. Characterizing spin-one Kitaev quantum spin liquids. *Phys. Rev. Research*, 3:013160, Feb 2021.
- [37] Heung-Sik Kim and Hae-Young Kee. Crystal structure and magnetism in α -RuCl₃: An ab initio study. *Phys. Rev. B*, 93:155143, Apr 2016.
- [38] Heung-Sik Kim, Vijay Shankar V., Andrei Catuneanu, and Hae-Young Kee. Kitaev magnetism in honeycomb RuCl₃ with intermediate spin-orbit coupling. *Phys. Rev. B*, 91:241110, Jun 2015.
- [39] A Yu Kitaev. Fault-tolerant quantum computation by anyons. *Annals of Physics*, 303(1):2–30, 2003.
- [40] Alexei Kitaev. Anyons in an exactly solved model and beyond. *Annals of Physics*, 321(1):2–111, 2006.
- [41] J Knolle, R Moessner, and NB Perkins. Field-induced quantum spin liquid in the kitaev-heisenberg model and its relation to α -rucl3. *Physical review letters*, 122(4):047202, 2019.
- [42] Akihisa Koga, Hiroyuki Tomishige, and Joji Nasu. Ground-state and thermodynamic properties of an $s = 1$ Kitaev model. *Journal of the Physical Society of Japan*, 87(6):063703, 2018.
- [43] Hyun-Yong Lee, Ryui Kaneko, Li Ern Chern, Tsuyoshi Okubo, Youhei Yamaji, Naoki Kawashima, and Yong Baek Kim. Magnetic field induced quantum phases in a tensor network study of Kitaev magnets. *Nature Communications*, 11(1):1–7, 2020.
- [44] Hyun-Yong Lee, Naoki Kawashima, and Yong Baek Kim. Tensor network wave function of $s = 1$ Kitaev spin liquids. *Phys. Rev. Research*, 2:033318, Aug 2020.
- [45] Michael Levin and Xiao-Gang Wen. Detecting topological order in a ground state wave function. *Physical Review Letters*, 96(11):110405, 2006.

- [46] Elliott H. Lieb. *Flux Phase of the Half-Filled Band*, pages 79–82. Springer Berlin Heidelberg, Berlin, Heidelberg, 2004.
- [47] Huimei Liu, Ji ř Chaloupka, and Giniyat Khaliullin. Kitaev spin liquid in 3d transition metal compounds. *Phys. Rev. Lett.*, 125:047201, Jul 2020.
- [48] Huimei Liu and Giniyat Khaliullin. Pseudospin exchange interactions in d^7 cobalt compounds: Possible realization of the Kitaev model. *Phys. Rev. B*, 97:014407, Jan 2018.
- [49] A Loidl, P Lunkenheimer, and V Tsurkan. On the proximate Kitaev quantum-spin liquid α -RuCl₃: thermodynamics, excitations and continua. *Journal of Physics: Condensed Matter*, 33(44):443004, aug 2021.
- [50] Salvatore R. Manmana, E. M. Stoudenmire, Kaden R. A. Hazzard, Ana Maria Rey, and Alexey V. Gorshkov. Topological phases in ultracold polar-molecule quantum magnets. *Phys. Rev. B*, 87:081106, Feb 2013.
- [51] N. D. Mermin and H. Wagner. Absence of ferromagnetism or antiferromagnetism in one- or two-dimensional isotropic heisenberg models. *Physical Review Letters*, 17:1133–1136, 1966.
- [52] Alexandros Metavitsiadis and Wolfram Brenig. Flux mobility delocalization in the Kitaev spin ladder. *Phys. Rev. B*, 103:195102, May 2021.
- [53] Tetsuya Minakawa, Joji Nasu, and Akihisa Koga. Quantum and classical behavior of spin- s Kitaev models in the anisotropic limit. *Phys. Rev. B*, 99:104408, Mar 2019.
- [54] Grégoire Misguich and Vincent Pasquier. Quantum spin liquids and the metal-insulator transition in doped semiconductors. *Physical Review B*, 88(7):075104, 2013.
- [55] Raúl Morral-Yepes, Frank Pollmann, and Izabella Lovas. Detecting and stabilizing measurement-induced symmetry-protected topological phases in generalized cluster models. *arXiv preprint arXiv:2302.14551*, 2023.
- [56] Yukitoshi Motome, Ryoya Sano, Seonghoon Jang, Yusuke Sugita, and Yasuyuki Kato. Materials design of Kitaev spin liquids beyond the jackeli–khaliullin mechanism. *Journal of Physics: Condensed Matter*, 32(40):404001, jun 2020.
- [57] Ramis Movassagh. Entanglement and correlation functions of the quantum motzkin spin-chain. *Journal of Mathematical Physics*, 58(3), March 2017.

- [58] Rahul Nandkishore and David A Huse. Many-body localization and thermalization in quantum statistical mechanics. *Annual Review of Condensed Matter Physics*, 6(1):15–38, 2015.
- [59] Michael A Nielsen and Isaac L Chuang. Quantum computation and quantum information. *Quantum Computation and Quantum Information*, pages 1–25, 2010.
- [60] Roman Orus. A practical introduction to tensor networks: Matrix product states and projected entangled pair states. *Annals of Physics*, 349:117–158, 2014.
- [61] Roman Orus. Tensor networks for complex quantum systems. *Nature Reviews Physics*, 1(9):538–550, 2019.
- [62] K. W. Plumb, J. P. Clancy, L. J. Sandilands, V. Vijay Shankar, Y. F. Hu, K. S. Burch, Hae-Young Kee, and Young-June Kim. α -RuCl₃: A spin-orbit assisted mott insulator on a honeycomb lattice. *Phys. Rev. B*, 90:041112, Jul 2014.
- [63] Frank Pollmann, Subroto Mukerjee, Ari M. Turner, and Joel E. Moore. Theory of finite-entanglement scaling at one-dimensional quantum critical points. *Phys. Rev. Lett.*, 102:255701, Jun 2009.
- [64] Frank Pollmann and Ari M. Turner. Detection of symmetry-protected topological phases in one dimension. *Phys. Rev. B*, 86:125441, Sep 2012.
- [65] Frank Pollmann, Ari M. Turner, Erez Berg, and Masaki Oshikawa. Entanglement spectrum of a topological phase in one dimension. *Phys. Rev. B*, 81:064439, Feb 2010.
- [66] John Preskill. Quantum computing in the nisq era and beyond. *Quantum*, 2:79, 2018.
- [67] Robert Raussendorf and Hans J Briegel. One-way quantum computer. *Physical Review Letters*, 86(22):5188, 2001.
- [68] Subir Sachdev. *Quantum Phase Transitions*. Cambridge University Press, 2 edition, 2011.
- [69] Ryoya Sano, Yasuyuki Kato, and Yukitoshi Motome. Kitaev-Heisenberg hamiltonian for high-spin d^7 mott insulators. *Phys. Rev. B*, 97:014408, Jan 2018.
- [70] Lucile Savary and Leon Balents. Quantum spin liquids: a review. *Reports on Progress in Physics*, 80(1):016502, nov 2016.

- [71] Lucile Savary and Leon Balents. Quantum spin liquids: a review. *Reports on Progress in Physics*, 80(1):016502, 2017.
- [72] Ulrich Schollwöck. The density-matrix renormalization group in the age of matrix product states. *Annals of Physics*, 326(1):96 – 192, 2011.
- [73] Diptiman Sen, R. Shankar, Deepak Dhar, and Kabir Ramola. Spin-1 Kitaev model in one dimension. *Phys. Rev. B*, 82:195435, Nov 2010.
- [74] R. Shankar. *Principles of Quantum Mechanics*. Springer, 2 edition, 2012.
- [75] Yogesh Singh, S. Mani, J. Reuther, T. Berlijn, R. Thomale, W. Ku, S. Trebst, and P. Gegenwart. Relevance of the heisenberg-kitaev model for the honeycomb lattice iridates $A_2\text{IrO}_3$. *Phys. Rev. Lett.*, 108:127203, Mar 2012.
- [76] W. Son, L. Amico, and V. Vedral. Topological order in 1d cluster state protected by symmetry. *Quantum Information Processing*, 11:1961–1968, Dec 2012.
- [77] P. Peter Stavropoulos, Xiaoyu Liu, and Hae-Young Kee. Magnetic anisotropy in spin-3/2 with heavy ligand in honeycomb mott insulators: Application to CrI_3 . *Phys. Rev. Research*, 3:013216, Mar 2021.
- [78] P. Peter Stavropoulos, D. Pereira, and Hae-Young Kee. Microscopic mechanism for a higher-spin Kitaev model. *Phys. Rev. Lett.*, 123:037203, Jul 2019.
- [79] E Miles Stoudenmire and Steven R White. Studying two-dimensional systems with the density matrix renormalization group. *Annual Review of Condensed Matter Physics*, 3(1):111–128, 2012.
- [80] Masuo Suzuki. Generalized trotter’s formula and systematic approximants of exponential operators and inner derivations with applications to many-body problems. *Communications in Mathematical Physics*, 51(2):183–190, 1976.
- [81] Hidenori Takagi, Tomohiro Takayama, George Jackeli, Giniyat Khaliullin, and Stephen E. Nagler. Concept and realization of Kitaev quantum spin liquids. *Nature Reviews Physics*, 1:264–280, Apr 2019.
- [82] Simon Trebst and Ciarán Hickey. Kitaev materials. *Physics Reports*, 950:1–37, 2022.
- [83] Alexander A. Tsirlin and Philipp Gegenwart. Kitaev magnetism through the prism of lithium iridate. *physica status solidi (b)*, 259(5):2100146, 2022.

- [84] Ruben Verresen, Roderich Moessner, and Frank Pollmann. One-dimensional symmetry protected topological phases and their transitions. *Physical Review B*, 96(16):165124, 2017.
- [85] Frank Verstraete and J Ignacio Cirac. Matrix product states, projected entangled pair states, and variational renormalization group methods for quantum spin systems. *Advances in Physics*, 57(2):143–224, 2008.
- [86] Guifre Vidal. Classical simulation of infinite-size quantum lattice systems in two spatial dimensions. *Physical Review Letters*, 98(7):070201, 2007.
- [87] Xiao-Gang Wen. Quantum orders in an exact soluble model. *Physical Review Letters*, 90(1):016803, 2003.
- [88] Xiao-Gang Wen. Colloquium: Zoo of quantum-topological phases of matter. *Reviews of Modern Physics*, 89(4):041004, 2017.
- [89] Steven R. White. Density matrix formulation for quantum renormalization groups. *Phys. Rev. Lett.*, 69:2863–2866, Nov 1992.
- [90] Steven R. White. Density-matrix algorithms for quantum renormalization groups. *Phys. Rev. B*, 48:10345–10356, Oct 1993.
- [91] S. C. Williams, R. D. Johnson, F. Freund, Sungkyun Choi, A. Jesche, I. Kimchi, S. Manni, A. Bombardi, P. Manuel, P. Gegenwart, and R. Coldea. Incommensurate counterrotating magnetic order stabilized by Kitaev interactions in the layered honeycomb $\alpha - \text{Li}_2\text{IrO}_3$. *Phys. Rev. B*, 93:195158, May 2016.
- [92] Stephen M. Winter, Ying Li, Harald O. Jeschke, and Roser Valentí. Challenges in design of Kitaev materials: Magnetic interactions from competing energy scales. *Phys. Rev. B*, 93:214431, Jun 2016.
- [93] William Witczak-Krempa, Gang Chen, Yong Baek Kim, and Leon Balents. Correlated quantum phenomena in the strong spin-orbit regime. *Annual Review of Condensed Matter Physics*, 5(1):57–82, 2014.
- [94] Ning Wu. Topological phases of the two-leg Kitaev ladder. *Physics Letters A*, 376(46):3530–3534, 2012.
- [95] Changsong Xu, Junsheng Feng, Mitsuaki Kawamura, Youhei Yamaji, Yousra Nahas, Sergei Prokhorenko, Yang Qi, Hongjun Xiang, and L. Bellaiche. Possible Kitaev

- quantum spin liquid state in 2d materials with $s = 3/2$. *Phys. Rev. Lett.*, 124:087205, Feb 2020.
- [96] Changsong Xu, Junsheng Feng, Hongjun Xiang, and Laurent Bellaiche. Interplay between Kitaev interaction and single ion anisotropy in ferromagnetic CrI_3 and CrGeTe_3 monolayers. *npj Computational Materials*, 4:57, Nov 2018.
- [97] Wang Yang, Alberto Nocera, Paul Herringer, Robert Raussendorf, and Ian Affleck. Symmetry analysis of bond-alternating Kitaev spin chains and ladders. *Phys. Rev. B*, 105:094432, Mar 2022.
- [98] J. M. Yeomans. *Statistical Mechanics of Phase Transitions*. Oxford University Press, 1992.
- [99] Jinmin Yi, Weicheng Ye, Daniel Gottesman, and Zi-Wen Liu. Complexity and order in approximate quantum error-correcting codes, 2024.
- [100] T. Yokoi, S. Ma, Y. Kasahara, S. Kasahara, T. Shibauchi, N. Kurita, H. Tanaka, J. Nasu, Y. Motome, C. Hickey, S. Trebst, and Y. Matsuda. Half-integer quantized anomalous thermal hall effect in the Kitaev material candidate $\alpha\text{-RuCl}_3$. *Science*, 373(6554):568–572, 2021.
- [101] Vivien S Zapf, Michel Kenzelmann, et al. Magnetism in low dimensions: From quantum objects to quantum materials. *Reviews of Modern Physics*, 86(2):563, 2014.
- [102] Yi Zhou, Kazushi Kanoda, and Tai-Kai Ng. Quantum spin liquid states. *Rev. Mod. Phys.*, 89:025003, Apr 2017.
- [103] Zheng Zhu, Zheng-Yu Weng, and D. N. Sheng. Magnetic field induced spin liquids in $s = 1$ Kitaev honeycomb model. *Phys. Rev. Research*, 2:022047, Jun 2020.
- [104] Jean Zinn-Justin. *Quantum Field Theory and Critical Phenomena*. Oxford University Press, 4 edition, 2002.

APPENDICES

Appendix A

SPT detection in MPS

The now standard technique for detecting SPT order in an MPS was given by Pollmann and Turner [64]. We review their method, then explain how it can be modified for the present case, where the SPT order occurs in the effective model in the reduced Hilbert space \mathcal{H}_{GS} .

For a given iMPS $|\psi\rangle$ and corresponding symmetry group, e.g. a $G = \mathbb{Z}_2 \times \mathbb{Z}_2$ group and $g^a, g^b \in G$ the \mathbb{Z}_2 generators, we first apply the corresponding operators Σ^a, Σ^b onto $|\psi\rangle$ to get the generalized transfer matrices T^a, T^b ; then with T^a and T^b we calculate their largest eigenvalues η^a, η^b and corresponding eigenvectors U^a, U^b . If $|\eta^a| = |\eta^b| = 1$ the iMPS indeed respects the symmetry G . Furthermore, if $U^a U^b = -U^b U^a$, then $|\psi\rangle$ realizes a projective representation of the symmetry group; in contrast, $|\psi\rangle$ realizes a linear representation if U^a commutes with U^b . The method is summarized in Fig. A.1.

Note that the above description takes for granted that the local symmetry applies on the system site by site. However, we are often interested in systems where such translational symmetry is only partly respected. For example, in the cluster model $H = \sum_i \sigma_i^x \sigma_{i+1}^z \sigma_{i+2}^x$, the symmetry $G = \mathbb{Z}_2 \times \mathbb{Z}_2$ is implemented by two generators $Z_{\text{odd}} = \prod_k \sigma_{2k+1}^z$ and $Z_{\text{even}} = \prod_k \sigma_{2k}^z$. We should therefore view each pair of neighboring sites together as a single unit cell, then apply the method discussed before. Either of the two distinct groupings, $2k+1$ and $2k+2$ as a single unit cell or $2k$ and $2k+1$ as a single unit cell, is equally valid. The effect of a symmetry transformation on an iMPS in this more general case is illustrated in Fig. A.2.

The case of the Kitaev ladder has further complications. We can order the sites so that the Hamiltonian appears to be translation-invariant with a two site unit cell; let the corresponding two-site translation symmetry be \mathbb{T}_2 . However, the global symmetries Σ_u^Z

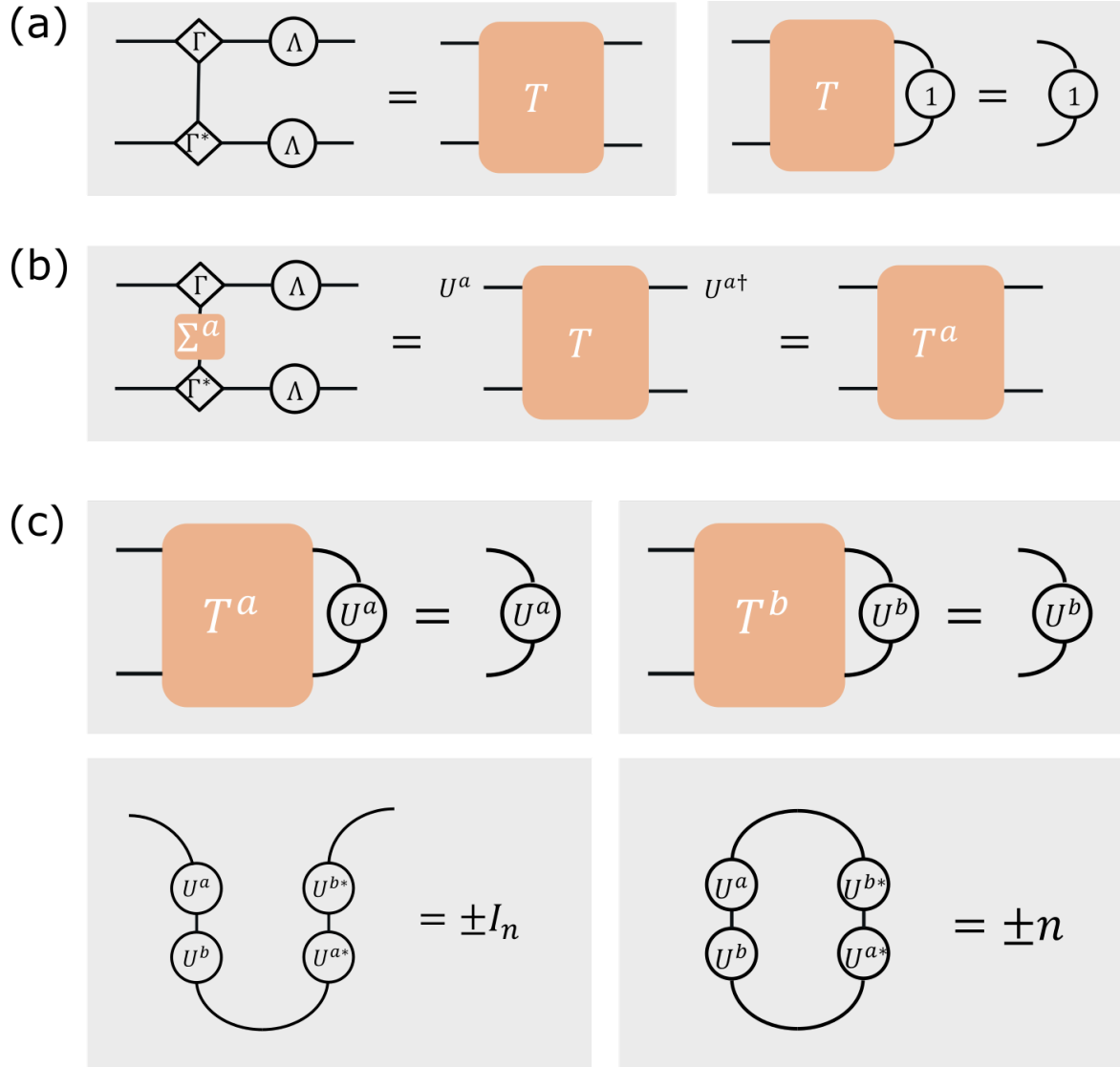


Figure A.1: Brief illustration of the detection of SPT order. (a) iMPS and its transfer matrix T . The corresponding leading eigenvector is the identity matrix, denoted by “1.” (b) iMPS transformed by a symmetry Σ^a and the corresponding generalized transfer matrix T^a , which is given in terms of the original transfer matrix by a unitary transformation U^a as shown. (c) The leading eigenvector of T^a is U^a . For two different elements a and b in the symmetry group $G = \mathbb{Z}_2 \times \mathbb{Z}_2$, we can calculate $U^a U^b U^{a\dagger} U^{b\dagger}$ to determine whether the iMPS belongs to an SPT phase.

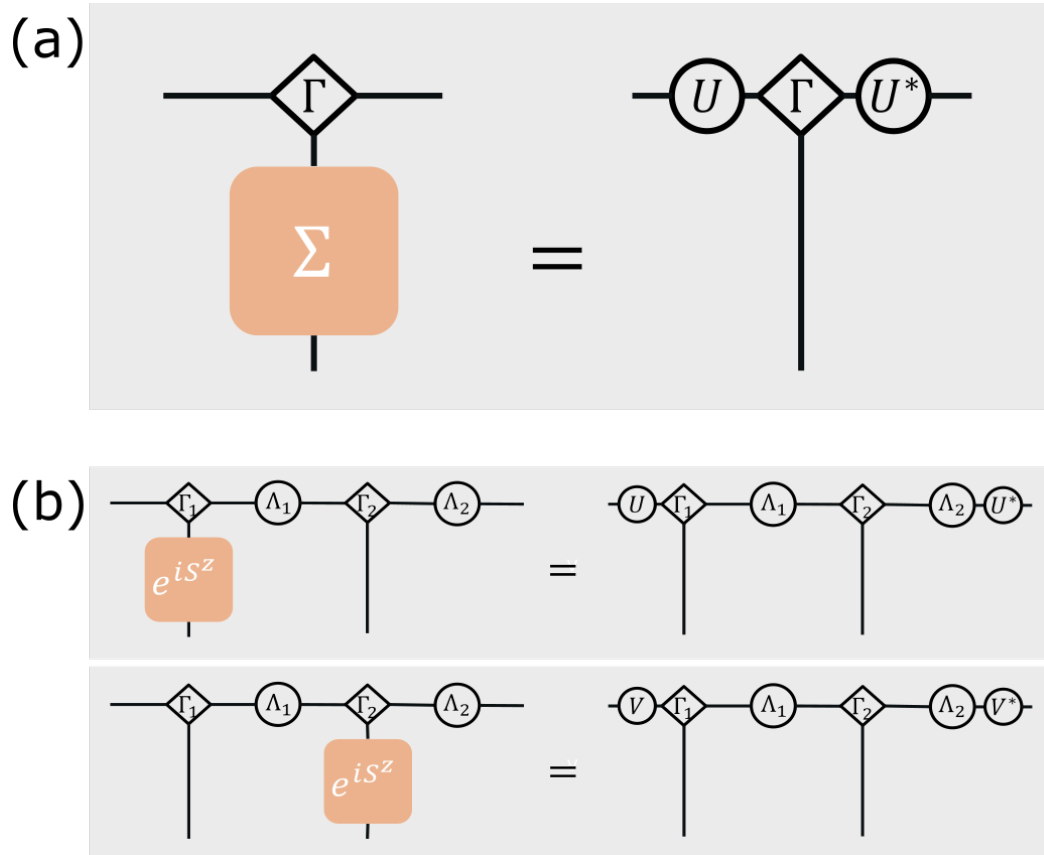


Figure A.2: Modification of symmetry action on iMPS for model with two-site symmetries. (a) A usual translation-invariant iMPS under the transformation of its on-site group $G = \{\Sigma\}$. (b) Action of symmetries on the ground state of the cluster model $H = \sum \sigma^x \sigma^z \sigma^x$, invariant under the translation by 2 sites.

and Σ_l^Z then act differently on even and odd unit cells. Explicitly, $\Sigma_u^Z \mathbb{T}_2 = \mathbb{T}_2 \Sigma_l^Z$, or intuitively \mathbb{T}_2 swaps Σ_u^Z and Σ_l^Z . We conclude that, although the Hamiltonian appears to have a two-site translation symmetry, in fact a four-site unit cell is needed when considering the action of symmetries.

We then want to use the original iMPS, with a four-site unit cell, to detect the SPT order of the effective cluster model from perturbation theory. In the X -limit or Y -limit where the cluster model arises, it seems natural to pick a unit cell that does not cut the dimers that form effective sites. Such a choice is illustrated in the Y -limit in Figs. A.3(a) and A.3(b).

What goes wrong if we shift the unit cell by one site, as in Fig. A.4, so that the unit cell boundary cuts across a dimer? This does not affect our measurement of the projective representation of $\Sigma_u^z \times \Sigma_l^z$. However, if we perform the same measurement for the global symmetries Σ^X and Σ^Y , we also naively find a signal of a projective representation, even though we know from perturbation theory that both symmetries map to the identity in the effective model and thus do not act nontrivially in the SPT phase.

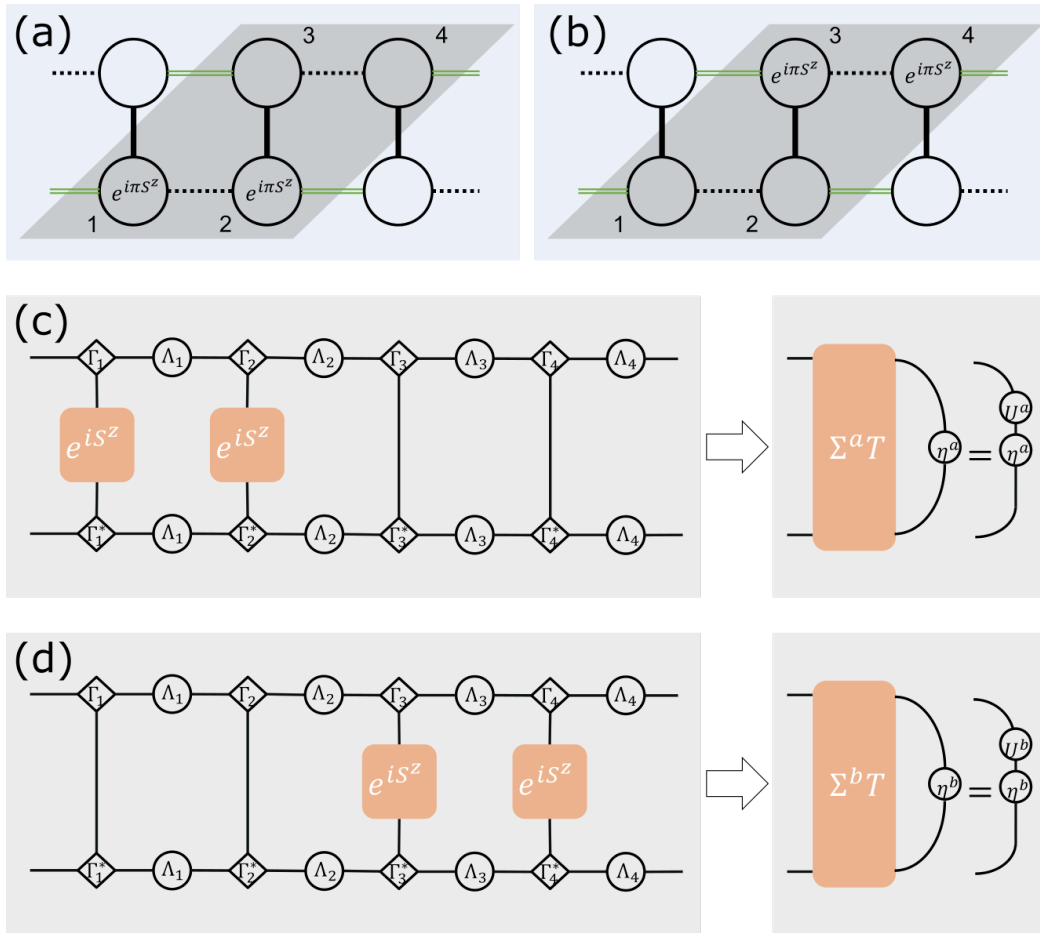


Figure A.3: (a)(b) An intuitive choice of unit cell inspired by perturbation theory. (c)(d) With this choice of unit cell, Σ_I^Z and Σ_u^Z act, respectively, on the first two sites and the last two sites.

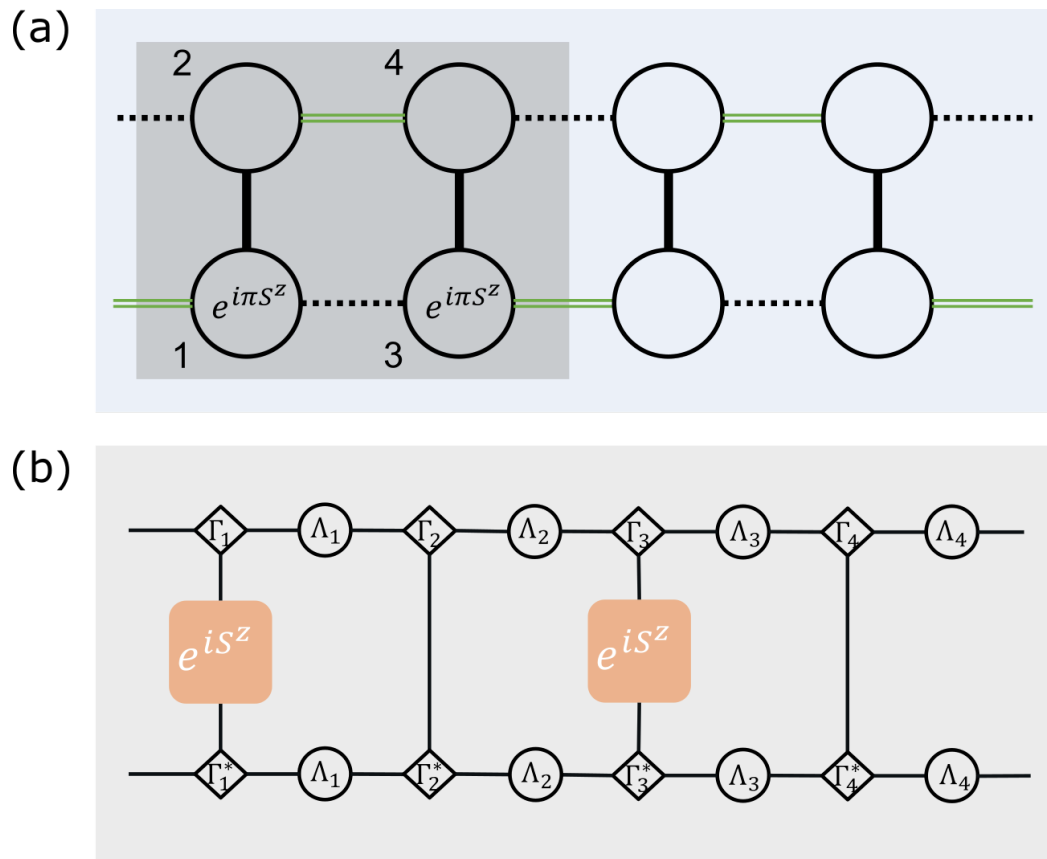


Figure A.4: (a) An improperly selected translationally invariant block for the same iMPS and (b) the corresponding local operators for the symmetry Σ_t^Z

Appendix B

SOPs and SPT distinction

Here we explain the construction of the SOPs of Fig. 4.5, used to distinguish the SPT- x and SPT- y phases of the Kitaev ladder.

In earlier explorations of string orders for distinguishing SPT phases and trivial phases [64, 55], researchers defined decorated SOPs for detecting SPT phases. The string bulk is given by (a local portion of) one of the symmetry operators, while two decorating operators that anticommute with the symmetry are added at the endpoints. For Kitaev ladders, the construction of SOPs is more intricate because the local D_n symmetries constrain the allowed SOPs that can be constructed.

To be more precise, following the same procedure of constructing SOPs for the cluster model, where one puts operators on even/odd positions, for the Kitaev ladder we can put $e^{i\pi S^z}$ (see Table B.1) on either the upper leg or the lower leg [64, 55]. However, using only $e^{i\pi S^z}$, at the two ends of each string there emerges anticommutation with D_n which enforces the pure Z -strings (on a single leg) to have zero expectation value. Therefore, it is necessary to decorate the end points of such Z -strings with either $e^{i\pi S^x}$ or $e^{i\pi S^y}$. The SOPs from Fig. 4.5 are:

$$O_x = e^{i\pi S_1^x} \left(\prod_{n=1}^N e^{i\pi S_{4n-2}^z} e^{i\pi S_{4n-1}^z} \right) e^{i\pi S_{4N}^x} \quad (\text{B.1})$$

$$O_y = e^{i\pi S_2^y} \left(\prod_{n=1}^N e^{i\pi S_{4n-3}^z} e^{i\pi S_{4n}^z} \right) e^{i\pi S_{4N-1}^y} \quad (\text{B.2})$$

O_x has a bulk built from $\Sigma_u^Z := \prod_{n=1}^N e^{i\pi S_{4n-2}^z} e^{i\pi S_{4n-1}^z}$ that commutes with all the symmetries, while the endpoint operators anticommute with $\Sigma_l^Z := \prod_{n=1}^N e^{i\pi S_{4n-3}^z} e^{i\pi S_{4n}^z}$ and

$\Sigma_u^X \Sigma_l^Y$. O^x can also be mapped by a two-site translation along the snake order to get an equivalent SOP built from Σ_l^Z and with endpoints anticommuting with Σ_u^Z and $\Sigma_l^X \Sigma_u^Y$; this shifted SOP is shown in Fig. B.1). Likewise, O^y has endpoints that anticommute with Σ_u^Z and $\Sigma_u^X \Sigma_l^Y$ (and has an equivalent two-site shifted version interchanging the roles of the upper and lower legs of the ladder).

	X_{even}		X_{odd}	
	rep1	rep2	rep1	rep2
X -limit	Σ_u^Z	$\Sigma_l^X \Sigma_u^Y$	Σ_l^Z	$\Sigma_u^X \Sigma_l^Y$
Y -limit	Σ_l^Z	$\Sigma_l^X \Sigma_u^Y$	Σ_u^Z	$\Sigma_u^X \Sigma_l^Y$

Table B.1: Pre-images in the original model of the X_{even} and X_{odd} symmetries of the effective cluster model from perturbation theory in the X - and Y -limits for half-integer spin. “rep1” and “rep2” columns give two different elements of the original $\mathbb{Z}_2 \times \mathbb{Z}_2 \times \mathbb{Z}_2$ symmetry group, each of which map to X_{even} or X_{odd} in the specified anisotropic limit.

Note that, by multiplying local symmetries D_2, D_4, \dots with such SOPs, we can get the same X -strings or Y -strings as in [14]. For an illustration, see Fig. B.1.

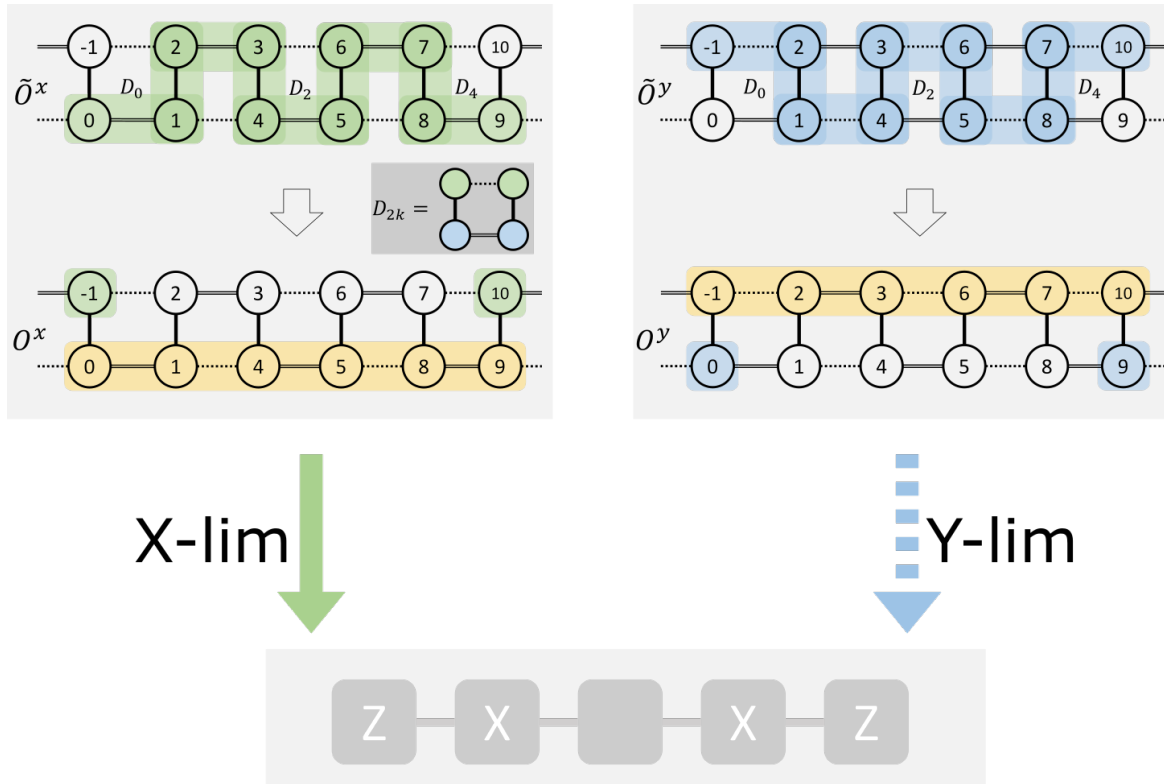


Figure B.1: Illustration of the string order parameters and their equivalent definition after multiplication with the local symmetries. Two SOPs in different limits map to effective SOPs of cluster model in different ways, which highlights the phase distinction. Note that the capitalized X and Z in the lower part indicate the operators in the effective models.